8-2009

Morphological Characterization of Irradiated Ultra High Molecular Weight Polyethylene (UHMWPE)

Christopher Phillip Stephens
University of Tennessee - Knoxville

To the Graduate Council:

I am submitting herewith a dissertation written by Christopher Phillip Stephens entitled "Morphological Characterization of Irradiated Ultra High Molecular Weight Polyethylene (UHMWPE)." I have examined the final electronic copy of this dissertation for form and content and recommend that it be accepted in partial fulfillment of the requirements for the degree of Doctor of Philosophy, with a major in Polymer Engineering.

Roberto S. Benson, Major Professor

We have read this dissertation and recommend its acceptance:

Wei He, Gajanan Bhat, Mitchell H. Goldman

Accepted for the Council:

Carolyn R. Hodges

Vice Provost and Dean of the Graduate School

(Original signatures are on file with official student records.)

To the Graduate Council:

I am submitting herewith a dissertation written by Christopher Phillip Stephens entitled "Morphological Characterization of Irradiated Ultra High Molecular Weight Polyethylene (UHMWPE)." I have examined the final electronic copy of this dissertation for form and content and recommend that it be accepted in partial fulfillment of the requirements for the degree of Doctor of Philosophy, with a major in Polymer Engineering.

Roberto S. Benson

Major Professor

We have read this dissertation

and recommend its acceptance:

Wei He

Gajanan Bhat

Mitchell H. Goldman

Accepted for the Council

Carolyn R. Hodges

Carolyn R. Hodges, Vice Provost and Dean of the Graduate School

Morphological Characterization of Irradiated Ultra High Molecular Weight Polyethylene (UHMWPE)

A Dissertation Presented for

The Doctor of Philosophy Degree

The University of Tennessee, Knoxville

Christopher Phillip Stephens

August 2009

ACKNOWLEDGEMENTS

The author would like to express appreciation to his mentor and friend, Dr. Roberto S. Benson. He would also like to show appreciation for the other members of his committee, Drs. Gajanan Bhat, Wei He, and Mitchell Goldman. The author would also like to thank Dr. J.S. Lin for use of the Small Angle X-Ray Scattering Facility in the Solid State Division of Oak Ridge National Laboratories. He would also like to show his appreciation to those people he supported him personally through the process of earning this degree including: his parents, Tim Hughes, Erin Hughes, Libby Hughes, Lori, Marshal Flynn, Mark Marlow, and Oren Yarbrough.

ABSTRACT

Effects of radiation (gamma and proton) on Ultra High Molecular Weight Polyethylene (UHMWPE) is studied for prosthetic joints and for radiation shielding for manned space missions. The first section of the dissertation will cover gamma radiation effects on UHMWPE by means of solubility, hardness, three-phase model, crystallite thickness, and molecular mobility studies. The second part will cover proton radiation effects on UHMWPE by means of solubility, three-phase crystallite model, and crystallite thickness study. The combined studies of the gamma irradiated samples shows that chain scission occurs on the surface and crosslinking in the center. The combined studies of the proton irradiated samples show that crosslinking occurs in the amorphous region and breaking of the tie chains and loops causes the growth of the already existing crystals. A new method has been developed to analyze DSC data based on crystallite thickness that generates crystallite thicknesses (number-average, weight-average, and z-average) and the lamella thickness polydispersity index, PDI (l_w/l_n and l_z/l_n). This new analysis method agrees with all other experiments conducted on the samples (solubility, molecular mobility, and three-phase model analysis).

Table of Contents

LIST OF TABLES

LIST OF FIGURES

1 Introduction

1.1 Production of Ultra High Molecular Weight Polyethylene (UHMWPE)

1.1.1 Polymerization

Polyethylene is produced in many molecular-level variants that include Low Density Polyethylene (LDPE), Linear Low Density Polyethylene (LLDPE), High Density Polyethylene (HDPE), and Ultra High Molecular Weight Polyethylene (UHMWPE). LDPE is a branched version of polyethylene and LLDPE is a copolymer ethylene and longer chain olefins that have very short branches. Both LDPE and LLDPE have a molecular weight of less than 50,000 g/mol [1]. HDPE is a linear polymer with a molecular weight of up to 200,000 g/mol [1]. UHMWPE typically has a viscosity average molecular weight of up to 6 million g/mol [1]. The extremely high molecular weight of UHMWPE endows this polymer with very special properties such as its high abrasion resistance, impact strength, low coefficient of friction, excellent biocompatibility, and chemical resistance, as seen in Table 1 [2, 3]. UHMWPE is produced by Ziegler gas polymerization with the main components of the polymerization being ethylene, hydrogen, and titanium tetra chloride; the strict requirement for purification of UHMWPE for medical use are covered in ASTM F648 and ISO 5834-1 [1]. The polymerization in gas form leads to a polymer product in the powder form.

Table 1: Physical properties comparison between HDPE and UHMWPE [1]

Property	HDPE	UHMWPE
Molecular Weight (10^6 g/mol)	0.05-0.25	2-6
Melting Temperature (^oC)	130-137	125-138
Poisson's Ratio	0.40	0.46
Specific Gravity	0.952-0.965	0.932-0.945
Tensile Modulus of Elasticity (GPa)	0.4-4.0	0.8-1.6
Tensile Yield Strength (MPa)	26-33	21-28
Tensile Ultimate Strength (MPa)	22-31	39-48
Tensile Ultimate Elongation (%)	10-1200	350-525
Impact Strength, Izod (J/m of notch; 3.175 mm thick specimen)	21-214	>1070 (no break)
Degree of Crystallinity (%)	60-80	39-75

1.1.2 Part Fabrication

Ultra High Molecular Weight Polyethylene (UHMWPE) has a multitude of uses in both industry and medicine. This dissertation will be concerned with UHMWPE's applications in articulating joints and as a radiation shield. Conversion of the powder polymerization product into a useful product requires a few steps. Due to UHMWPE's very high molecular weight it can not be formed using traditional polymer processing techniques and must be consolidated using high temperatures and pressures in a compression molding, ram extrusion, hot isostatic pressing, or direct part compression molding [1]. The consolidation occurs by a self diffusion process that leads to the formation of grain boundaries between the consolidated particles [1]. The surface properties of compression molded and machined surfaces have been shown to be very different by Schmidt [4]. However, this dissertation is not focused on the effect of surface texture, but instead on polymer morphology (e.g. crystallinity, crystallite thickness, and crosslinking).

1.2 Articulating Joints

1.2.1 Types of Joints

UHMWPE is the material of choice for artificial hip, knee, shoulder joints, as well as spinal implants. UHMWPE is used in the acetabular cup of the hip and tibial plateau of the knee. Both components are major load bearing surfaces that articulate against a metal counterface.

1.2.2 History

The first artificial articulating joint was implanted by Charnley in the 1950s and was composed a PTFE acetabular cup and a metal counterface [1]. PTFE was chosen because of its low coefficient of friction, but it failed due to its high wear rate. The PTFE component was replaced by UHMWPE in 1962 [1]. The generated wear debris from

UHMWPE can result in many problems for the patient, including osteolysis (bone resorption), inflammatory and cytotoxic reactions. The issues seen with the polymer-on-metal (POM) joints are still under investigation. In the past decade, there have been interest in metal-on-metal (MOM), ceramic-on-metal (COM), and ceramic-on-ceramic (COC) joints as a replacement for POM joints, but these also have their drawbacks. Both the MOM and COM acetabular cups typically have a sandwich design where UHMWPE is used as the center of the cup with metal on both sides [1]. CoCr is typically the metal used in MOM joints and alumina or zirconia is the ceramic typically used in the COM joint [1]. Since 1998, there has been use of gamma irradiation of the POM joint past the sterilization point (40-100 kGy) to induce crosslinking of the UHMWPE, which is also occasionally followed by a heat treatement to quench free-radicals that remain after crosslinking [1]. This heat-treatment is important, since free-radicals can remain trapped in the crystalline region of the polymer for longer than 18 years before they can diffuse out of the crystallie and react to form a crosslink or chain scission [5].

1.2.3 Clinical Performance

The lifetime limiting factor of arthroplasties is the loosening of the metal-bone interface leading to revision of the prosthesis; this loosening is caused by wear debris from the UHMWPE acetabular cup the induces osteoclast-mediated bone resorption [6]. The wear debris generation rate fluctuates with a number of variables including but not limited to: UHMWPE fabrication methods, sterilization methods, and surface roughness. The wear rates for UHMWPE is comparatively low, as seen in Figure 1, typically within the range of 0.05 - 0.20 mm/year [7]. There is a 90% survivor rate for prostesis that wear less than 0.1 mm/year, but only 30% survival rate for prosthesis that wear 0.2 mm/year [6].

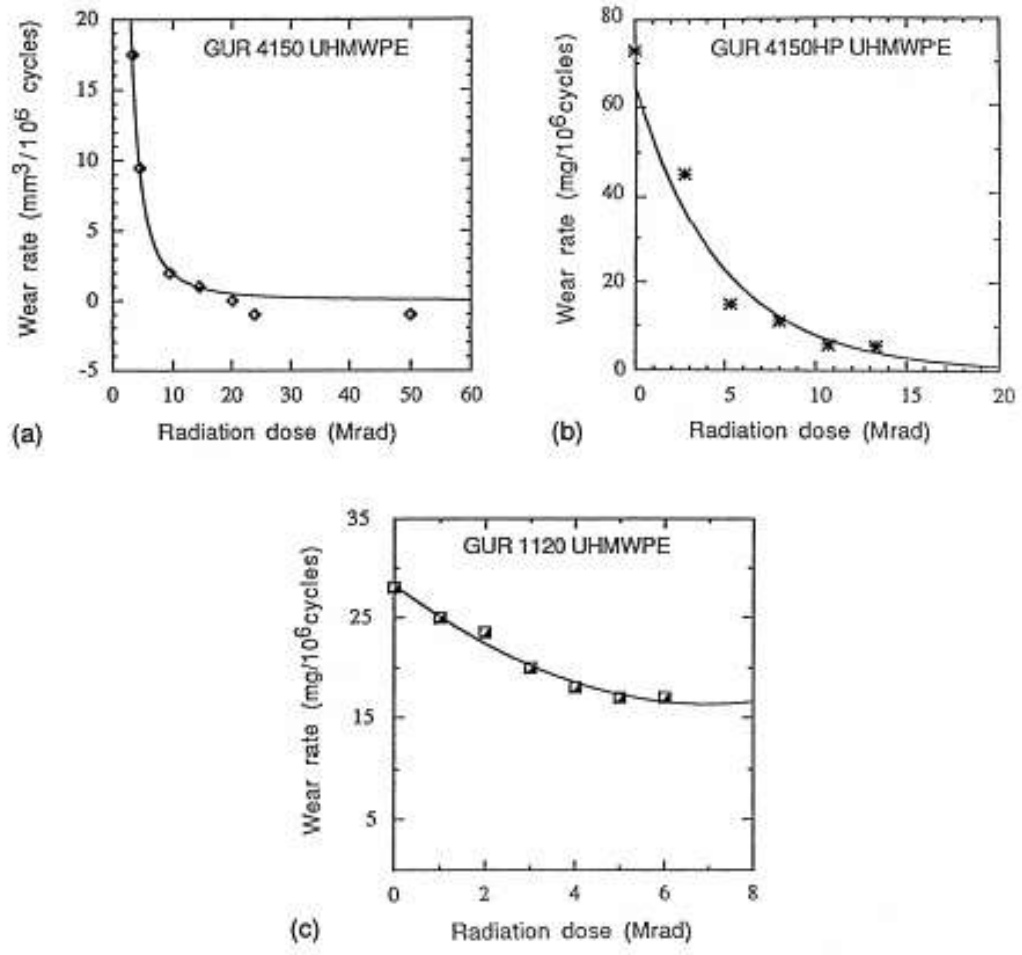

Figure 1: Effect of Radiation on the Wear Rate of UHMWPE in Hip Simulators [4]

Long term clinincal results show 20 kGy to be the optimal radiation dose, however wear rates are seen to decrease significantly up to 100-150 kGy [6]. Low in vitro wear rates of crosslinked UHMWPE are associated with small polydispersity indices (PDI) of the pre-irradiation polymer [6]. However, the problem is the size of the generated wear debris being in the bioactive range. The use of ionizing radiation to improve the overall wear rate of UHMWPE has been relatively successful, but a total understanding of the surface properties remains a necessity.

1.3 Sterilization

The most common methods of sterilization of UHMWPE based articulating joints is gamma irradiation due to the swiftness and track record of this method of sterilization, however gamma radiation exposure of UHMWPE leads to molecular-level changes that induce a depth dependent mechanical property change.

1.3.1 Gamma Radiation

UHMWPE can be sterilized with gamma radiation in air or in a controlled environment with a sterilization dose of 25 and 40 kGy [1]. Gamma sterilization induces molecular-level changes in the polymer such as crosslinking, chain scission, and oxidation. It is now well accepted that it is important to irradiate in an inert envionment (e.g. nitrogen or argon) to try to limit oxidative damage to the polymer.

1.3.2 Alternatives to Gamma Sterilization

EtO is a sterilization method that does not induce molecular changes to the polymer during the sterilization process. This highly toxic gas will neutrilize bacteria, spores, and viruses [1]. The main drawback seen with this technique is the time associated with the diffusion process associated with sterilization and degassing. Gas plasma sterilization is accomplished by creating a low-temperature plasma of peracetic acid or hydrogen

peroxide [1]. This sterilization method is expected to induce less molecular changes than gamma sterilization and does not have the potentially toxic residues seen with EtO sterilization [1].

1.4 Morphology

1.4.1 Crosslinking and Chain Scission

The free radicals formed during radiation will react to form either crosslinks or chain scissions depending on access to oxygen. The presence of molecular oxygen may completely prevent the formation of cross-links by reacting with the free radicals. Irradiation of polyethylene leads to the formation of free radicals, migration of free radicals, and reaction of free radicals into crosslinks or chain scissions, as seen in Figure 2. The first step in this process is the formation of a positive alkyl ion from the gamma radiation's interaction with the polyethylene chain [9]. The alkyl ion undergoes charge transfer until it reaches a vinyl or vinylene group, where it reacts and forms an ion radical [9]. After charge neutralization the allyl radical is formed [9]. The allyl radical is then free to form a crosslink or go through disproportionation creating a dead chain end. The presence of molecular oxygen (O_2) during and/or after irradiation leads to a higher degree of chain scission and deterioration of mechanical properties. In an inert environment, intermolecular cross-linking is the predominant process during ionizing radiation of polyethylene. The effect of ionizing radiation at high integral radiation doses leads to recombination of free radicals into inter-chain crosslinks; these crosslinks, as seen in Figure 2, lead to the improvement of wear resistance [6]. However, extensive crosslinking can lead to deleterious effects on fatigue, fatigue crack propagation, and fracture toughness [6]. The irradiation of polymers involves two competing processes: chain scission and cross-linking.

(1) Irradiation causes generation of new species:

$-CH_2-\dot{C}H-CH_2-$ (mobile alkyl radicals) + $\dot{H}$
$-CH_2-CH_2-$ → $-CH=CH-$ (double bond) + H_2
$-(CH_2-CH_2)_n-$ → $-(CH=CH)_n-$ (conjugated double bonds) + $n\ H_2$

and other radicals like methyl radical or those from additives and dissolved gases.

(2) Migration of mobile radicals and formation of relatively immobile allyl and polyenyl radicals:

$-\dot{C}H-CH_2-$ + $\dot{H}$ → $-CH=CH-$ (double bond) + H_2
$-(\dot{C}H-CH_2)_n-$ + $\dot{H}$ → $-(CH=CH)_n-$ (conjugated double bonds) + $n\ H_2$
$-\dot{C}H-CH_2-$ → $-CH_2-\dot{C}H-$ (intrachain migration of alkyl radicals)
$-\dot{C}H-CH_2-$ + $-CH_2-CH_2-$ → $-CH_2-CH_2-$ + $-\dot{C}H-CH_2-$ (interchain migration of alkyl radicals)
$-\dot{C}H-CH_2-(CH=CH)_n-$ → $-CH_2-\dot{C}H-(CH=CH)_n-$ (allyl and polyenyl radicals by intrachain migration)
$-\dot{C}H-CH_2-$ + $-CH_2-CH_2-(CH=CH)_n-$ → $-CH_2-\dot{C}H-(CH=CH)_n-$ + $-CH_2-CH_2-$ (allyl and polyenyl radicals by interchain migration)

(3) Reactions among alkyl radicals and with oxygen (alkyl radicals are represented by $\dot{R}$).
[Note: the following reactions are a chain and until all radicals are terminated they will continue.]

$\dot{R} + O_2$ → $R\dot{O}O$ (reversible step forming peroxy radicals)
$R\dot{O}O + RH$ → $ROOH + \dot{R}$ (propagation)
$ROOH$ → $R\dot{O} + H\dot{O}$ (hydroxyl radicals)
$R\dot{O} + RH$ → $ROH + \dot{R}$ (propagation and formation of alcohol)
$H\dot{O} + RH$ → $HOH + \dot{R}$ (propagation and formation of water)
$\dot{R} + \dot{R}$ → $R-R$ (cross-linking and termination)
$R\dot{O}O + R\dot{O}O$ → O_2 (cross-linking and termination)
$\dot{R} + R\dot{O}O$ → $ROOR$ (cross-linking and termination)
$-CH_2-CH(OOH)-CH_2-$ → $-CH_2-CHO + HO-CH_2-$ (scission and formation of aldehyde and alcohol)
$-CH_2-CH(OOH)-CH_2-$ → $HOH + -CH_2-(C=O)-CH_2-$ (scission and formation of ketone and water)
$-CH_2CH(OO)CH_2-$ → $CO_2 + -CH_3 + \dot{C}H_2-$ (scission and formation of CO_2)
Also, (1) other smaller radicals can also participate in termination; (2) smaller molecular weight hydrocarbons and CO can also be formed.

(4) Reactions of the allyl radical:

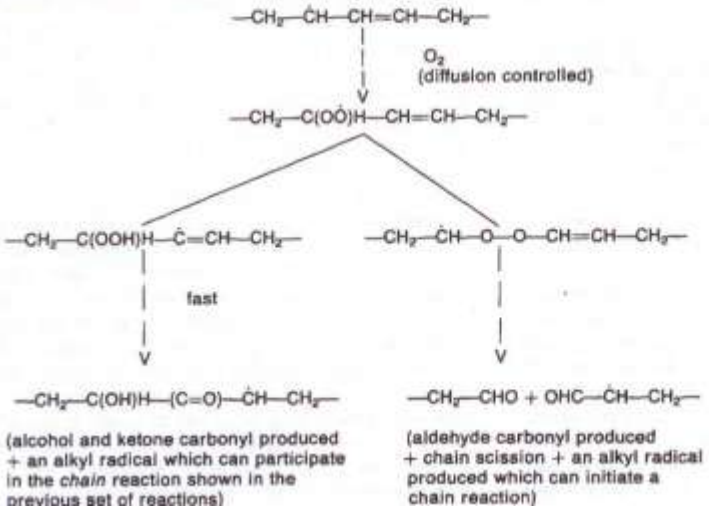

Figure 2: Irradiation Effects on Polyethylene [8]

When dispropotionation is the predominant termination step, chain scission prevails. A preference for the recombination of radicals as the termination step leads to formation of intermolecular cross-links. When the G-factor increases the probability of the reaction occurring increases, where the G-factor is defined as the units (crosslinks or chain scissions) produced per 100 eV of radiation. A G factor value of zero means that the probability of the reaction occurring is negligible, as seen in the crystalline region (Table 2). These g-factors show that polyethylene has a strong tendency to cross-link in the amorphous and interfacial regions, as seen in Table 2. The G(Crosslinking) is inversely proportional to the initial molecular weight of the polymer, so as the molecular weight goes to infinity the tendency to crosslink drops to zero [10]. It has also been shown that the crosslink density is inversely dependent on the polydispertisity index (PDI) of the starting polymer [6]. Increases in the level of crosslinking tend to increase mechanical integrity of the polymer and chain scission causes deterioration of mechanical properties.

Figure 3 displays typical free radical concentrations as a function of time and the subsequent concentration of oxidation products. It can be seen that there is a high concentration of oxidation products in the subsurface, due to the depth dependent absorbed dose and high concentration of oxygen near the surface of the material. Inversely, it is expected that the concentration of crosslinks will be high in the center of the sample as compared to the surfaces, since diffusion of oxygen to the center of the sample is slow enough to allow for crosslinking kinetics (Permeability of UHMWPE to oxygen is 0.047 cm^3 (STP)/cm^3*bar and decreases with increasing crystallinity) [11]. These two effects are shown together in Figure 4, where chain scissioning is present in the subsurface and crosslinking is prevalent in the center of the sample [12].

Table 2: G-Factors for crosslinking and scission of polyethylene [14]

	Amorphous	Interfacial	Crystalline
G(Scission)	0.5	0.5	~0
G(Crosslinking)	2.0	0.30 (Interchain-Intralamella) 0.13 (Interchain-Interlamella)	~0

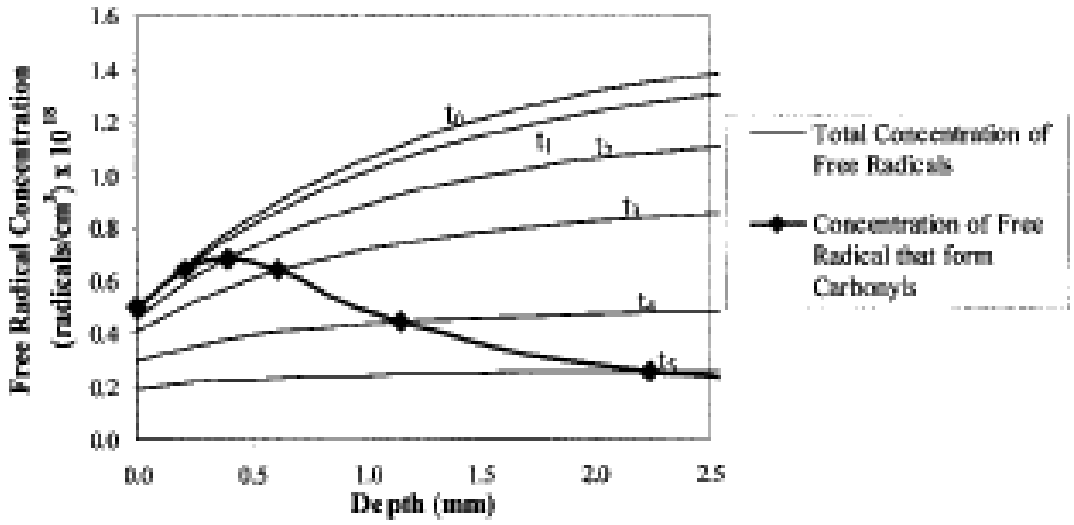

Figure 3: Concentration of Free-Radicals as a Function of Time and Subsequent Oxidative Product Concentration [12]

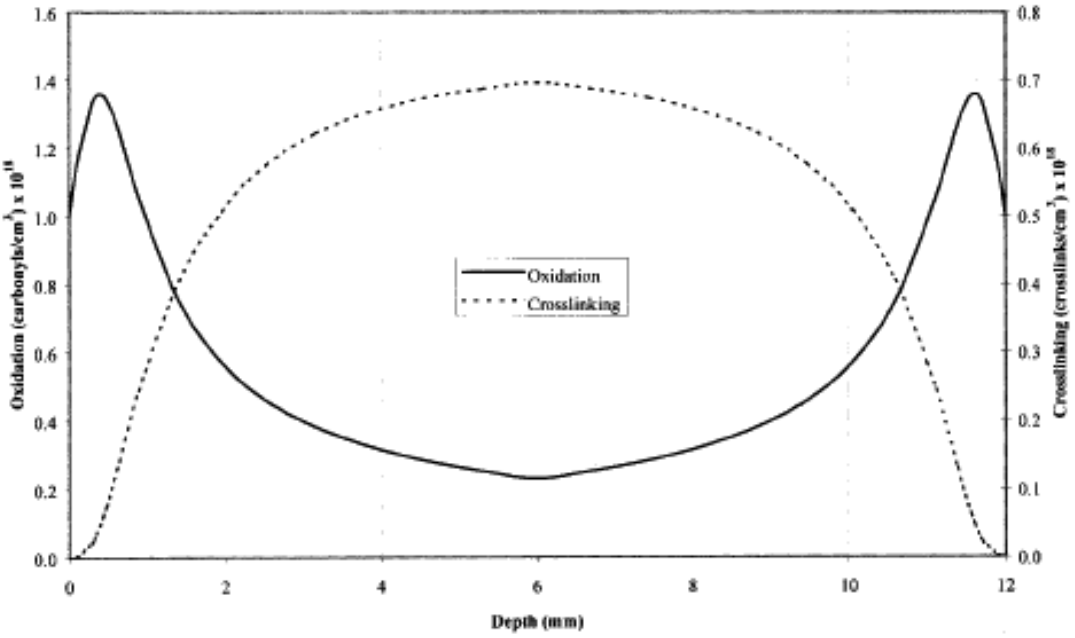

Figure 4: Depth Dependence of Crosslinking and Chain Scissioning [12]

1.4.2 Crystalline Morphology

Polyethylene organizes into an orthorhombic crystal (Figure 5 and Figure 6) with lattice parameters of a=0.7417nm, b=0.4945nm, and c=0.2547nm [13]. UHMWPE can be described efficiently by using a three-phase crystallite model. The three-phase crystallite model is composed of an amorphous, interfacial, and crystalline regions (Figure 7). The amorphous phase is a collection of entangled disordered chains. The crystalline region is a collection of chains that are fully organized into an orthorhombic lattice. The interfacial region of the polymer is composed of slightly ordered chains at the interface of the crystal and amorphous regions, which includes loops and tie chains. The long period (combined crystalline, interfacial, and amorphous size) of the PE crystal is determined by Small Angle X-Ray Scattering (SAXS). Differential Scanning Calorimetry (DSC) is used to find the lamella thickness, purely crystalline portion. Tie chains serve to connect the very strong crystalline regions with each other through the weak amorphous region, as illustrated in Figure 8.

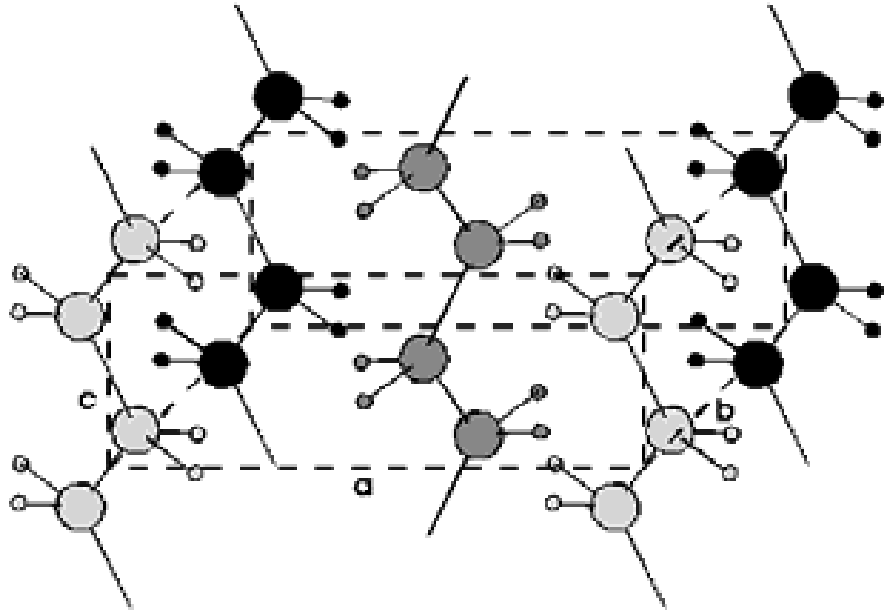

Figure 5: Polyethylene Unit Cell [15]

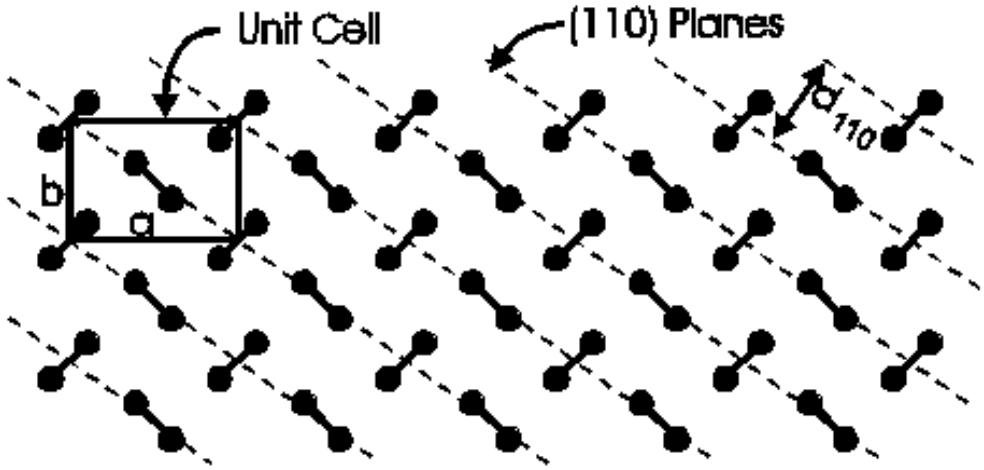

Figure 6: Polyethylene (110) Crystallographic Plane [15]

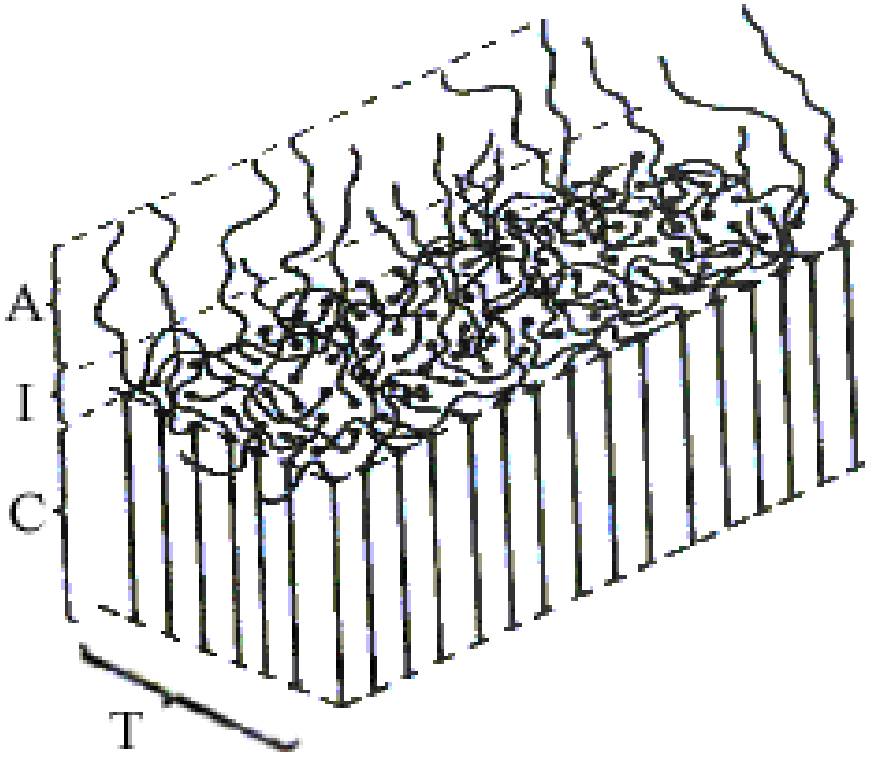

Figure 7: Three-Phase Crystallite Model

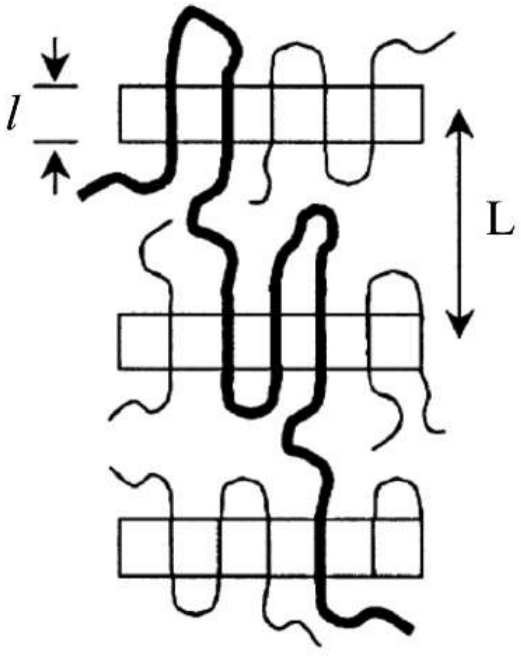

Figure 8: Tie Chains Between Lamella Crystals [16]

1.4.3 Effect of Radiation on Morphology

1.4.3.1 Particle Morphology

Since UHMWPE is of a molecular weight that is to high to flow in the molten state, fabrication of a device leads to grain boundary formation between particles of UHMWPE that have been compression molded together. This grain boundary is an inherent weakness in the material, since the only thing holding the particles of UHMWPE together is the few chain ends that self-diffuse between particles, leading to inter-particle bridges. These inter-particle bridges have been shown to be possible points for chain scissioning in irradiated UHMWPE, if oxygen is present [17]. If these inter-particle bridges are broken by the radiation, it leads to subsurface cracking on the grain boundary which eventually causes delamination and wear particle generation [17].

1.4.3.2 Crystalline Morphology

Radiation energy is absorbed within the semicrystalline material uniformly. Which means that radical formation should be uniform throughout the material [10]. However, it has been shown that upon radiation there is no significant cross-linking or chain scission that occurs within the crystalline core, which means that the radicals produced within this crystalline region must migrate to the edge of the crystal in order to react [10]. This means that cross-linking and chain scission is limited to the interfacial and amorphous regions of the materials. This fact makes the entangled loops and tie chains very important in a radiation study, because they are located at the interfacial region where there is a high concentration of radicals diffusing from within the crystal. This means that the interface could be exposed to a higher concentration of reactive radicals than the amorphous region, due to the diffusion of radicals out of the crystal. This fact will affect both the melting behavior and mechanical properties of the bulk polymer due to the

reduction of mobility of the chains, induced by crosslinking, that make up the reentry loops, tie chains, and amorphous region.

1.5 Radiation Shielding

Another application of UHMWPE is for manned space vehicles where the material acts as radiation shielding to reduce deleterious effects of radiation on DNA. The materials for radiation shielding are listed starting with the best: liquid hydrogen, liquid methane, lithium hydride, polyethylene, and then water [18]. Of the listed good radiation shielding materials polyethylene is chosen for cost saving and ease of use. Polyethylene is considered to be the benchmark material for radiation shielding [18]. This is primarily due to its high concentration of low Z materials, including hydrogen, carbon, and oxygen (if oxidized) [18]. UHMWPE is also an exceptional material for radiation shielding, due to its inherent tendency to cross-link upon irradiation, high hydrogen content, and high molecular mass. Another concern with radiation shielding material is the effect of atomic oxygen on the degradation of the polymeric material; however, much of this concern has been alleviated by coating the shielding material with a very thin coat of metal [19]. Much of this atomic oxygen is found in the low earth orbit (LEO) and causes erosion per incident oxygen atom of 3.97 ± 0.23 cm3/atom [19]. The study of radiation shielding is conducted using proton irradiation. Proton irradiation induces very similar chemical reactions to gamma irradiation, discussed above.

1.6 Scope of Dissertation

The first section of the dissertation will cover gamma radiation effects on UHMWPE by means of solubility, hardness, three-phase model, crystallite thickness, and molecular mobility studies. The second part will cover proton radiation effects on UHMWPE by means of solubility, three-phase crystallite model, and crystallite thickness study.

2 Theory

2.1.1 Differential Scanning Calorimetry (DSC)

2.1.1.1 DSC Measurement

The degree of crystallinity can be determined from DSC by using Equation 1, where the ΔH_{FUS} is the heat of fusion of the sample and ΔH_m is the heat of fusion for a sample of the same material with perfect (100%) crystalline material.

$$\alpha_m = \frac{\Delta H}{\Delta H_m} \tag{1}$$

2.1.1.2 Space Transformation

In order to gain further insight regarding crystallite size and distribution from the DSC Endotherm, it must be transformed into a probability distribution based on temperature (Equation 2). Where ΔH_m is the heat of fusion per unit mass for the perfect crystal, P(T) is the DSC power output, ρ_c is the crystalline density, M is the sample mass, and α_m is the mass fraction crystallinity of the sample [20]. These thermal parameters are used to determine the probability density as a function of temperature is given by f(T), Equation 2.

$$f(T)dT = \frac{1}{\alpha_m \Delta H_m} \frac{P(T)dT}{M\left(\frac{dT}{dt}\right)} \tag{2}$$

An apparent crystal thickness distribution is calculated from transferring f(T) into an equation dependent on the crystal thickness, l, (Equation 3) and the weight distribution function of thickness, Equations 4 and 5, where σ_e is the basal surface energy, T_m^o is the

melting temperature for an infinite crystal, and T_m is the melting temperature of the sample [20-22]. The transformation procedure is depicted graphically in Figure 9.

$$l = \frac{2\sigma_e 10^3}{\Delta H_m \rho_c \left(1 - \frac{T_m}{T_m^o}\right)}, \quad nm \tag{3}$$

$$g(l) = KP(T)\left(T_m^o - T\right)^2, \quad nm \tag{4}$$

$$K = \frac{\rho_c}{2\sigma_e T_m^o M \alpha_m 10^9 \left(\frac{dT}{dt}\right)} \tag{5}$$

The constant parameters for polyethylene are T_m^o=418.7 K, ΔH_m=288 kJ/kg, σ_e=90 mJ/m2, and ρ_c=967 kg/m3 and sample dependent parameters are T_m in K, α_m, M in kg, dT/dt in K per second and P(T) in mW [20]. The crystallizable sequence length is determined by dividing the crystallite thickness by the value for the c-dimension (0.2547nm) of a UHMWPE crystal, which tells the number of repeat units in the crystal. Often the crystallizable segment length will be capped with cross-links or oxidation products that cannot be incorporated into the crystal, as seen in Figure 10 (this will especially show to be true in melting and recrystallization post-irradiation). The crystallizable fractions of the pristine and irradiated UHMWPE samples were determined using equation 6, where x is the mole fraction of crystallizable units, R (1.9873 cal/mol K) is the gas constant, and ΔH_u (960 cal/mol) is the molar heat of fusion of repeat units in the crystals [23].

$$\frac{1}{T_m^c} = \frac{1}{T_m^o} - \frac{R}{\Delta H_u} \ln x \tag{6}$$

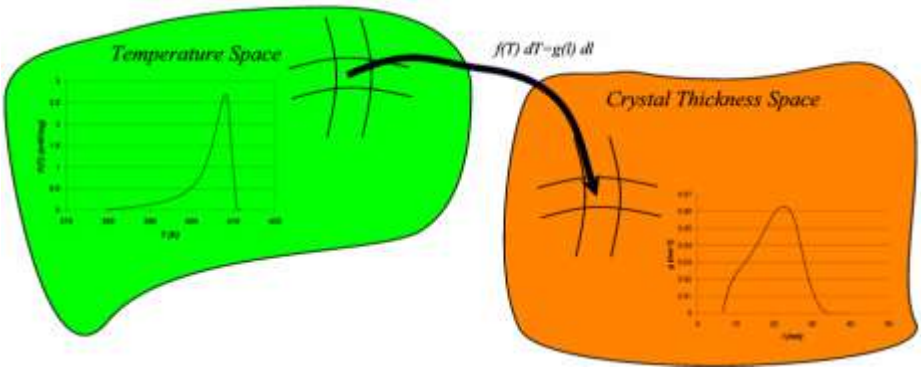

Figure 9: DSC Space Transformation

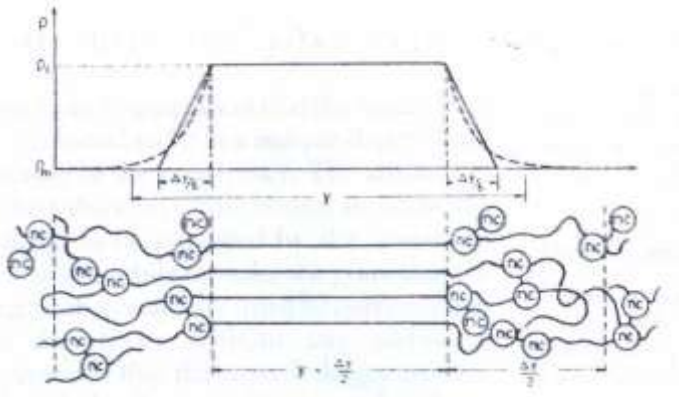

Figure 10: Effect of Non-Crystallizable Units on Crystallization

2.1.2 Wide Angle X-Ray Diffraction (WAXD)

WAXD allows for the determination of crystal structure by displaying the intensity of the x-ray beam diffracted by specific crystalline planes. The intensity of diffraction is measured as a function of the 2θ angle between the transmitted x-ray beam and the diffracted beam. A diffraction peak results from the additive diffraction of atoms sitting in a crystalline lattice diffracting from the same crystalline plane. Diffraction obeys bragg's law, equation 7, where d is the distance between crystallographic planes, λ is the radiation wavelength, 2θ is the angle of scatter, and n is the integer order of reflection

$$n\lambda = 2d \cdot \sin\theta \tag{7}$$

2.1.2.1 Crystallinity

Polyethylene's main diffraction peaks are from the 110 and 200 crystalline planes, which are at 2θ angles of 21^{o} and 24^{o} respectively. There is also a very broad diffraction from the amorphous phase. The crystallinity, W_c, was calculated by using equation 8, where I_{hkl} is the integrated intensity of the corresponding diffraction peak and I_A is the integrated intensity of the amorphous peak [20].

$$W_{c,x} = \frac{I_{110} + 1.42 * I_{200}}{I_{110} + 1.42 * I_{200} + 0.651 * I_A} \tag{8}$$

2.1.3 Small Angle X-Ray Scattering (SAXS)

SAXS is an analytical technique used to determine the long period of the polymer. The analysis used is based on Bragg's law stated in Equation 7 [24]. Bragg's law is set equal to the momentum transfer, Q, in Equation 9 to determine the long period of the repeat unit of the polymer [24]. Since we are looking at the first order of the reflection n is set equal to 1. Long period can be determined from Equation 10, where qmax is the q at the maximum of the Lorenz plot [4, 25].

$$Q = 4\pi\lambda^{-1}\sin\theta \quad (9)$$

$$L = \frac{2\pi}{q_{\max}} \quad (10)$$

By multiplying the DSC based crystalline fraction times the long period the size of the crystalline region can be determined. By multiplying the WAXD crystallinity by the long period the size of the crystalline region plus two interfacial regions can be determined. Therefore, using SAXS, DSC, and WAXD an approximation of the parts of the three-phase model can be determined.

2.1.4 Hardness Testing

2.1.4.1 Nanoindentation

Nano-indentation permits the determination of surface micro-properties such as hardness and modulus. This form of testing can provide better insight into surface morphology-property relationships. Normally this technique is used with indentations on nano-scale lengths, however due to the three-phase nature of the material the indenter had to probe much deeper, ~5 μm, to get an average of the phases and a reasonable hardness and modulus value.

Hardness can be calculated by the ratio of maximum load over contact area, since during the experiment load, contact area, and displacement into the material were measured. The reduced modulus of the material can be calculated by using Equation 11, where S is the stiffness of the material and A is the contact area [26]:

$$E_r = \frac{\sqrt{\pi}S}{2.068\sqrt{A}} \quad (11)$$

The modulus of sample can be calculated by using Equation 12. Where v is the Poisson's ratio of the sample (UHMWPE), v_i is the Poisson's ratio for the indenter tip (0.07), E_i (1141 GPa for diamond) is the modulus of the indenter, and E modulus of the sample [26]:

$$\frac{1}{E_r} = \frac{\left(1-v^2\right)}{E} + \frac{\left(1-v_i^2\right)}{E_i} \tag{12}$$

2.1.4.2 Hardness Analysis

The modulus of semi-crystalline polymers is known to depend directly on the degree of crystallinity, α. The micro-hardness has been shown to depend directly on crystal thickness, l_c [27, 28]. The dependence of the hardness of the crystal, H_c, on the crystal thickness, l_c, is illustrated in equation 13, where H_c^{∞} is the hardness of an infinite size crystal [27, 29]. The parameter b is defined by equation 14, where σ_e is the surface free energy and δ_h is the enthalpy of the crystal destruction [27, 29]. The yield stress is also able to estimated using the Tabor's relationship expressed in Equation 15 [27, 29]. From both the crystal hardness and yield stress relationships, it can be seen that both values are highly dependent on the lamella thickness, l_c.

$$H_c = \frac{H}{\alpha} = \frac{H_c^{\infty}}{\left(1+\frac{b}{l_c}\right)} \tag{13}$$

$$b = \frac{2\sigma_e}{\delta h} \tag{14}$$

$$\sigma_y^o \approx \frac{H_c}{3} \tag{15}$$

2.1.5 Swelling

The swell ratio is a relative measure of crosslinking in the gel phase, which is arrived at by the ratio of the gel weight in the swollen state to its weight in the nonswollen state. The lower the swell ratio the greater the crosslinking and the lower the molecular weight between cross-links. Equation 16 can be used to calculate swell ratio, where W_g is the weight of the swollen gel, W_d is the weight after the swollen gel is dried, W_o is the weight of the original sample, and $W_e = W_o - W_d$ (assuming no additives in the polymer). K is the ratio of the density of the polymer to that of the solvent at the immersion temperature. A value of 1.17 is used for the K ratio, which is based on high-density polyethylene at 110°C [22].

$$Swell\ Ratio = \frac{(W_g - W_d)}{W_d} K + 1 \tag{16}$$

As the degree of crosslinking induced in the material increases the amount of swelling decreases. The percent extract is a measure of the amount of polymer that is soluble. Equation 17 can be used to calculate the percent extract of the UHMWPE [22].

$$Extract,\% = \frac{(W_o - W_d)}{W_o} \times 100 \tag{17}$$

2.1.6 Dynamic Mechanical Analysis

DMA is a technique that allows identification of the relaxation processes in polymers. According to Popli et al. the PE relaxations occurs in the following temperature ranges: γ-relaxation occurs from -150 to -120°C, the β-relaxation occurs from -30 to 10°C, and the α-relaxation occurs from 30 to 120°C [30]. The γ-relaxation process is associated with the low temperature relaxation in a localized area of the amorphous regions. The β-relaxation is the medium temperature relaxation process associated with the amorphous phase of the polymer. The α-relaxation is seen at high temperature (below melting point)

and is associated with the crystalline phase of the material [31]. It has been shown that the temperature that the α-relaxation increases as the crystal lamellar thickness increases [30, 31]. Since UHMWPE is a semi-crystalline polymer all three relaxations are expected: the γ, β, and α.

3 Experimental

3.1 Sample Modification

3.1.1 Sample Preparation

UHMWPE samples are machined into discs with a diameter of 35 mm and a thickness of 6.35 mm from a rod of Tivar® 1000 produced by Poly Hi Solidor (Fort Wayne, IN).

3.1.2 Gamma Irradiation

Gamma Irradiation was conducted at the National Institute for Nuclear Research in Mexico City. The samples were exposed to gamma irradiation from a ^{60}Co source in an inert argon atmosphere at a dose rate of 0.25 kGy hr^{-1} (low dose rate) or 2.9 kGy hr^{-1} (high dose rate) for a integral dose of 75 or 150 kGy.

3.1.3 Proton Irradiation

Proton irradiation was conducted at the Indiana University Cyclotron Facility (IUCF). The samples were irradiated with protons at a fluence of $3.6x10^{17}$ protons/m^2 and a flux of $2x10^{14}$ protons/m^2s (low dose irradiation) and a fluence of about $2x10^{18}$ protons/m^2 (flux of about $3x10^{14}$ protons/m^2s) for the high dose irradiation. All irradiations were carried out in air, at room temperature. The total dose for each sample is listed in Table 3. The Linear Energy Transfer (LET) was estimated by using the standard SRIM program, with a corrected density of 0.97 g/cm^3 for UHMWPE. The LET was estimated for incident and emergent faces of the sample and averaged. Both electronic and nuclear contributions were added. The energy deposited by the beam in each sample was calculated by multiplying the average LET by the thickness of the sample. PMMA spacers of different thickness were used between UHMWPE samples. The samples were stacked together for irradiation, see Figure 11. The sample holder was made of a PVC (Polyvinylchloride)

tube. The spacer introduced a layer of air with a thickness of about 5 mm between samples in order to decrease heat accumulation during the irradiation. The energy deposited by the incident particle in the target is dominated by the electronic component, which is larger by about 2 orders of magnitude than the nuclear stopping power. The sample holder had about 40 positions for samples and it was calculated to allow for a total "sample length" longer by about 50% that the range of 200 MeV protons in polyethylene.

3.2 Characterization Techniques

3.2.1 Differential Scanning Calorimetery (DSC)

The basic principle of a DSC supplies enough energy to linearly increase the temperature of both a polymer sample and a reference sample, as seen in Figure 12. Following radiation, cores of 6.35 mm diameter are taken from the sample and sliced into 1 mm thick discs using a razor blade, to limit mechanical modification of the samples.

Table 3: Irradiation Dose

Irradiation Type	TOTAL DOSE (kGy)
Control	0
Low Dose	1.77 ± 1.2
High Dose	7.93 ± 1.0

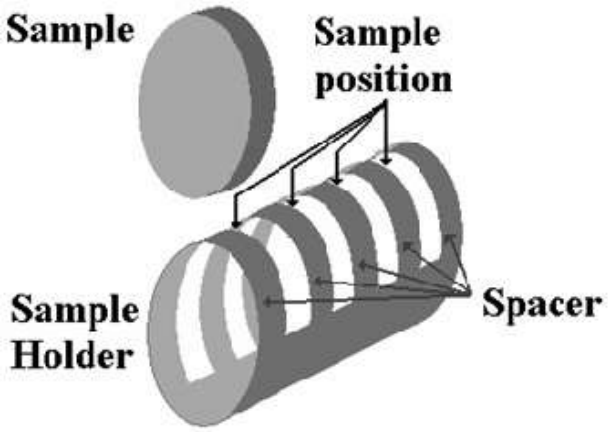

Figure 11: Sample Holder for Proton Irradiation

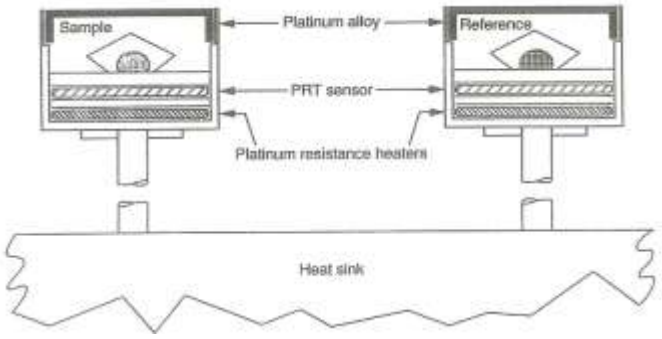

Figure 12: Schematic of a Typical DSC [35].

For the gamma irradiation experiments, a 1 mm thick sample is taken from the surface and center of the irradiated disc and held at 75^{o}C for 10 minutes followed by a heating segment from 75^{o}C to 180^{o}C at 1 ^{o}C/min. For the proton irradiation experiments, a 1 mm thick sample is taken from the surface of the sample and exposed to a three segment thermal test: 1) 75^{o}C to 180^{o}C at 1 ^{o}C/min (Run 1), 2) 180^{o}C to 75^{o}C at -1 ^{o}C/min, and 3) 75^{o}C to 180^{o}C at 1 ^{o}C/min (Run 2). These slow rate experiments avoid the artificial increase of the Tm, seen in 10 ^{o}C/min heating rate experiments, to values above the theoretical melting temperature of polyethylene assigned to infinite size crystals, T_m^o. Increase in melting temperature of UHMWPE has been cited by Zachariades and Logan [36, 37]. The anomaly is possibly due to the existence of crystals in a microenvironment consisting of high degree of chain entanglement and/or cross-linking found in these irradiated UHMWPE samples. Following each DSC run melting temperature corrections are conducted using an Indium standard. Following the experiment the endotherm is transformed into a probability distribution on crystalline lamella thickness, as discussed above. The median crystallite thickness, ln, of this probability distribution is then determined by integrating the area under the curve and determining the middle of the area, as displayed in Appendix II and IV. The first moment of this probability distribution is then calculated and the median crystallite thickness, lw, (Equation 18) of this distribution is determined by integrating the area under the curve to determine the median value.

$$l_w = \frac{\sum N_i l_i^2}{\sum N_i l_i} \tag{18}$$

The second moment of the probability function is determined and the median crystallite thickness, lz, (Equation 19) of this new distribution is determined by integrating the area

under the cure to determine the median value. A graphical depiction of the meaning of ln, lw, and lz is depicted in Figure 13.

$$l_z = \frac{\sum N_i l_i^3}{\sum N_i l_i^2} \tag{19}$$

3.2.2 Wide Angle X-Ray Diffraction (WAXD)

The samples were scanned over a 2-Theta range from 8 to 44 degrees in step sizes of 0.01 degrees held for 1 second. The detector used was a 4x4 Programmable Receiving Slit (PRS), and the source was controlled using a 2x2 Cross-slit. The generator was kept at 45 kV and 40 mA at all times during testing. The experimental setup is shown in Figure 14.

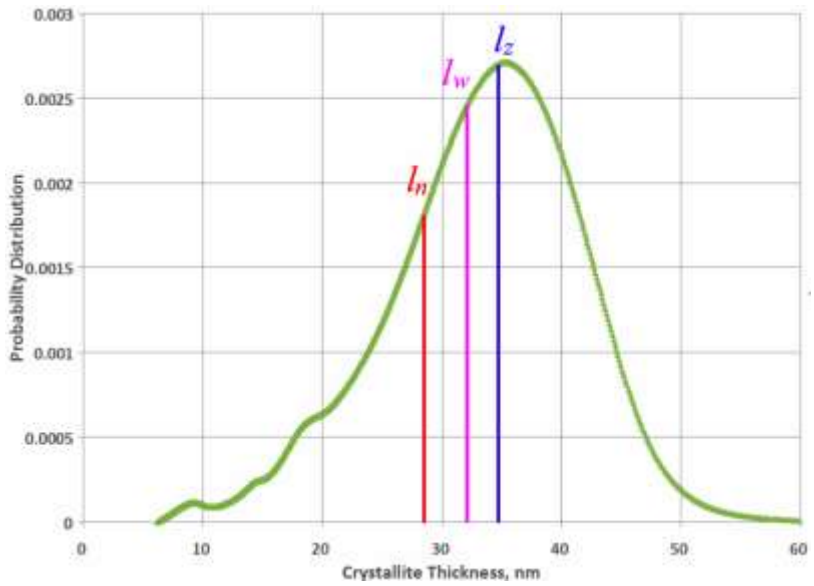

Figure 13: Graphical Depiction of the Number, Weight, and Z-Average Crystallite Thicknesses

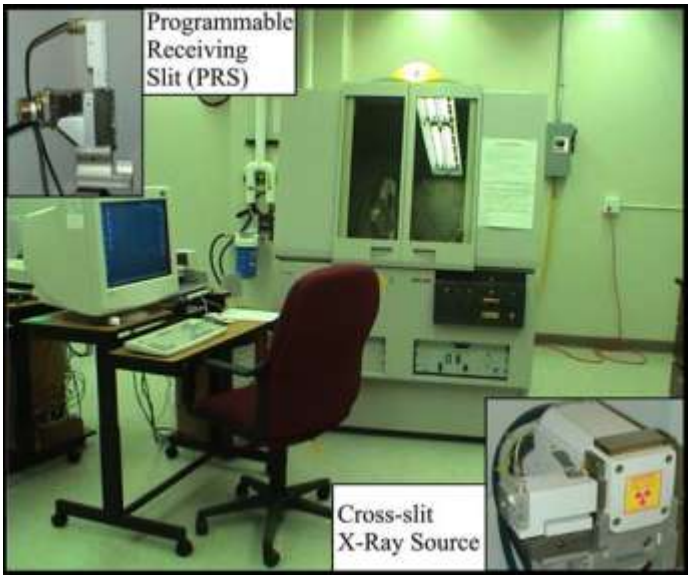

Figure 14: Wide-Angle X-ray Setup

3.2.3 Small Angle X-Ray Scattering (SAXS)

Following radiation 6.35 mm diameter cores are taken from the sample and sliced into 1 mm thick discs using a razor blade, to limit the introduction of stress induced morphological modification of the samples. The experiments were conducted using a 10-m SAXS camera within the Solid State Division at Oak Ridge National Laboratory. The 10-m SAXS camera consisted of x-ray source, a monochromator, a collimator, a specimen chamber, and a two dimensional position-sensitive detector. The detector is 20x20 cm^2 with an element spacing of 3 mm. The scattering vector (q) used was 0.0479nm^{-1} to 0.9812 nm^{-1}. The detector was held at 5.119 m from the sample. The machine was calibrated with a Fe55 radioactive isotope to remove background cosmic radiation and electronic noise. The power setting was maintained at 100 kV and 40 mA.

3.2.4 Nano-Indentation

A Nano-Indenter XP (Nano Instruments, Inc.) was used to determine the surface hardness and modulus. A three-sided pyramidal Berkovich indenter used in maximum load to penetrated the surface 17 to 22 μm depending on hardness of the sample. Indentation measurements were made in a Continuous Stiffness Measurement (CSM) mode. The load, displacement (h), and stiffness (S) data collected as a function of time was used to calculate the hardness (H) and elastic modulus (E) [38]. A total of four samples per treatment condition were studied. Each test specimen was indented 5 times at a temperature of 21.5 C. A Poisson ratio of 0.46 was assumed for the calculations [39]. The program settings for these tests included a strain rate of 0.003 sec^{-1} and a harmonic frequency of 45 Hz.

3.2.5 Swelling

Swelling experiments are based on ASTM standard D 2765-95 (swelling of PE) [22]. A core that is approximately 0.25-inches in diameter and 0.25-inches thick is used for

swelling experiments. All experiments are done in a ventilated fume hood, since xylene is a toxic and flammable solvent. An 8-oz jar with 100 mL of xylene is placed in an oil bath that is maintained at 110^{o}C. The sample in xylene is left in the oil bath for 24-hours in order to reach equilibrium swelling. At the completion of the 24-hour period of swelling the swollen sample is removed and put into a clean weighing bottle. The bottle is weighed to the nearest 0.001-g. The weighing bottle is then placed into a vacuum oven at 100 ^{o}C for 16-hours. After completion of the drying process the sample is weighed again to the nearest 0.001-g.

3.2.6 Dynamic Mechanical Thermal Analysis

Testing was done in a DMTA V from Rheometric Scientific. Testing was done from -150 ^{o}C to 160 ^{o}C at 1 ^{o}C/min in tensile mode with a strain of 0.03%. Liquid nitrogen was used for cooling of the sample.

4 Results and Discussion

4.1 Gamma Irradiation

There are many components of the polymer morphology that can be disrupted by radiation, including molecular weight (crosslinking and chain scission), crystallinity, crystallite thickness, and molecular mobility. This study covers all of the morphological components that can be affected, as well as nano-hardness and modulus.

4.1.1 Solubility Study

Swelling of UHMWPE in xylene at 110^{o}C showed a decrease in the swell ratio with increasing radiation, as seen in Table 4. The swollen irradiated cores had an hourglass shape, where the surface diameters were larger than the centers which means that the chains in the center of the sample were more constrained than the chains on the surface. This phenomena is caused by chain scissioning on the surface of the sample where the free-radiacals have access to oxygen and crosslinking deeper into the polymer, as illustrated in Figure 4.

4.1.2 Three-Phase Crystallite Study

The three-phase crystallite model (TPM) can be used to characterize the average morphology. The TPM has been created for the surface of the irradiated sample by using DSC crystallinity, WAXD crystallinity, and SAXS long period. The long periods and crystallinities used to make the TPM are shown in Table 5. This representation shows an increase in the crystalline region with a shrinkage in the interfacial region at low (Table 6 and Figure 15) and high (Table 7 and Figure 16) dose rates.

4.1.2.1 Crystallite Region

In the LDR samples, the increase in the crystalline region is 19% at 75 kGy and 22% at 150 kGy. In the HDR samples, the increase in the crystalline region is 16% at 75 kGy and 23% at 150 kGy. It can be seen that there is a significant increase in crystallinity with radiation at LDR and HDR.

4.1.2.2 Interfacial Region

In the LDR samples, the decrease in the interfacial region is 38% at 75 kGy and 90% at 150 kGy. In the HDR samples, the decrease in the interfacial region is 66% at 75 kGy and 68% at 150 kGy. There is a very significant decrease in the interfacial region with irradiation at LDR. There is a decrease in interfacial region with radiation at HDR, but not as significant as in the LDR samples.

4.1.2.3 Discussion

The increase in the crystalline region and decrease in interfacial region can be explained by the breaking of chains in the amorphous and interfacial regions, which are then oxidized and free to recrystallize. This increase in crystallite region is created at the expense of inter-lamella connectivity, which will lead to a decrease in toughness of the material. The number of new small crystals in the amorphous phase is dependent on the dose rate; at a high dose rate the tendency of the material is to form new crystals in the amorphous region and if the irradiation is conducted at a low dose rate the preference is to increase the already existing crystallite size by shrinking the amorphous region.

Table 4: Swell Ratio and %Extract for Gamma Irradiated UHMWPE

	Swell Ratio	% Extract
0 kGy	>34	--
75 kGy	6.72 ± 0.30	3.00 ± 1.58
150 kGy	4.85 ± 1.28	3.28 ± 3.22

Table 5: SAXS long period, WAXD crystallinity, and DSC crystallinity used to create three-phase-crystallite model

Dose (kGy)	Long Period (nm)		WAXD Crystallinity		DSC Crystallinity	
	Low Dose Rate	High Dose Rate	Low Dose Rate	High Dose Rate	Low Dose Rate	High Dose Rate
0	65.88 ± 0.5	65.88 ± 0.5	75.94%	75.14%	51.22%	51.22%
75	62.43 ± 0.1	62.96 ± 0.3	79.94%	70.76%	64.15%	62.21%
150	61.29 ± 0.5	63.11 ± 1.5	70.34%	73.54%	67.65%	65.53%

Table 6: Three Phase Model for Low Dose Rate Gamma Irradiation on the Surface

Dose (kGy)	Crystalline, nm	Interfacial, nm	Amorphous, nm
0	33.7	15.8	16.4
75	40.0	9.8	12.5
150	41.3	1.6	18.1

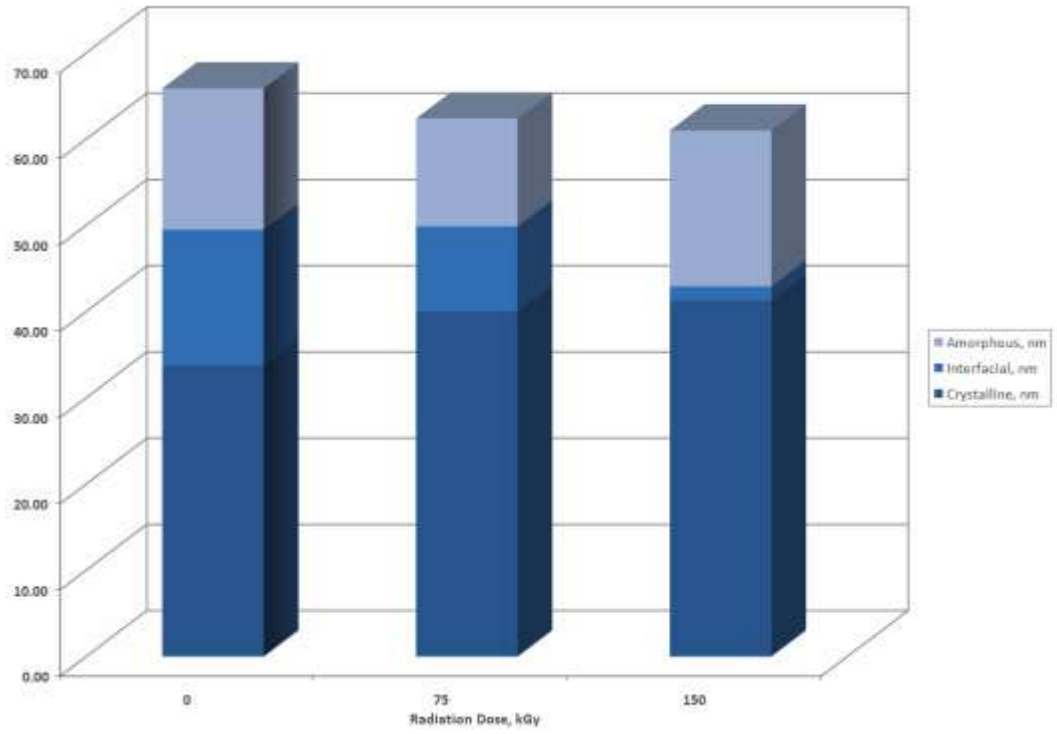

Figure 15: Three Phase Crystal Model for Low Dose Rate Gamma Irradiation

Table 7: Three Phase Model for High Dose Rate Gamma Irradiation on the Surface

Dose (kGy)	Crystalline, nm	Interfacial, nm	Amorphous, nm
0	33.7	15.8	16.4
75	39.1	5.4	18.4
150	41.6	5.1	16.8

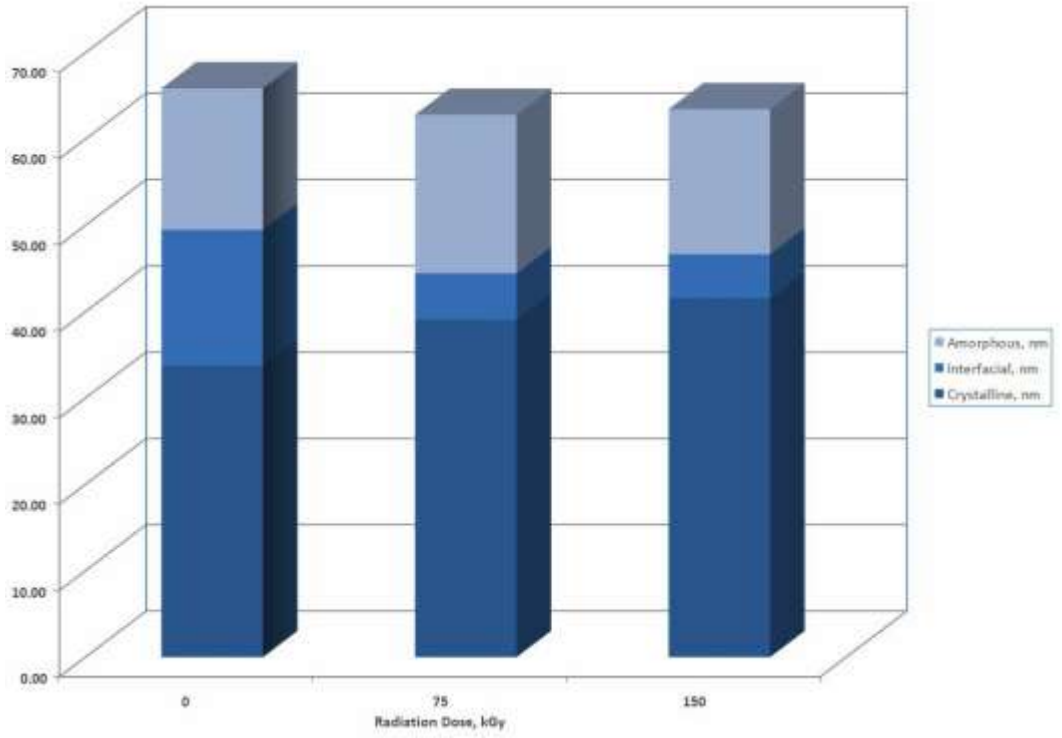

Figure 16: Three Phase Crystal Model for High Dose Rate Gamma Irradiation

4.1.3 Hardness Study

Irradiation of UHMWPE leads to an increase in hardness (Table 8 and Figure 17) of 24% at 75 kGy and 39% at 150 kGy. Irradiation also leads to an increase in modulus (Table 8 and Figure 18) of 24% at 75 kGy and 35% at 150 kGy. This increase in hardness and modulus can be explained using the three phase model developed in Section 4.1.2. Chain scissioning in the presence of oxygen, leads to formation of new crystals in the amorphous region and further crystallization of existing crystals at the interface. This further crystallization explains the increase in both hardness and modulus with increasing radiation dose. The breaking of constraints at the surface of the crystal (tie chains and loops) would also allow for further perfection of already existing crystals. This increased degree of uniformity in the crystal leads to a higher crystal hardness, H_c, as seen in Table 8. The H_c is dependent on the crystallite lamella thickness, l_c, and inversely dependent on the surface free energy of the crystal, σ_e, which means that by having an increase in H_c there is a combination of an increase in l_c and an increase in the perfection of the crystal (explained by the lowering of σ_e).

4.1.4 Molecular Motion Study

It can be seen that on the surface of the irradiated sample there are no significant changes in relaxation temperatures (Υ, β, or α), as displayed in Table 9, Figure 19, and Figure 20. This is due to the fact that there is negligible crosslinking on the surface of the irradiated sample. These results agree with the hourglass structure seen in the solubility study conducted in Section 4.1.1, that said that there was chain scissioning on the surface and crosslinking in the center of the sample.

4.1.5 Crystallite Thickness Study

The final study on the gamma irradiated samples is an in depth crystallite thickness analysis using the DSC at a very slow heating rate (1^oC/min). This study showed that on

the surface of the sample, there is a small uniform increase in crystallite thickness l_n, l_w, and l_z (45 ± 10%) distribution with the application of gamma irradiation independent of radiation dose, as seen in Figure 21 and Table 10. In the center of the sample, there is a significant dose and dose rate dependent increase in crystallite thickness distribution (l_n, l_w, and l_z), as seen in Figure 21 and Table 10. This is most noticeable in the l_z-distribution where the average irradiated surface l_z is 52% ± 18%, the average l_z for 75 kGy in the center is 77% ± 25%, and the average l_z for 150 kGy in the center is 145% ± 23%. On the surface of the sample, the PDI (l_w:l_n and l_z:l_n) remain similar to the control sample (l_w/l_n: 3% ± 3% and l_z/l_n: 4% ± 3%); however, in the center of the sample, the PDI increases significantly in the irradiated samples (l_z/l_n for 75 kGy is 18% ± 21% and l_z/l_n for 150 kGy is 35% ± 1%), as seen in Figure 22 and Table 10. In the center of the sample, there is very little increase in integral crystallinity (4% ± 3%), however there is a significant increase in crystallinity on the surface of the sample (27% ± 4%), as seen in Figure 23 and Table 10. The raw data used for these calculations is displayed in Table 11, Table 12, Table 13, and Table 14. Appendix I contains the DSC endotherms (Figure 30 to Figure 33) and crystallite thickness distributions (Table 23 and Figure 34 to Figure 89).

4.1.5.1 Surface

The changes on the surfaces of the samples agree with the results seen in the other studies (Sections 4.1.1, 4.1.2, 4.1.3, and 4.1.3), where chain scissioning of the tie chains and loops induce further crystallization. Since there is oxygen dissolved and accessible at the surface of the sample, the free-radicals in the amorphous region undergo chain scissioning which allow for new crystals to form in the unoriented amorphous phase. Since on the surface there are no constraints (crosslinks) in the amorphous phase, the primary site for new crystals is in the amorphous phase and not at the interface.

4.1.5.2 Center

In the center of the sample there is not the same availability of oxygen, so the amorphous region is expected to crosslink, as supported by the solubility study, seen in Section 4.1.1 and the literature as seen in Figure 4. This means that the required sequence length for crystallization is not available between crosslinks in the amorphous phase. This lack of the minimum required sequence crystallizable sequence length prevents nucleation of new crystals in the amorphous region and makes the main site of crystallization the surface of the already existing crystals (interface). This leads to the growth of larger crystals instead of the formation of new smaller crystals.

Table 8: Hardness and modulus dependence on gamma irradiation

Dose (kGy)	Plateau Hardness (MPa)	Plateau Modulus (MPa)	H_c (MPa)	Y (MPa)
0	38	1200	69.78	23.26
75	47	1490	71.56	23.85
150	53	1620	77.41	25.80

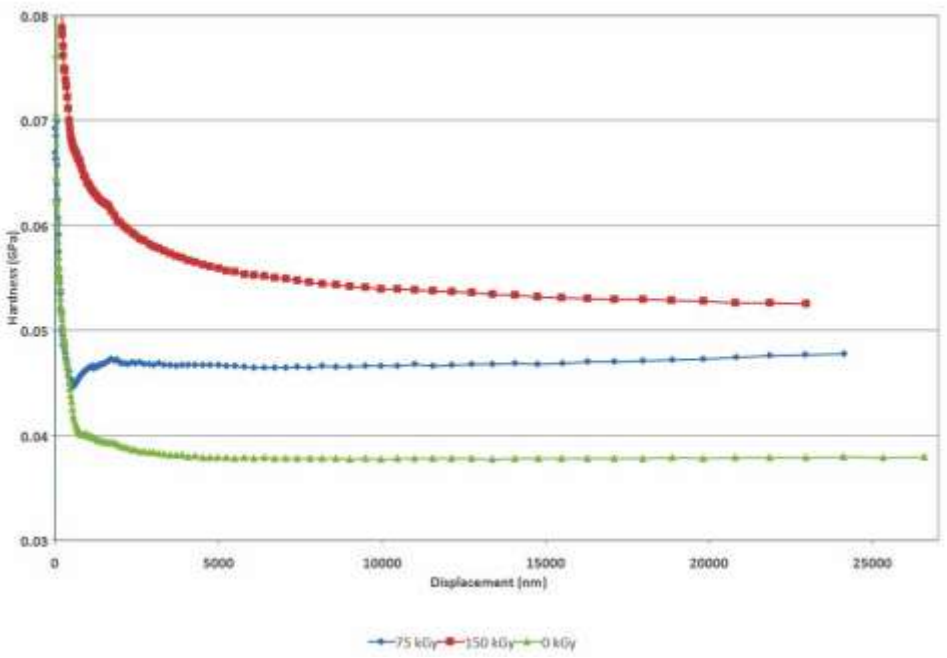

Figure 17: Effect of Integral Dose on Hardness as a Function of Depth

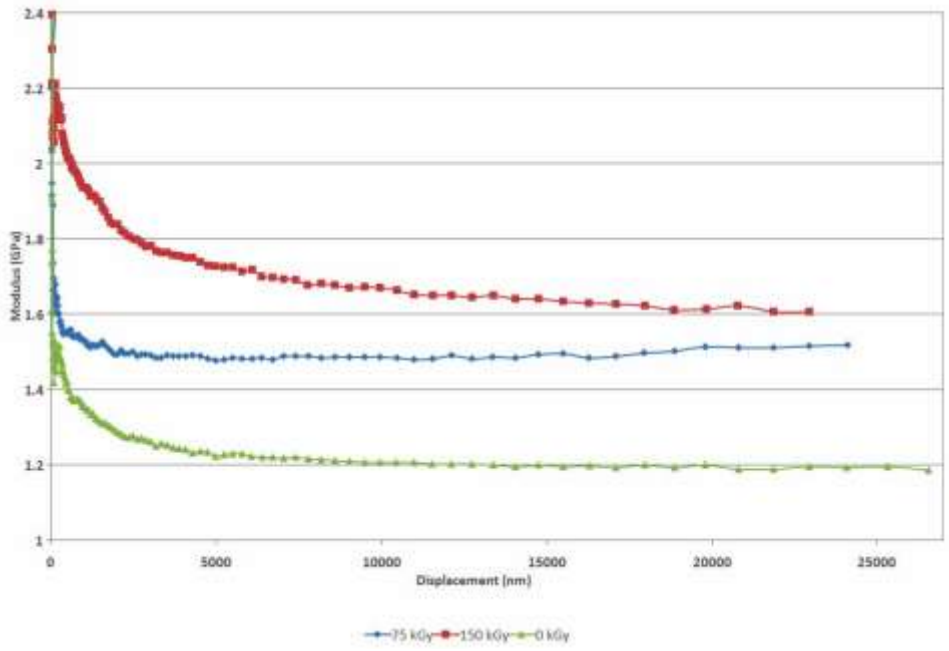

Figure 18: Effect of Integral Dose on Modulus as a Function of Depth

Table 9: DMTA Relaxation Temperatures at 1 Hz (^{o}C)

Sample	γ Relaxation	β Relaxation	α Relaxation
Control	-120	4	102
75 kGy	-117	3	93
150 kGy	-120	4	102

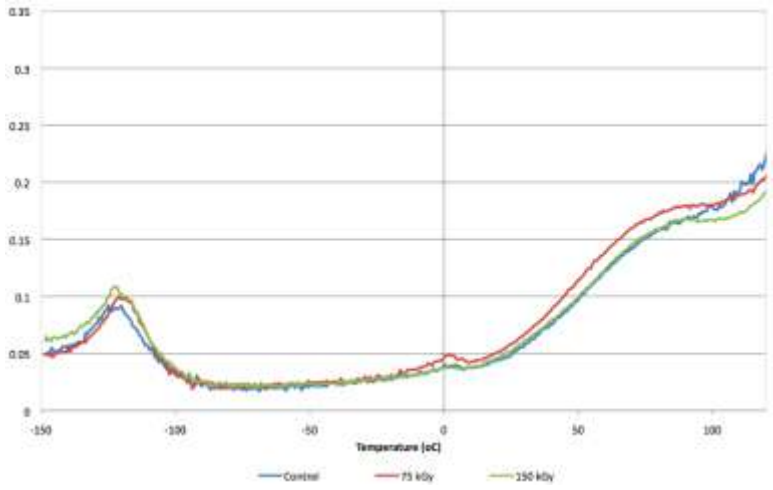

Figure 19: Tan Delta at 1 Hz

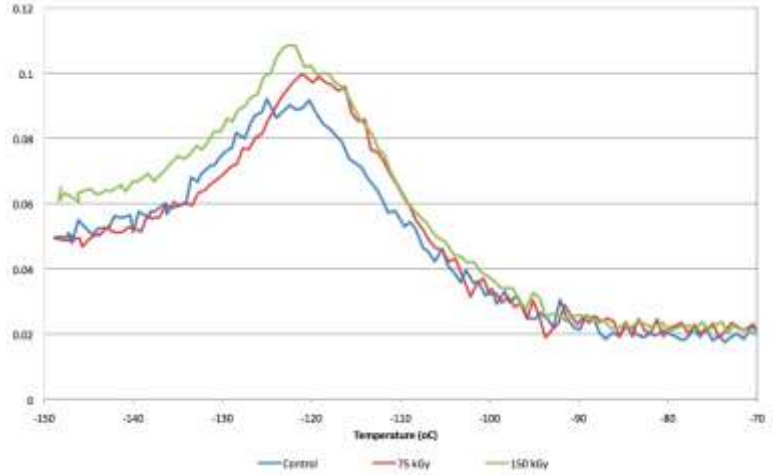

Figure 20: Gamma Relaxation in Tan Delta at 1 Hz

Table 10: Percentage Increase in crystallite thickness and polydispersity index from control

			l_n	l_w	l_z	l_w/l_n	l_z/l_n
75 kGy	Surface	HDR	41%	41%	42%	1%	1%
		LDR	42%	41%	42%	0%	0%
	Center	HDR	46%	83%	95%	25%	33%
		LDR	55%	57%	59%	2%	3%
150 kGy	Surface	HDR	37%	43%	44%	4%	5%
		LDR	60%	70%	78%	6%	11%
	Center	HDR	95%	131%	161%	18%	34%
		LDR	69%	94%	128%	15%	35%

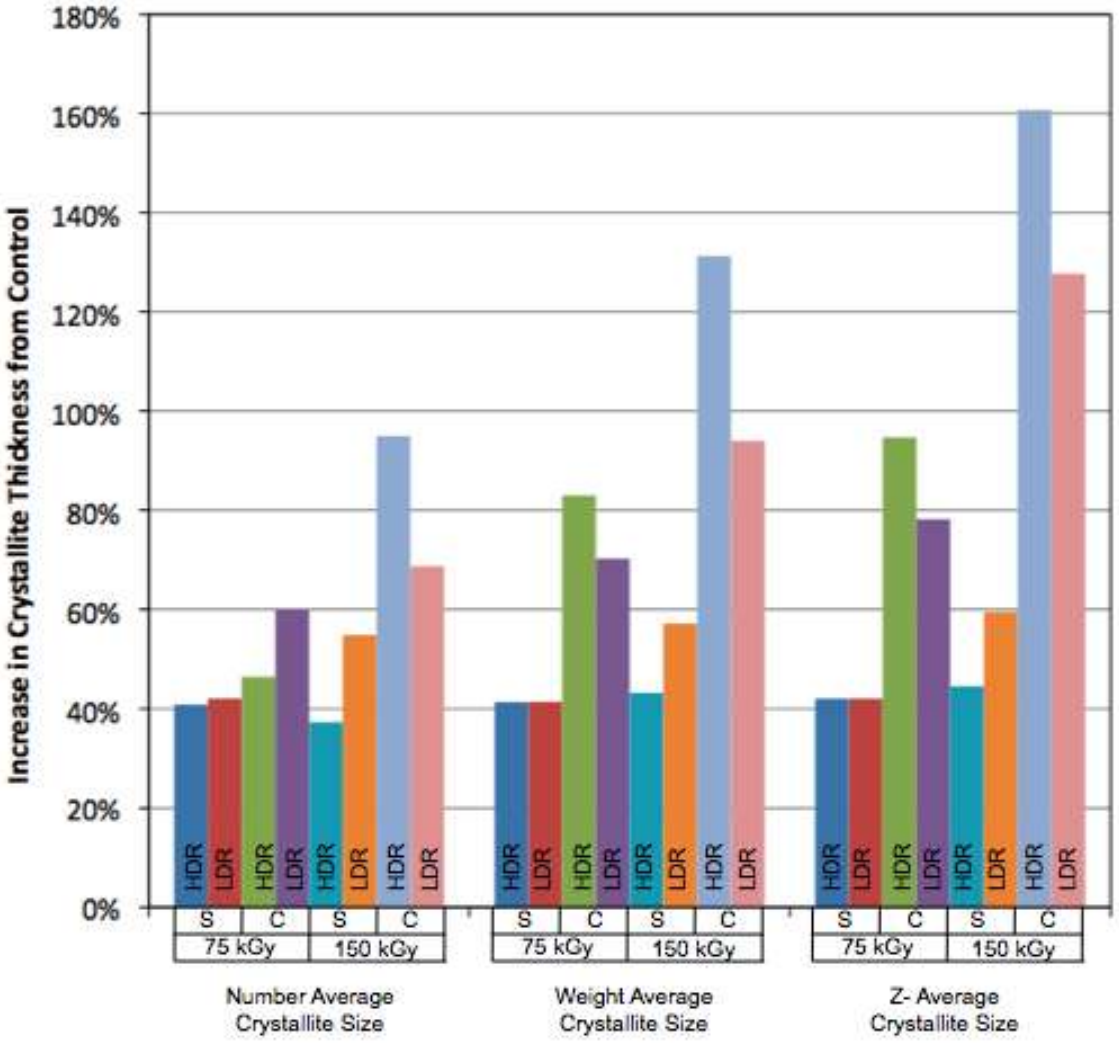

Figure 21: Increase in crystallite thickness compared to control for the number- average, weight-average, and z-average

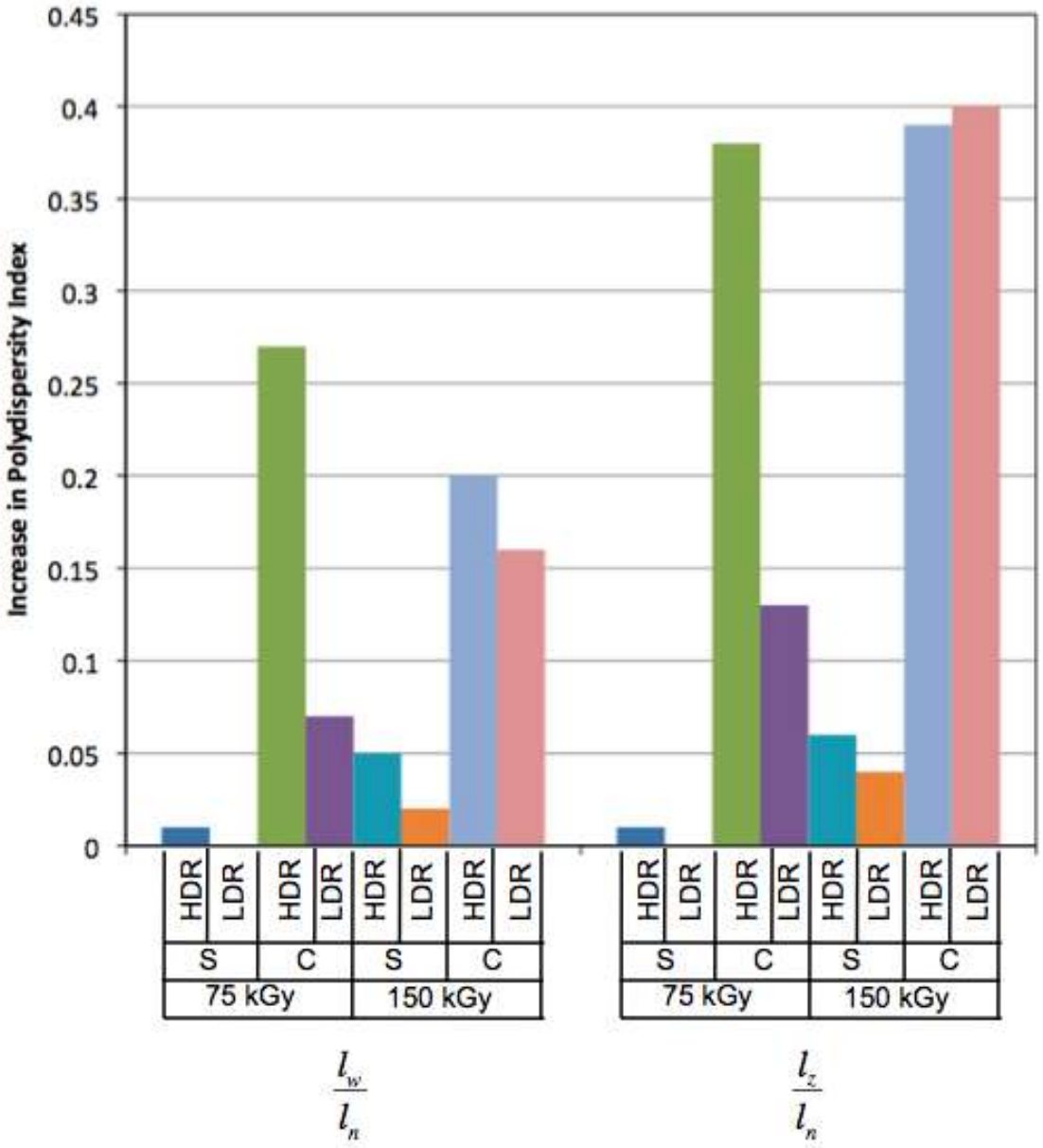

Figure 22: Comparison of the ratio of weight-average to number average crystallite thickness and the z-average ratio to the number-average

Table 11: Median Crystallite Thickness for the Surface of the Gamma High Dose Rate Irradiation Dose

Dose (kGy)	Crystallite Thicknesss Distribution, l_n	First Moment, l_w	Second Moment, l_z	l_w/l_n	l_z/l_n
0	19.16	21.55	23.00	1.12	1.20
75	26.98	30.46	32.66	1.13	1.21
150	26.30	30.86	33.24	1.17	1.26

Table 12: Median Crystallite Thickness for the Surface of the Gamma Low Dose Rate Irradiation Dose

Dose (kGy)	Crystallite Thicknesss Distribution, l_n	First Moment, l_w	Second Moment, l_z	l_w/l_n	l_z/l_n
0	19.16	21.55	23.00	1.12	1.20
75	27.21	30.47	32.66	1.12	1.20
150	29.67	33.87	36.69	1.14	1.24

Table 13: Median Crystallite Thickness for the Center of the Gamma High Dose Rate Irradiation Dose

Dose (kGy)	Crystallite Thicknesss Distribution, l_n	First Moment, l_w	Second Moment, l_z	l_w/l_n	l_z/l_n
0	20.52	22.19	23.42	1.08	1.14
75	30.04	40.61	45.60	1.35	1.52
150	40.01	51.32	61.06	1.28	1.53

Table 14: Median Crystallite Thickness for the Center of the Gamma Low Dose Rate Irradiation Dose

Dose (kGy)	Crystallite Thicknesss Distribution, l_n	First Moment, l_w	Second Moment, l_z	l_w/l_n	l_z/l_n
0	20.52	22.19	23.42	1.08	1.14
75	32.81	37.78	41.74	1.15	1.27
150	34.62	43.05	53.33	1.24	1.54

Table 15: Comparison of cyrstallinity at different depths and dose rates

Dose (kGy)	Low Dose Rate		High Dose Rate	
	Surface	Center	Surface	Center
0	51.22%	55.61%	51.22%	55.61%
75	64.15%	56.92%	62.21%	56.25%
150	67.65%	59.72%	65.53%	57.70%

Table 16: Comparison of crystallizable fraction and sequence length at different depths and dose rates

Dose (kGy)	Crystallizable Fraction				Sequence Length			
	Low Dose Rate		High Dose Rate		Low Dose Rate		High Dose Rate	
	Surface	Center	Surface	Center	Surface	Center	Surface	Center
0	0.961	0.963	0.961	0.963	75	80	75	80
75	0.972	0.975	0.972	0.977	107	118	106	129
150	0.975	0.981	0.971	0.978	116	157	103	136

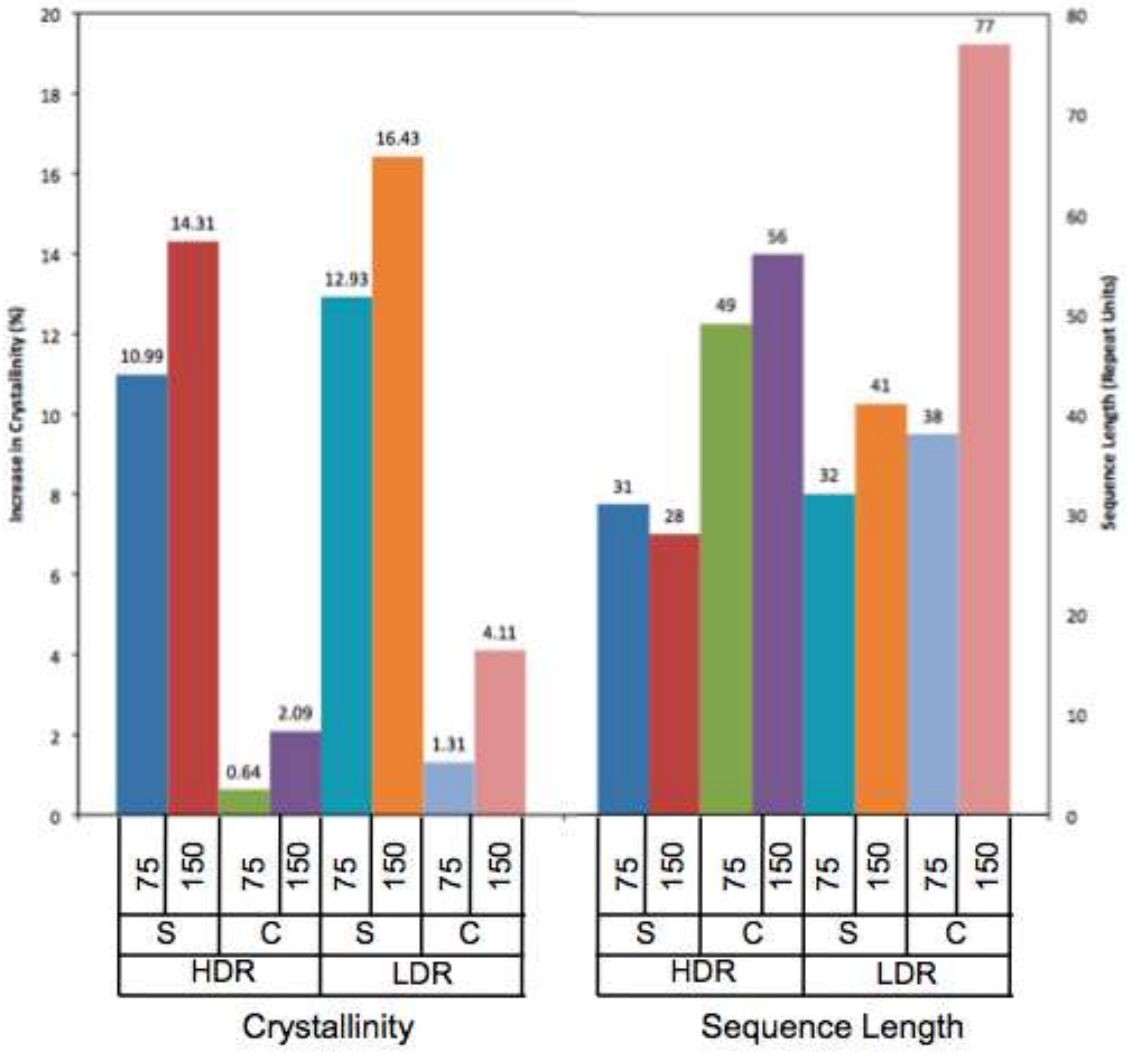

Figure 23: Comparison of crystallinity and sequence length

4.2 Proton Irradiation

4.2.1 Solubility Study

At 1.03 kGy there is a significant change induced in the amorphous region of the proton-irradiated polymer, as seen by the swell ratio's (Table 17) decrease from 34 to 2. This decrease in swell ratio is caused by crosslinking in the amorphous region which leads to a high gel fraction. The percent extract (Table 17) is also very low, which signifies a very low sol fraction for the polymer to chain scission (percent extract of 0.34%).

4.2.2 Three-Phase Crystallite Model

The three-phase crystallite model, Table 19 and Figure 24, show a significant decrease in the interfacial region (14 nm to 9 nm) with radiation, which can be explained by chain scission of the tie chains and loops in the interfacial region leading to further crystallization at the already existing crystal surface.

4.2.3 Crystallite Thickness Study

4.2.3.1 Thermal Analysis of Post-Irradiated Samples (Run 1)

There is a dose dependent increase in crystallite thickness, (best illustrated by looking at the second moment of the crystallite thickness, l_z) where the percent increase for the samples irradiated at 1.77 ± 1.2 kGy is 12% and the percent increase for the samples irradiated at 7.93 ± 1.0 is 22%, as seen in Table 20, Table 21, and Figure 25. The change in crystallite PDI (l_z/l_n for 1.77 kGy is -5% and l_z/l_n for 7.93 kGy is 1%) is assumed to be within experimental error, as seen in Table 20, Table 21, and Figure 26. The change in crystallinity is assumed to be within experimental error (-3% for 1.77 kGy and 3% for 7.93 kGy), as seen in Table 22 and Figure 27. These results would be explained by uniform growth of all existing crystals and no formation of new crystals. This would be facilitated by the breaking of tie chains and loops on the surface of the crystal, allowing

for the molecular mobility needed for crystal growth. Appendix II contains the DSC crystallite thickenss distributions (Table 24, Table 26 to Table 29, Figure 90 to Figure 104, and Figure 120 to Figure 168)

4.2.3.2 Thermal Analysis of Post-Heat Treated Samples (Run 2)

After all crystals were melted (erasing the thermal history of the samples) the samples were cooled at 1^{o}C/min and then reanalyzed with all samples having the same thermal history. At low irradiation doses (1.77 kGy), it can be seen that there is very limited changes in crystallite thickness from the control samples (l_z value of -3%), as seen in Table 20, Table 21, and Figure 25. In the high dose samples (7.93 kGy) there is a very significant decrease in crystallite thickness (l_z value of -34%), as seen in Table 20, Table 21, and Figure 25. The change in the crystallite thickness PDI was within experimental error (l_z/l_n for 1.77 kGy is 2% and l_z/l_n for 7.93 kGy is -4%), as seen in Table 20, Table 21, and Figure 26. The change in crystallinity is assumed to be within experimental error (7% for 1.77 kGy and -5% for 7.93 kGy), as seen in Table 22 and Figure 27. Using the change in crystallite thickness, the change in sequence length can be determined. There is a small decreases in the 1.77 kGy crystal sequence length of -4%, as seen in Table 22 and Figure 27. There is a much larger decrease in crystallizable sequence length in the 7.93 kGy samples of -31% (68 repeat units in control to 47 repeat units in the irradiated sample), as seen in Table 22 and Figure 27. This change in crystallizable sequence length, which is dependent on the distance between crosslinks is what controls the crystallite thickness in the second heating. Appendix II contains the DSC crystallite thickness distributions (Table 25, Table 31, Figure 105 to Figure 119, and Figure 169 to Figure 217).

Table 17: Swell ratio and % extract for proton irradiated UHMWPE

	Swell Ratio	% Extract
Control	34.09	
Proton Irradiated (1.03 ± 0.1 kGy)	1.98 ± 0.17	0.35 ± 0.66

Table 18: WAXD and DSC crystallinity for proton irradiated UHMWPE

	WAXD Crystallinity	DSC Crystalinity
Control	76.66 ± 2.08	55.97 ± 0.92
Proton Irradiated (1.03 ± 0.1 kGy)	70.64 ± 1.01	59.77 ± 1.78

Table 19: Three-phase crystallite model for proton irradiate UHMWPE

	Long Period (nm)	Amorphous (nm)	Crystalline (nm)	Interface (nm)
Control	65.88 ± 0.5	15.38 ± 1.4	36.87 ± 0.7	13.63 ± 1.5
Proton Irradiated (1.03 ± 0.1 kGy)	62.83 ± 0.0	16.65 ± 2.1	37.08 ± 1.1	9.09 ± 2.4

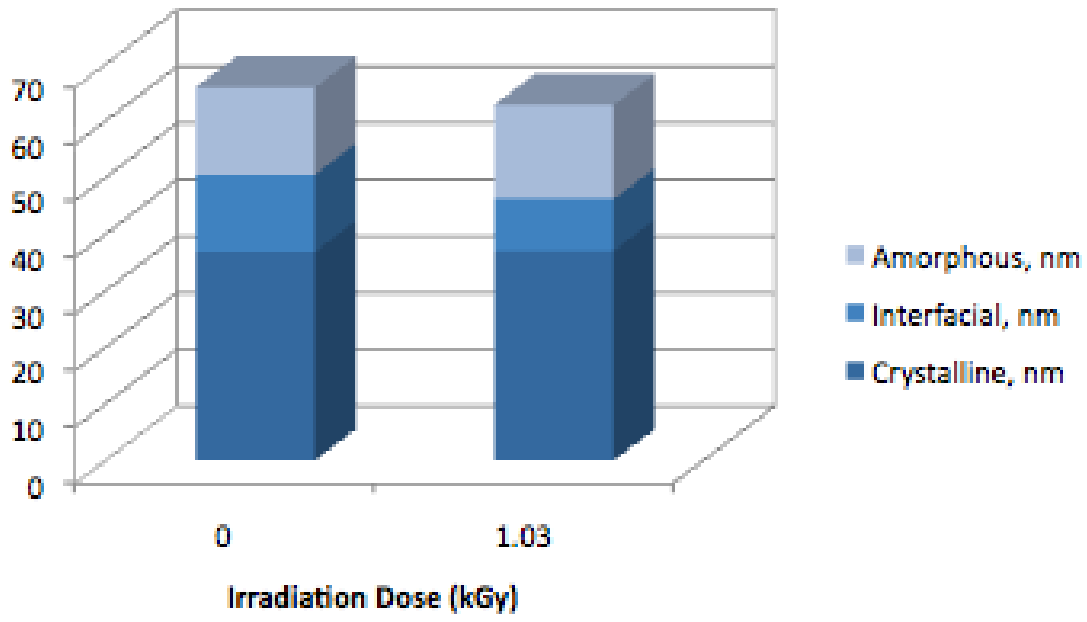

Figure 24: Three phase crystaline model for proton irradiaton

Table 20: Median Crystallite Thicknesses for Proton Irradiated Samples in the First DSC Run

Dose (kGy)	Crystallite Thicknesss Distribution, l_n	First Moment, l_w	Second Moment, l_z	l_w/l_n	l_z/l_n
0	21.00 ± 3.78	24.93 ± 3.33	25.24 ± 2.72	1.19	1.20
1.77 ± 1.2	24.97 ± 1.29	27.03 ± 1.18	28.41 ± 1.38	1.08	1.14
7.93 ± 1.0	25.56 ± 1.88	28.78 ± 2.35	30.81 ± 2.67	1.13	1.21

Table 21: Median Crystallite Thicknesses for Proton Irradiation Samples in the Second DSC Run

Dose (kGy)	Crystallite Thicknesss Distribution, l_n	First Moment, l_w	Second Moment, l_z	l_w/l_n	l_z/l_n
0	17.41 ± 1.82	18.98 ± 2.96	20.09 ± 2.60	1.09	1.15
1.77 ± 1.2	16.62 ± 0.76	18.43 ± 0.62	19.57 ± 0.71	1.11	1.18
7.93 ± 1.0	12.04 ± 0.18	12.76 ± 0.18	13.27 ± 0.19	1.06	1.10

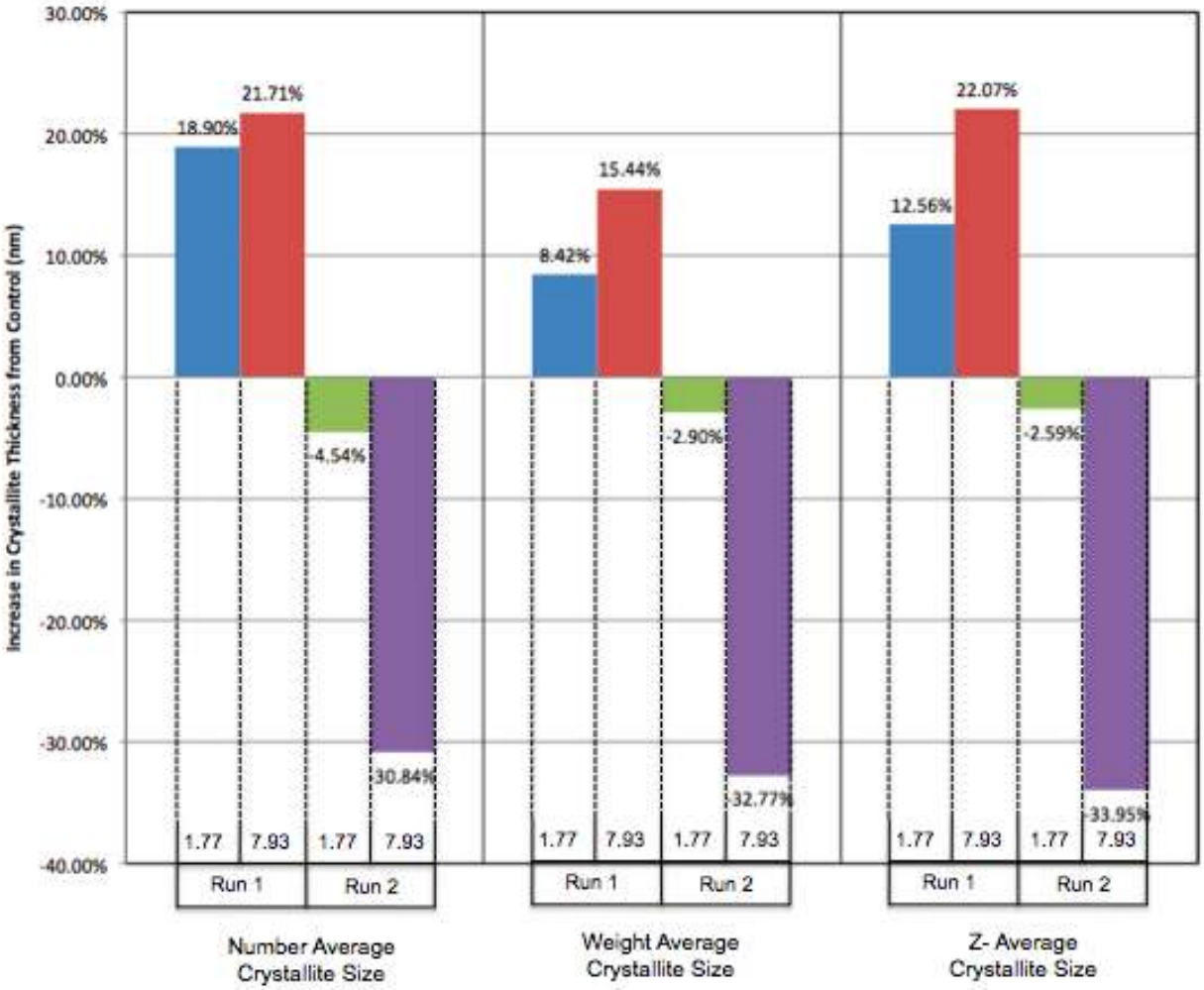

Figure 25: Crystallite thicknesses for proton irradiated UHMWPE

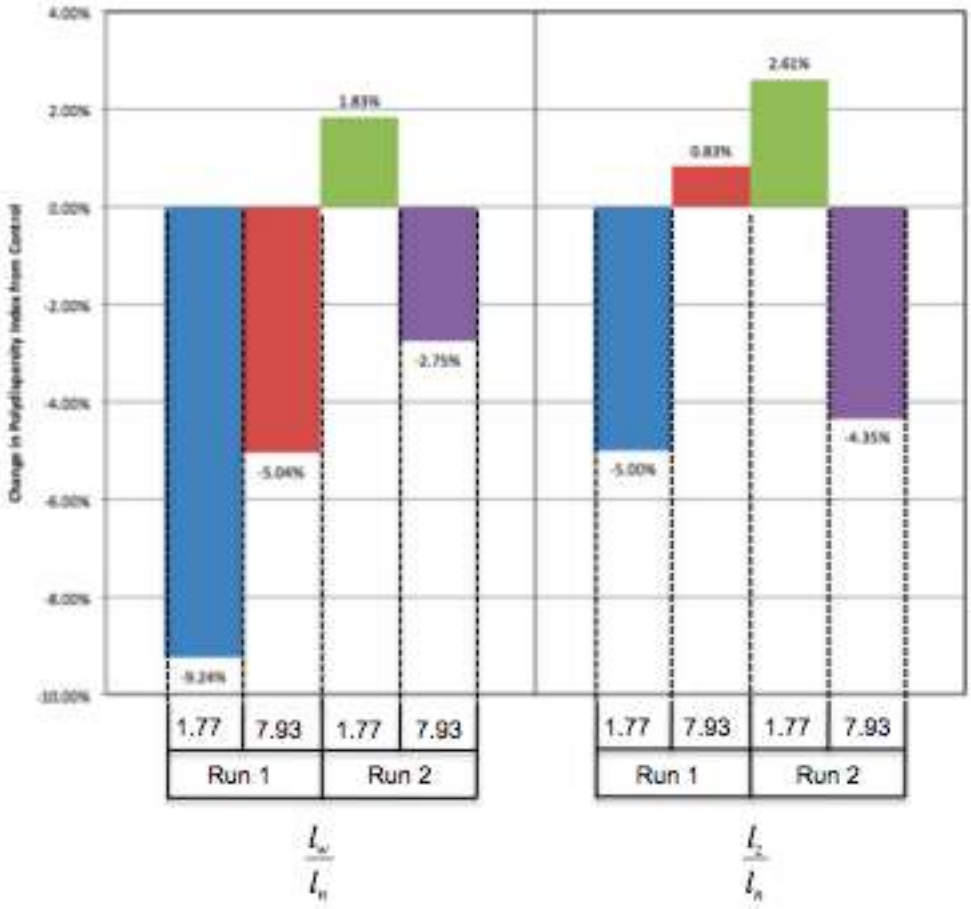

Figure 26: Crystallite polydispersity for proton irradiated UHMWPE

Table 22: Crystallintiy, crystallizable fraction, and sequence length for proton irradiated UHMWPE

Dose (kGy)	Crystallinity		Crystallizable Fraction		Sequence Length	
	Run 1	Run 2	Run 1	Run 2	Run 1	Run 2
0	60 ± 9%	58 ± 3%	0.964	0.956	82	68
1.77 ± 1.2	58 ± 3%	62 ± 4%	0.970	0.954	98	65
7.93 ± 1.0	62 ± 5%	55 ± 4%	0.971	0.937	100	47

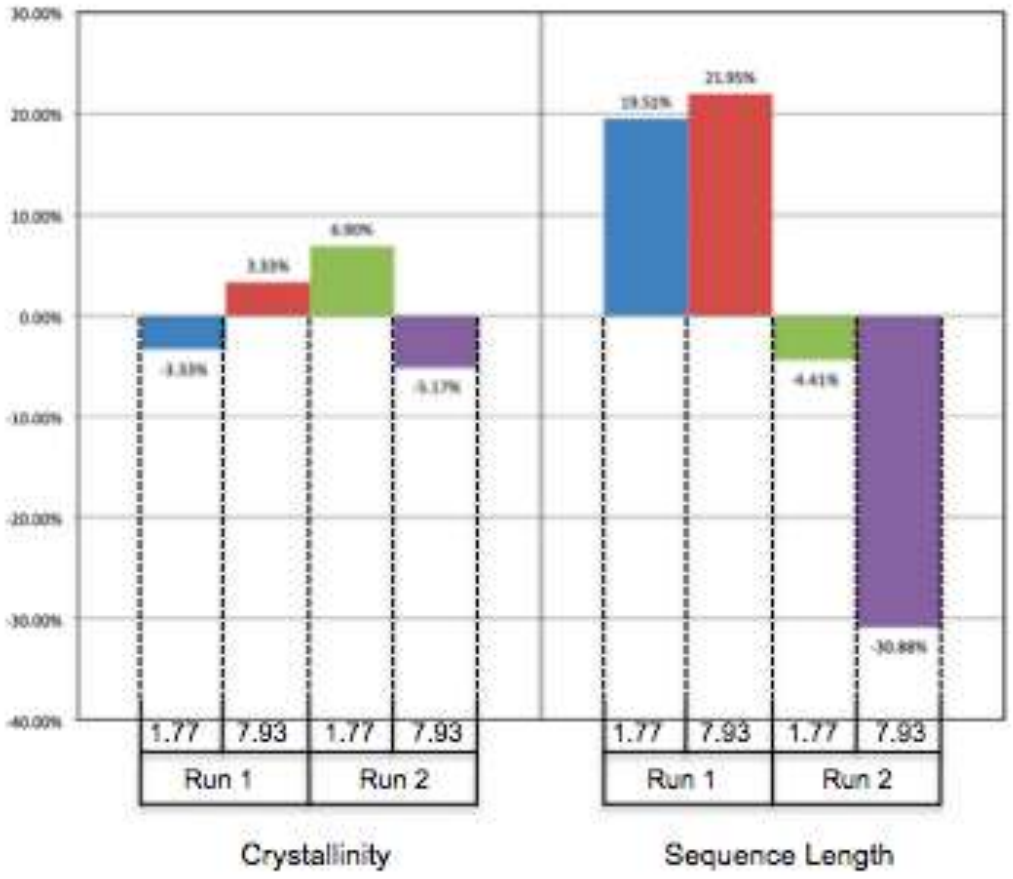

Figure 27: Crystallinity and sequence length for proton irradiated UHMWPE

5 Conclusions

5.1 General Conclusions

A new method has been developed to analyze DSC data based on crystallite thickness that generates crystallite thicknesses (number-average, weight-average, and z-average) and the lamella thickness polydispersity index, PDI (l_w/l_n and l_z/l_n). This new analysis method agrees with all other experiments conducted on the samples (solubility, molecular mobility, and three-phase model analysis).

5.2 Gamma Irradiated Conclusions

The combined studies of the gamma irradiated samples shows that chain scission occurs on the surface and crosslinking in the center. The chain scissioning on the surface of the sample creates the molecular mobility needed in the amorphous region to form new crystals and breaking of the tie chains and loops in the interface that allow for growth of already existing crystals. The formation of new crystals and growth of existing crystals leads to an increase in crystallinity. This increase in crystallinity leads to an increase in hardness and modulus. In the center of the sample there is crosslinking in the amorphous region and breaking of tie chains and loops in the interface; this combination leads to growth of already existing crystals.

5.3 Proton Irradiated Conclusions

The combined studies of the proton irradiated samples show that crosslinking occurs in the amorphous region and breaking of the tie chains and loops causes the growth of the already existing crystals. Both the degree of crosslinking and the growth of the crystals is highly dependent on integral proton dose.

6 Future Work

Fundamental Study: Heat-treated Gamma Irradiated UHMWPE

Compression molded samples of UHMWPE will be irradiated with gamma irradiation in an inert atmosphere (Doses: 20, 100, and 150 kGy and Dose Rates: 0.25 kGy/hr and 2.9 kGy/hr). While still in the inert atmosphere, the samples will go through a heat-treatment to a temperature above their melting point (430 K) followed by controlled cooling (either quenched or slow cooled) to room temperature. This heat-treatment will remove the free radicals that are trapped in the crystalline region after irradiation. The samples will be characterized by the thermal and morphological methods discussed in this dissertation, fatigue lifetime, fatigue crack propagation, fracture toughness, and a pin-on-disc wear study

Fundamental and Applied Study: Molecular Mechanisms of Wear Particle Generation

Following the techniques developed by Zhurkov [32], it is possible to understand the micromechanics associated with wear particle generation. Using electron spin resonance (ESR), it is possible to calculate the number of chains that undergo hemolytic chain scission during the wear process. Using FTIR, it is possible to detect the shift in vibrational bands with applied load and the creation of oxidized chains ends following chain scission. Using small angle x-ray/ neutron scattering, it is possible to detect the development of microcracks formed in the polymer at different stages of the wear process. These experiments will be conducted on UHMPWE that is gamma irradiated at 0, 20, 100, and 150 kGy in

disc form for pin-on-disc wear testing and flat tensile specimens for tensile and fatigue testing.

Medical Application: Wear Properties of Textured Gamma Irradiated UHMWPE

According to Muratoglu et. al, gamma irradiated UHMWPE (150 kGy) still had the original machining marks visible at 2 million cycles [33]. This implies that if we placed a texture on the highly crosslinked UHMWPE, that that texture would remain well into the lifetime of the implant. This texturing has been attempted by our group on a non-irradiated polished UHMWPE surface by direct laser texturing using a femtosecond laser, as seen in Figure 28 and Figure 29 [34]. However, the direct laser texturing does not lend itself to mass production. Therefore, this should be accomplished by a mold-replicate method. A highly polished metallic mold will be laser textured using a laser. The UHMWPE will then be compression molded using this surface as one side of the mold, thereby creating the inverse image of the mold surface. After the textured UHMWPE surface is created it will be gamma irradiated at 20, 100, and 150 kGy in an inert atmosphere. While still in the inert atmosphere, the textured UHMWPE will undergo a thermal treatment that takes the polymer above its melting point to quench all free-radicals trapped in the crystalline region. Since UHMWPE's molecular weight does not allow flow in the molten state, even the non-irradiated sample will maintain the textured surface. This textured crosslinked UHMWPE surface would be composed of cylinders with inter-connected channels running between to allow lubricant to flow more freely between the UHMWPE and the metallic counterface. These textured surfaces will undergo pin-on-disc wear testing, morphology, and fatigue characterization.

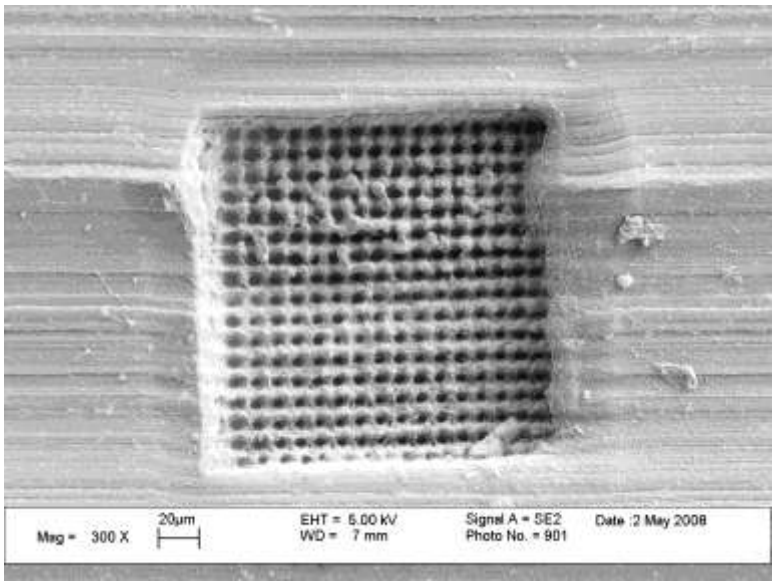

Figure 28: Femtosecond laser textured UHMWPE [34]

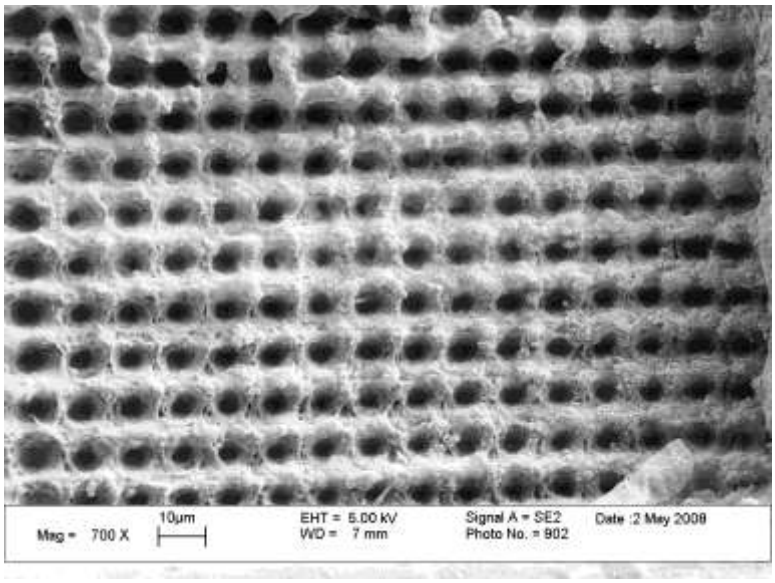

Figure 29: Femtosecond laser textured UHMWPE (Zoom) [34]

List of References

1. Kurtz, S, *The UHMWPE Handbook*. 2004, Amsterdam: Elsevier.

2. Landy, MMaW, P.S., J. Arthroplasty (suppl.), 1988. **S73**.

3. Wright, TM, C.M. Rinmac, S.D. Stulberg, Clinical Orthop. Rel. Res. 276, 1992. **126**.

4. Schmidt, MA, *Surface texture and micromechanics of ultra high molecular weight polyethylene (UHMWPE) orthopaedic implant bearings*, in *Materials Science and Engineering*. 2001, The University of Tennessee: Knoxville.

5. Shah, J and M Fuzail, *Examination of long-lived, oxygen-induced radicals in irradiated ultra-high molecular weight polyethylene.* Nucl. Instrum. Methods Phys. Res., Sect. B, 2007. **265**: 67-71.

6. Lewis, G, *Properties of crosslinked ultra-high-molecular-weight polyethylene.* Biomaterials, 2001. **22**: 371-401.

7. Schmidt, M, Trans. Soc. Biomaterials, Hawaii, 2000.

8. Premnath, V, W. Harris, M. Jasty, E. Merrill, *Gamma sterilization of UHMWPE articular implants: an analysis of oxidation problems.* Biomaterials, 1996. **17**: 1741-53.

9. Auerbach, I. *Irradiated polyethylene II- free radical formation*. in *Fall Meeting of the American Chemical Society*. 1962. Atlantic City, NJ.

10. Patel, G and A Keller, *Crystallinity and the Effect of Ionizing Radiation in Polyethylene. I. Crosslinking and the Crystal Core.* Journal of Polymer Science: Polymer Physics Edition, 1975. **13**(2): 303-21.

11. VanKrevelen, D, *Properties of Polymers*. 1997, San Diego, CA: Elsevier.

12. Blanchet, T and B Burroughs, *Numerical Oxidation Model for Gamma Radiation-Sterilized UHMWPE: Consideration of Dose-Depth Profile.* Journal of Biomedical Materials Research, 2001. **58**: 684-93.

13. Zhu, L, F-C Chiu, Q Fu, RP Quirk, et al, *Physical constants of poly(ethylene)*, in *Polymer Handbook*, A Abe, et al, Editors. 1999, John Wiley and Sons, Inc.: New York.

14. Patel, G, *Crystallinity and the Effect of Ionizing Radiation in Polyethylene. IV. Effect of Segregation of Low Molecular Weight Chains on Determination of Main-Chain Scission in Linear Polyethylene.* Journal of Polymer Science: Polymer Physics Edition, 1975. **13**(2): 303-21.

15. Wert, J, *Materials science and engineering laboratories*, in *Chapter 2: X-ray diffraction laboratory: Techische Univertitat Darmstadt.*

16. Hama, H and K Tashiro, *Structural changes in isothermal crystallization process of polyoxymethylene investigated by time-resolved FTIR, SAXS and WAXS measurements.* Polymer, 2003. **44**: 6973–88.

17. Shibata, N, N Tomita, N Onmori, K Kato, et al, *Defect initiation at subsurface grain boundary as a precursor of delamination in ultrahigh moleculat weight polyethylene.* Journal of Biomedical Materials Research, 2003. **67A**: 276-84.

18. Mansur, L, *Assessment of shielding material performance for deep space missions*, in *Materials for space applications*, M Chipara, Editor. 2005, Materials Reserach Society: Warrendale, PA.

19. Banks, B, K Groh and S Miller, *Low earth orbital atomic oxygen interactions with spacecraft materials*, in *Materials for space applications*, M Chipara, Editor. 2005, Materials Reserach Society: Warrendale, PA.

20. Crist, B and F Mirabella, *Crystal thickness distribution from melting homopolymers or random copolymers.* Journal of Polymer Science: Part B: Polymer Physics, 1999. **37**: 3131-40.

21. Valles-Llunch, A, L Contat-Rodrigo and A Ribes-Greus, *Differential scanning Calorimetry studies on high- and low-density annealed and irradiated polyethylenes: Influence of aging.* Journal of Applied Polymer Science, 2003. **89**: 3260-71.

22. Cook, J, *The morphology of nascent and molded ultra-high molecular weight polyethylene. Insights from solid-state NMR, nitric acid etching, GPC and DSC.* Polymer, 2000. **41**: 8615-23.

23. Flory, P, Trans. Faraday Soc., 1995. **51**: 848.

24. Wignall, GD, *Neutron and X-Ray Scattering*, in *Physical Properties of Polymer Handbook*, JE Mark, Editor. 1996, American Institute of Physics: Woodbury, New York. p. 299-310.

25. Kim, M-H, *The melting behavior and structure of ethylene copolymers from metallocene catalysts*, in *Materials Science and Engineering*. 1996, The University of Tennessee: Knoxville.

26. Thomas, SG, *Influence of silicon concentration on the nanoindentation and nanoscatch behavior of pyrolytic carbon*, in *Materials Science and Engineering*. 2000, University of Tennessee: Knoxville.

27. Santa Cruz, C, F.J. Balta Calleja, T. Asano, I.M. Ward, *Plastic deformation in polyethylene crystals studied by microindentation hardness.* Philosophical Magazine A, 1993. **68**(1): 209-24.

28. Balta Calleja, FJ, L. Giri, I.M. Ward, D.L.M. Cansfield, *Microstructure of Bulk Crystallized Linear Polyethylene: Correlation of Microhardness and Yield Stress.* Journal of Materials Science, 1995. **30**: 1139-43.

29. Rodriguez-Lorenzo, LM, A.J. Salinas, M. Vallet-Regi, J. San Roman, *Composite biomaterials based on ceramic polymers. I. Reinforced systemsbased on Al_2O_3/PMMA/PLLA.* Journal of Biomedical Materials Research, 1996. **30**: 515-22.

30. Popli, R, M Glotin, L Mandelkern and RS Benson, *Dynamic mechanical studies of a and b relaxations of polyethylene.* Journal of Polymer Science B: Polymer Physics, 1984. **22**: 407-48.

31. Boyd, RH, *Relaxation processes in crystalline polymers: experimental behaviour-a review.* Polymer, 1985. **26**: 323-47.

32. VonSchmeling, H, *The role of chain length and conformation in stress-transmission and fracture of thermoplastic polymers.* Physics of the Solid State, 2005. **47**(5): 934-41.

33. Muratoglu, OK, D.O. O'Connor, C.R. Bragdon. M. Jasty, W.H. Harris. *Effect of cross-linking on the wear behavior of ultra high molecular weight polyethylene (UHMWPE) used in total joint replacemnets*. in *11th Conference of the ESB*. 1998. Toulouse, France.

34. Fernandez, P, *Micropatterning of UHMWPE using a femtosecond laser*, in *Materials Science and Engineering*. 2008, The University of Tennessee: Knoxville.

Appendix

1 Appendix I: Gamma Irradiation Data

1.1 Thermal Analysis

1.1.1 High Dose Rate

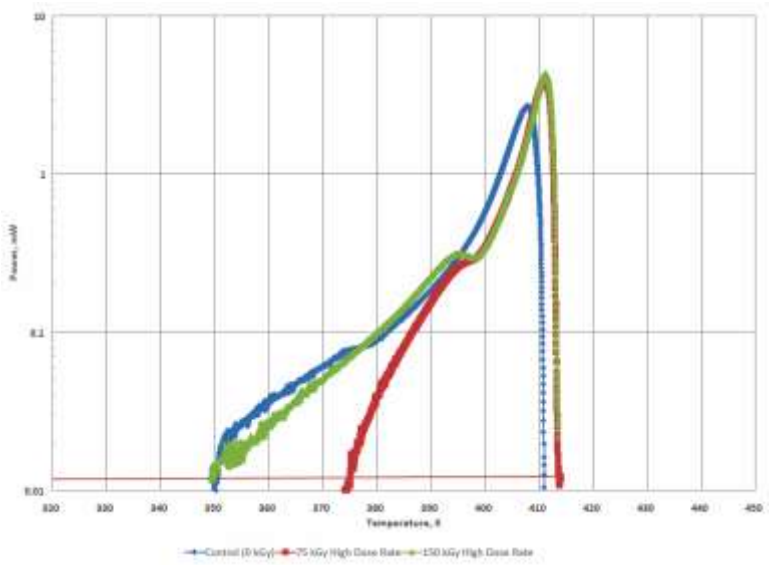

Figure 30: Endotherm for the Surface of High Dose Rate Irradiation

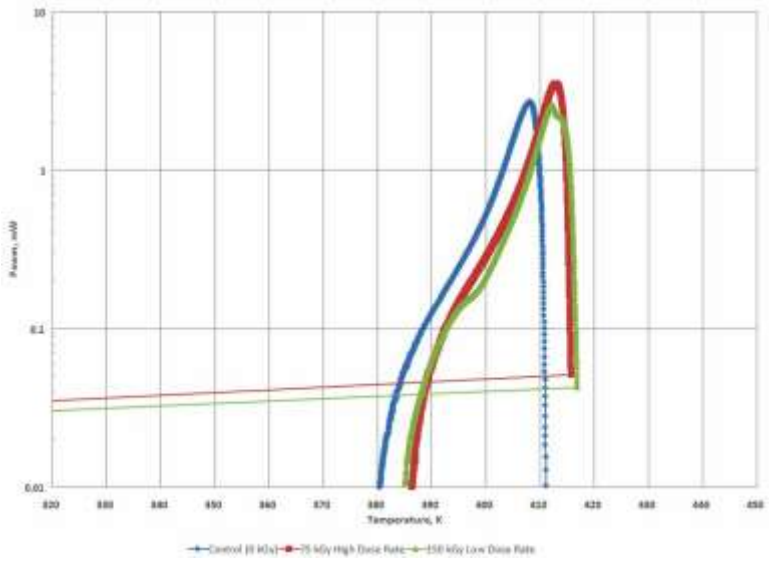

Figure 31: Endotherm for the Center of High Dose Rate Irradiation

1.1.2 Low Dose Rate

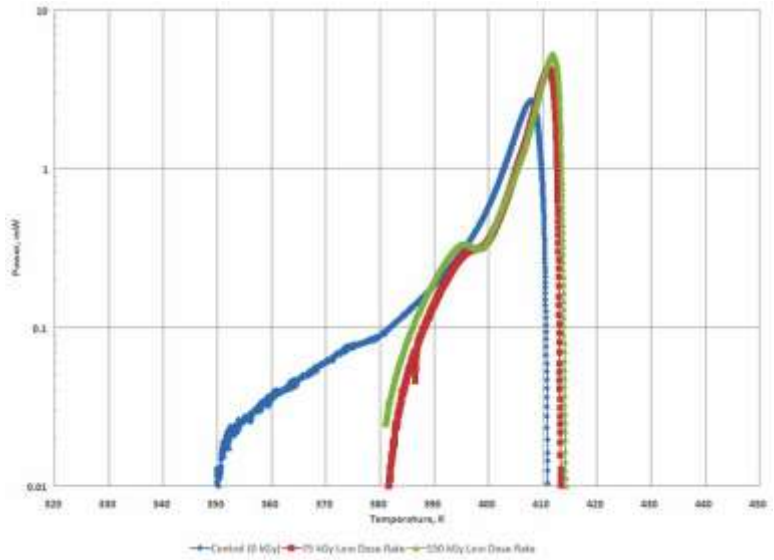

Figure 32: Endotherm for the Surface of Low Dose Rate Irradiation

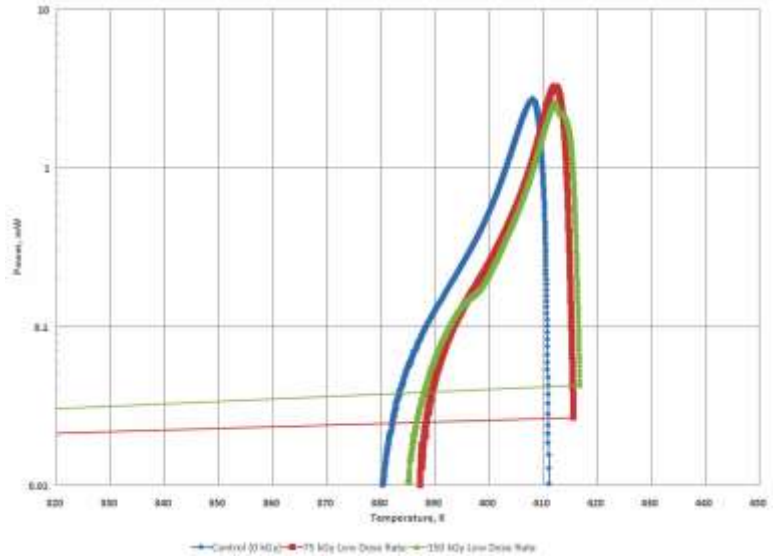

Figure 33: Endotherm for the Center of Low Dose Rate Irradiation

1.2 Crystallite Thickness Distribution

Table 23: Median and Maximum Crystallite Thickness for Gamma Irradiation

		Control		75 kGy				150 kGy			
				Low Dose Rate		High Dose Rate		Low Dose Rate		High Dose Rate	
		Surface	Center	Surface	Center	Surface	Center	Surface	Center	Surface	Center
Crystallite Thickness Distribution	Middle	19.16	20.52	27.21	32.81	26.98	30.04	29.67	34.62	26.30	40.01
	Maximum	32.64	33.42	48.00	83.61	47.30	86.65	57.33	138.41	48.65	137.90
First Moment	Middle	21.55	22.19	30.47	37.78	30.46	40.61	33.87	43.05	30.86	51.32
	Maximum	33.34	33.57	48.15	85.43	51.49	86.65	57.97	139.64	49.89	140.40
Second Moment	Middle	23.00	23.42	32.66	41.74	32.66	45.60	36.69	53.33	33.24	61.06
	Maximum	33.77	34.15	50.00	85.89	55.47	87.14	60.42	139.64	51.02	140.40

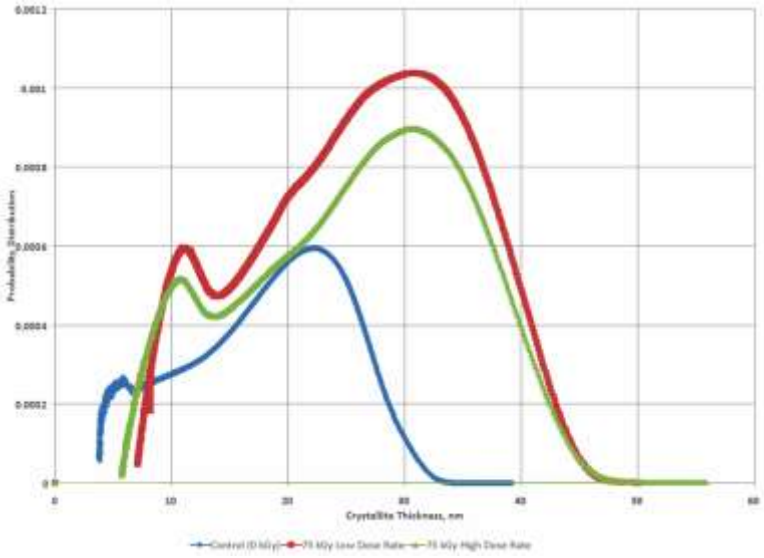

Figure 34: Effect of Dose Rate on the Surface of the 75 kGy Gamma Irradiated Crystallite Thickness Distribution

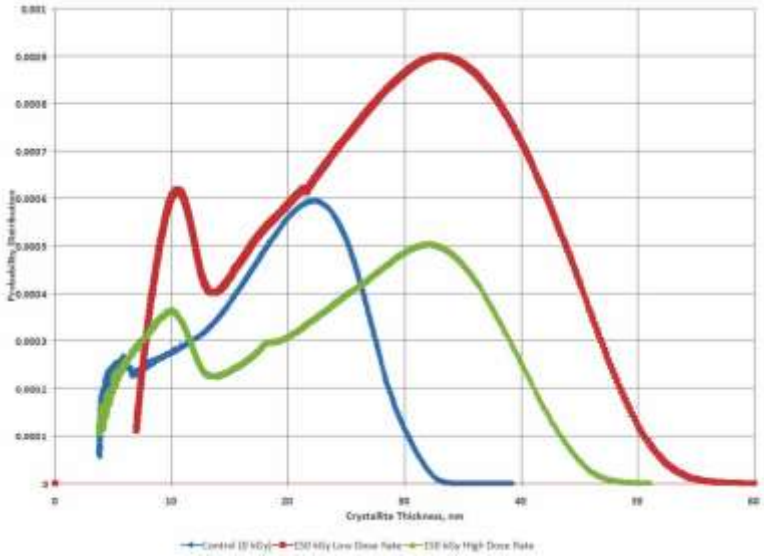

Figure 35: Effect of Dose Rate on the Surface of the 150 kGy Gamma Irradiated Crystallite Thickness Distribution

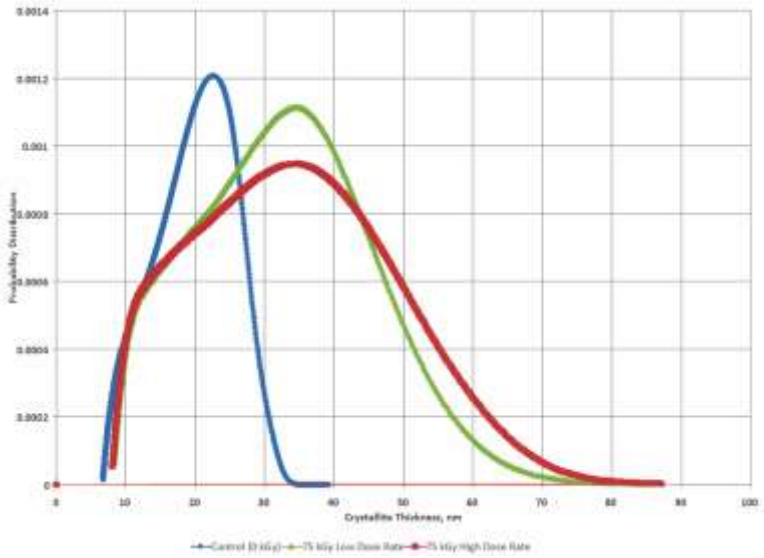

Figure 36: Effect of Dose Rate on the Center of the 75 kGy Gamma Irradiated Crystallite Thickness Distribution

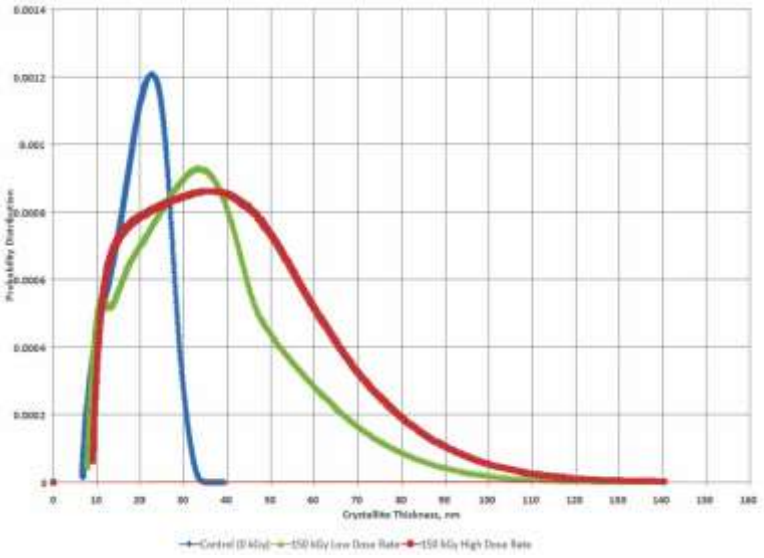

Figure 37: Effect of Dose Rate on the Center of the 150 kGy Gamma Irradiated Crystallite Thickness Distribution

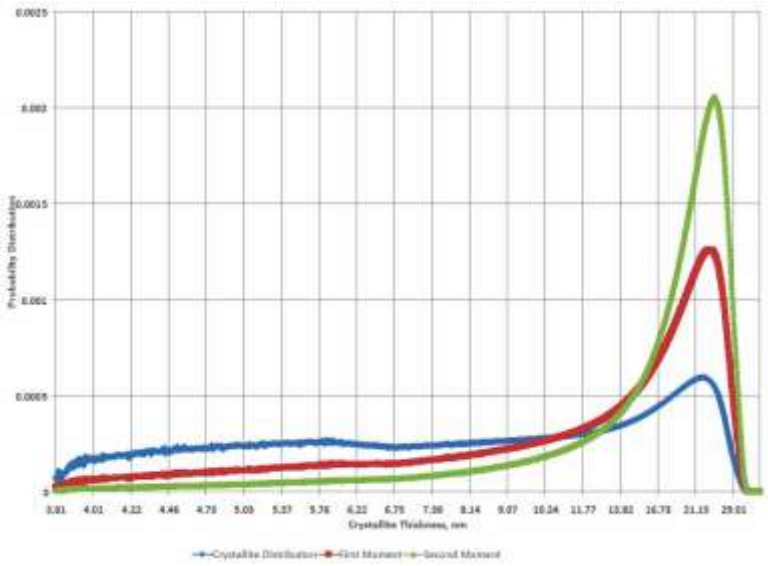

Figure 38: Surface of Control (0 kGy) Gamma Irradiated Sample (1801)

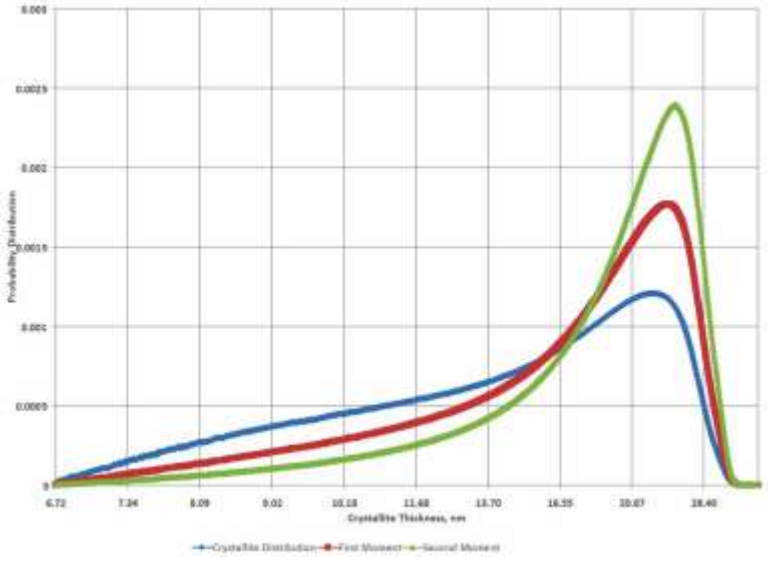

Figure 39: Center of Control (0 kGy) Gamma Irradiated Sample (1803)

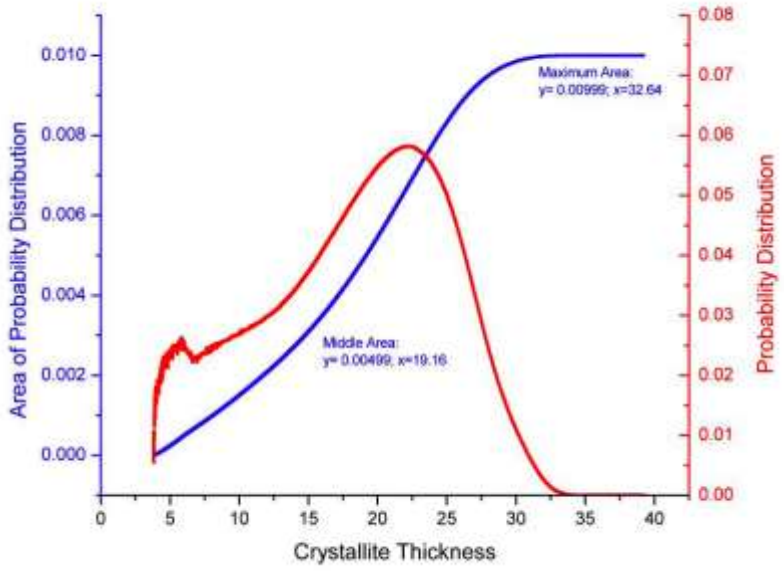

Figure 40: Control (0 kGy) Gamma Irradiated Crystallite Thickness Distribution for the Surface (Area Calculations)

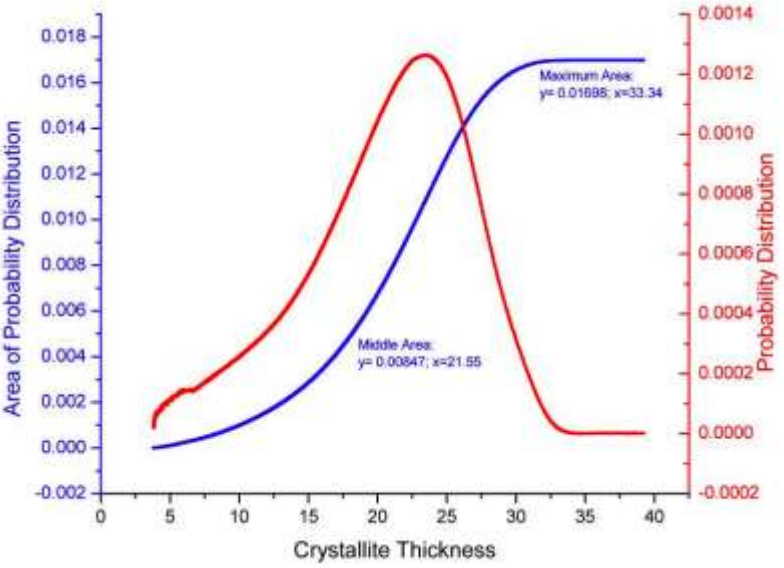

Figure 41: First Moment of Control (0 kGy) Gamma Irradiated Crystallite Thickness Distribution for the Surface (Area Calculations)

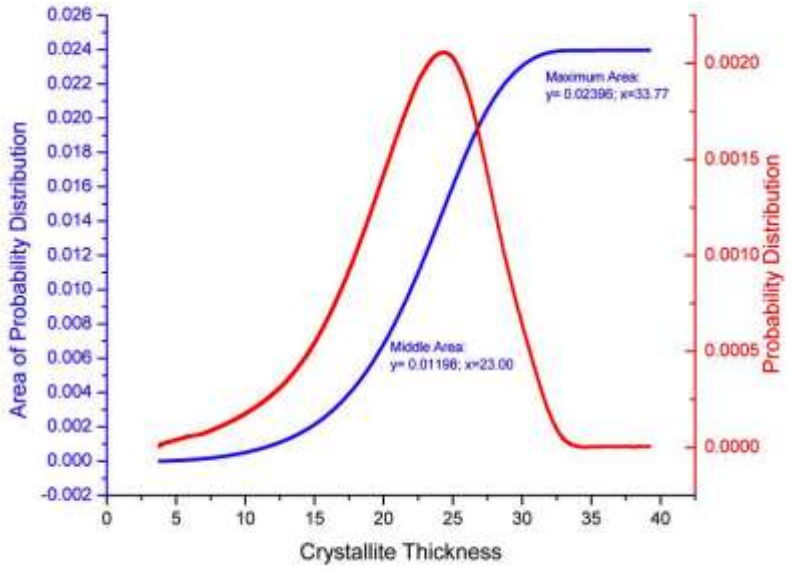

Figure 42: Second Moment of Control (0 kGy) Gamma Irradiated Crystallite Thickness Distribution for the Surface (Area Calculations)

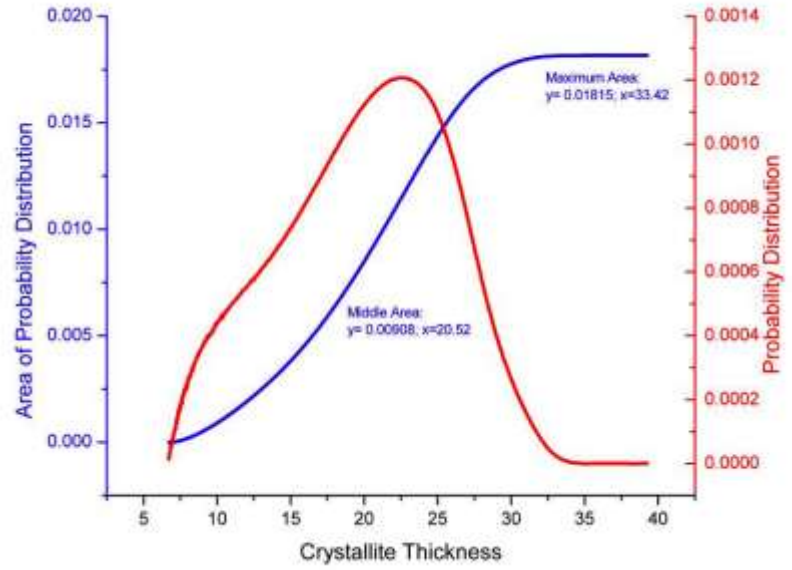

Figure 43: Control (0 kGy) Gamma Irradiated Crystallite Thickness Distribution for the Center (Area Calculations)

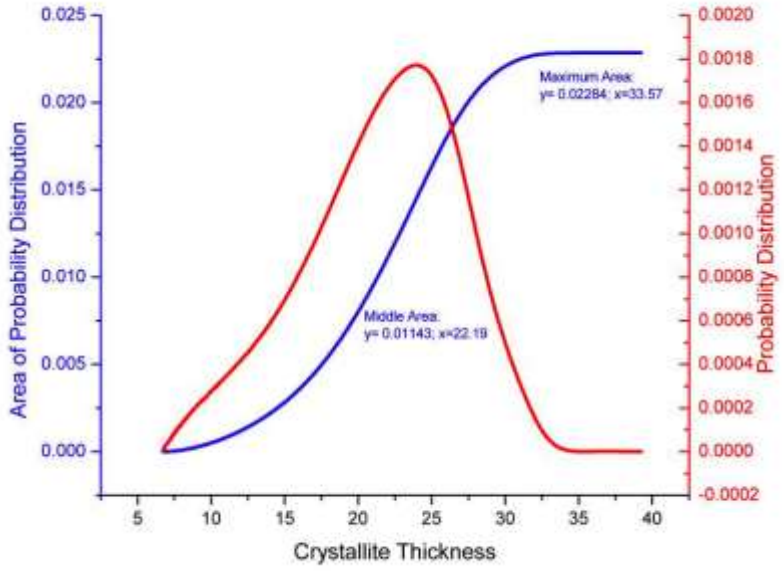

Figure 44: First Moment of Control (0 kGy) Gamma Irradiated Crystallite Thickness Distribution for the Center (Area Calculations)

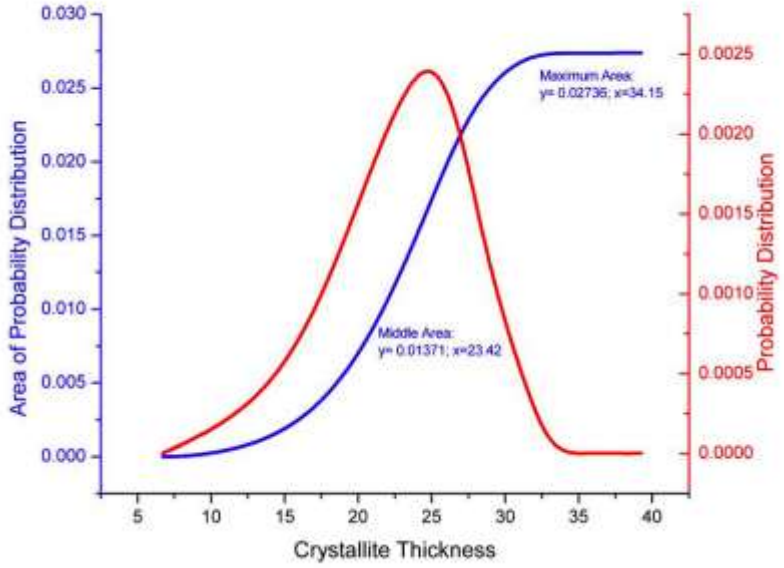

Figure 45: Second Moment of Control (0 kGy) Gamma Irradiated Crystallite Thickness Distribution for the Center (Area Calculations)

1.2.1 High Dose Rate

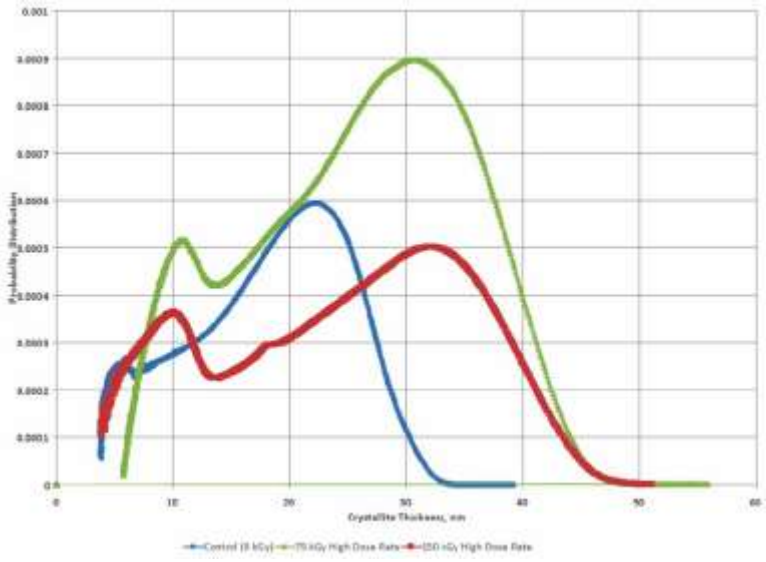

Figure 46: Effect of Integral Dose on the Surface of the Crystallite Thickness Distribution (High Dose Rate)

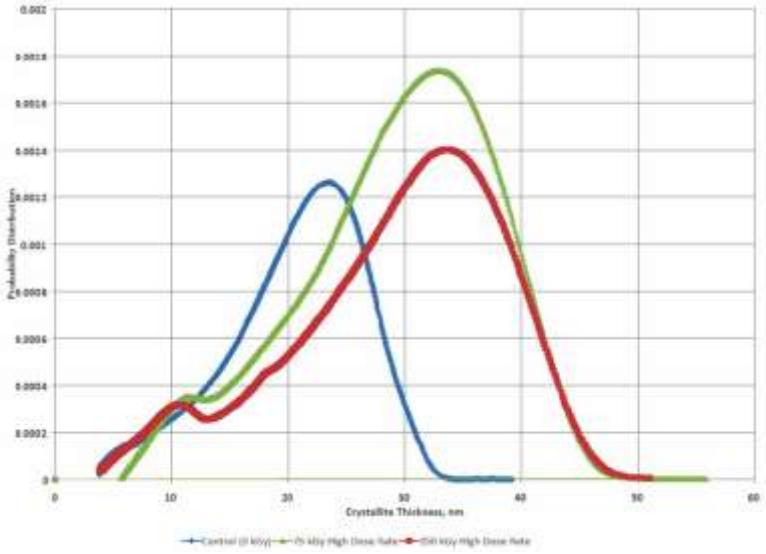

Figure 47: Effect of Integral Dose on the Surface of the First Moment of Crystallite Thickness Distribution (High Dose Rate)

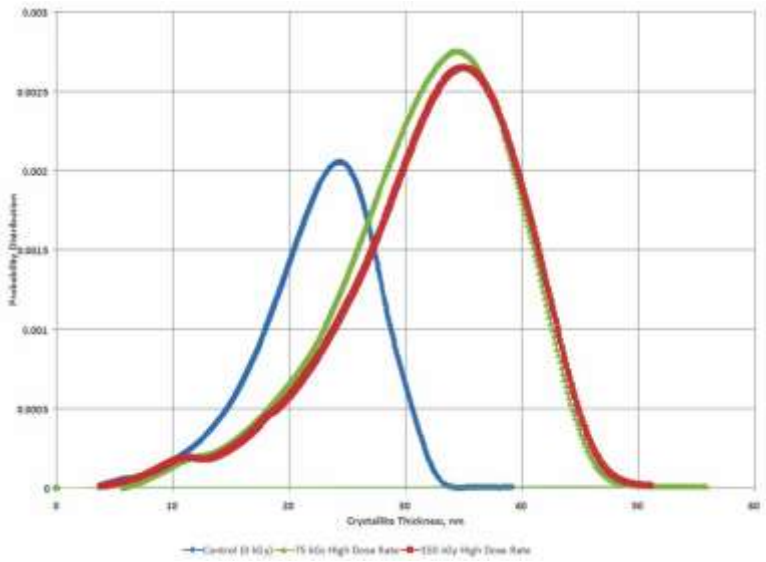

Figure 48: Effect of Integral Dose on the Surface of the Second Moment of Crystallite Thickness Distribution (High Dose Rate)

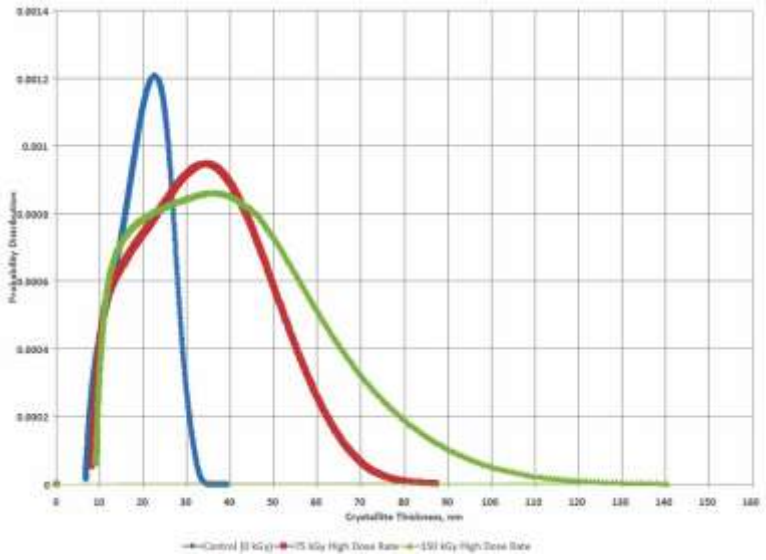

Figure 49: Effect of Integral Dose on the Center of the Crystallite Thickness Distribution (High Dose Rate)

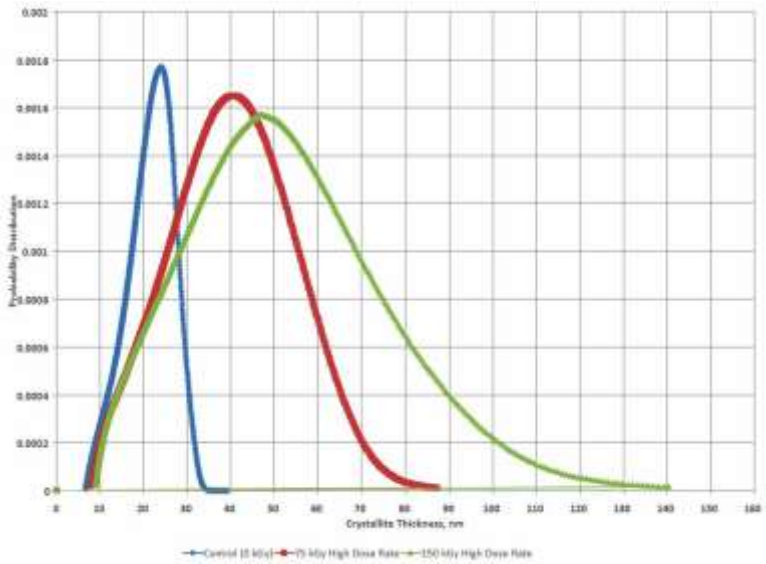

Figure 50: Effect of Integral Dose on the Center of the First Moment of Crystallite Thickness Distribution (High Dose Rate)

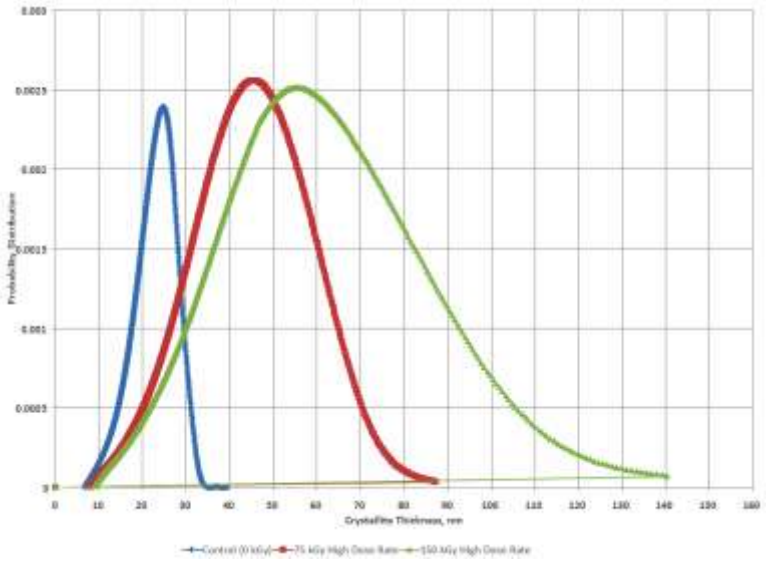

Figure 51: Effect of Integral Dose on the Center of the Second Moment of Crystallite Thickness Distribution (High Dose Rate)

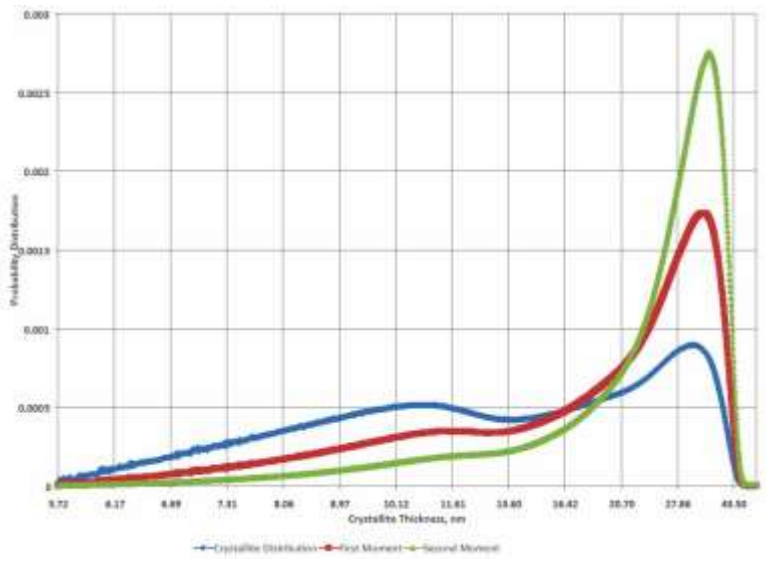

Figure 52: Surface of 75 kGy High Dose Rate Gamma Irradiated Sample (3701)

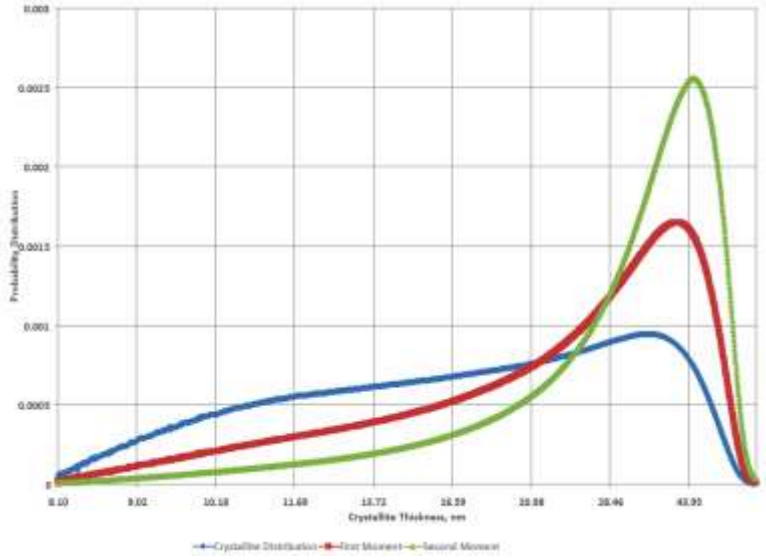

Figure 53: Center of 75 kGy High Dose Rate Gamma Irradiated Sample (3703)

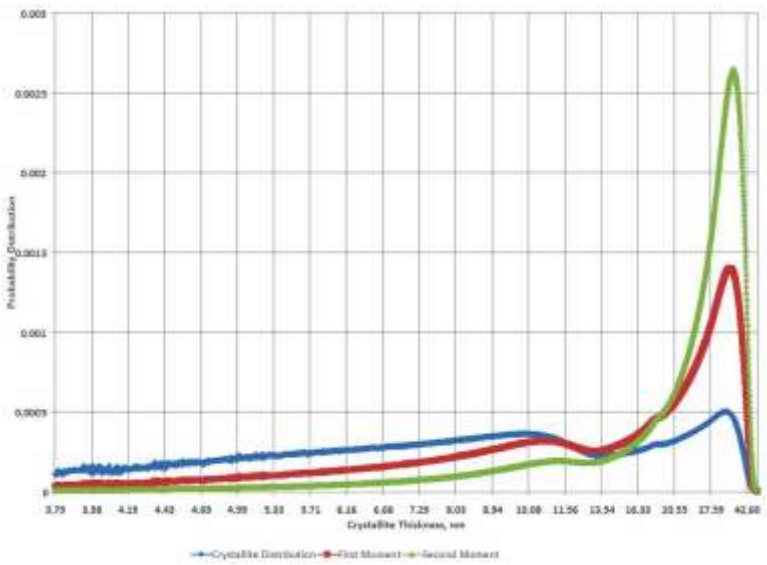

Figure 54: Surface of 150 kGy High Dose Rate Gamma Irradiated Sample (4501)

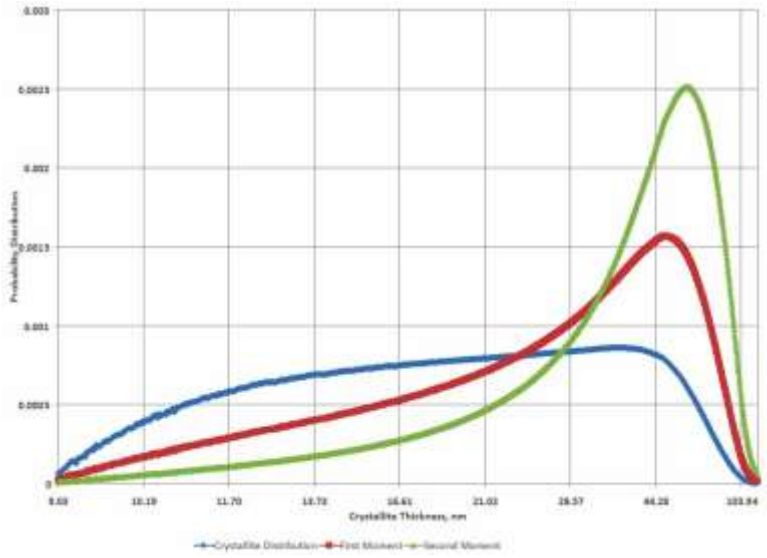

Figure 55: Center of 150 kGy High Dose Rate Gamma Irradiated Sample (4503)

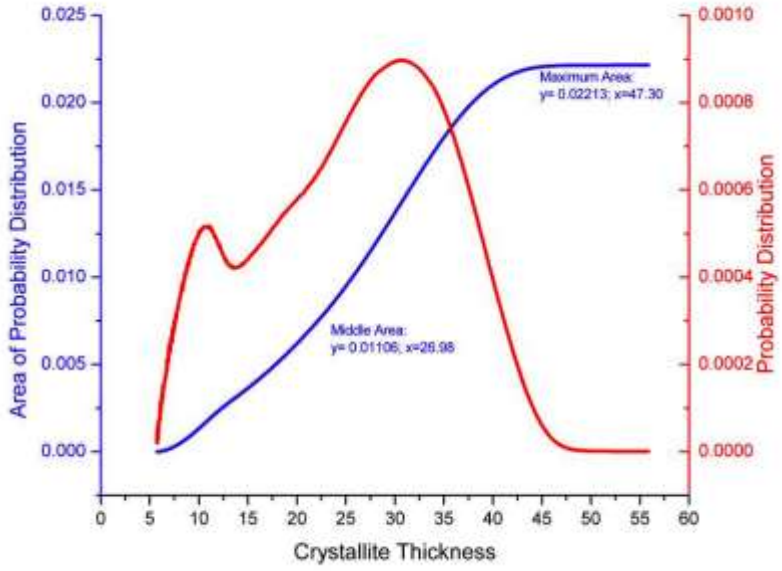

Figure 56: 75 kGy, High Dose Rate, Gamma Irradiated Crystallite Thickness Distribution for the Surface (Area Calculations)

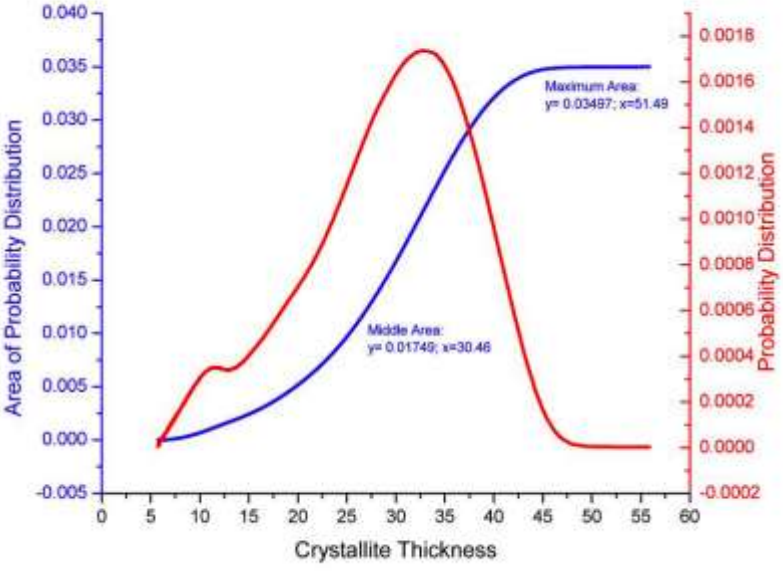

Figure 57: First Moment of 75 kGy, High Dose Rate, Gamma Irradiated Crystallite Thickness Distribution for the Surface (Area Calculations)

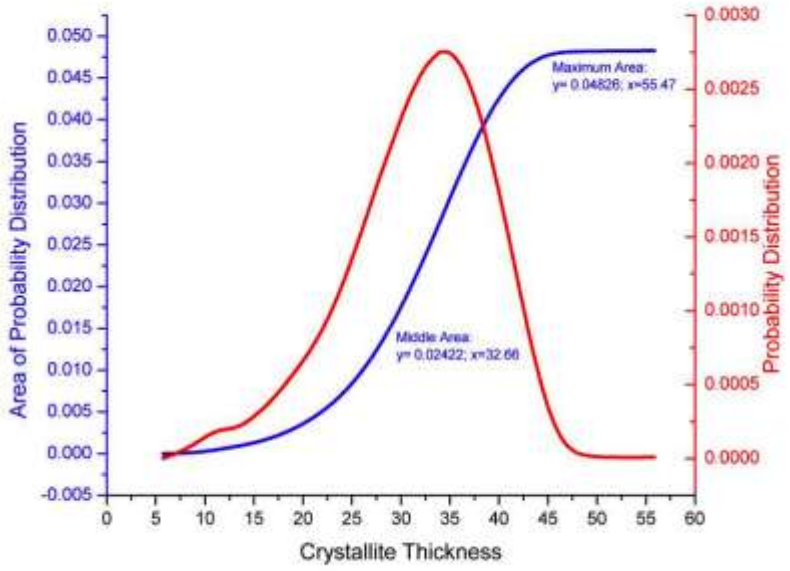

Figure 58: Second Moment of 75 kGy, High Dose Rate, Gamma Irradiated Crystallite Thickness Distribution for the Surface (Area Calculations)

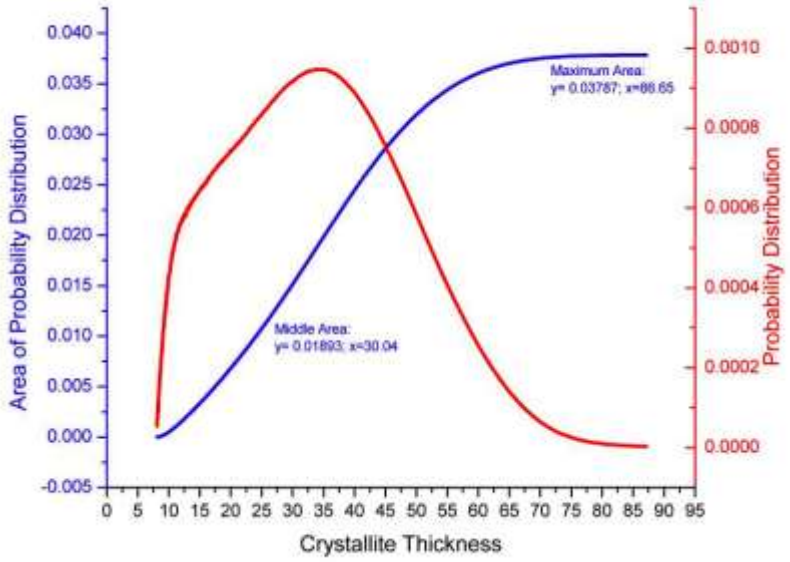

Figure 59: 75 kGy, High Dose Rate, Gamma Irradiated Crystallite Thickness Distribution for the Center (Area Calculations)

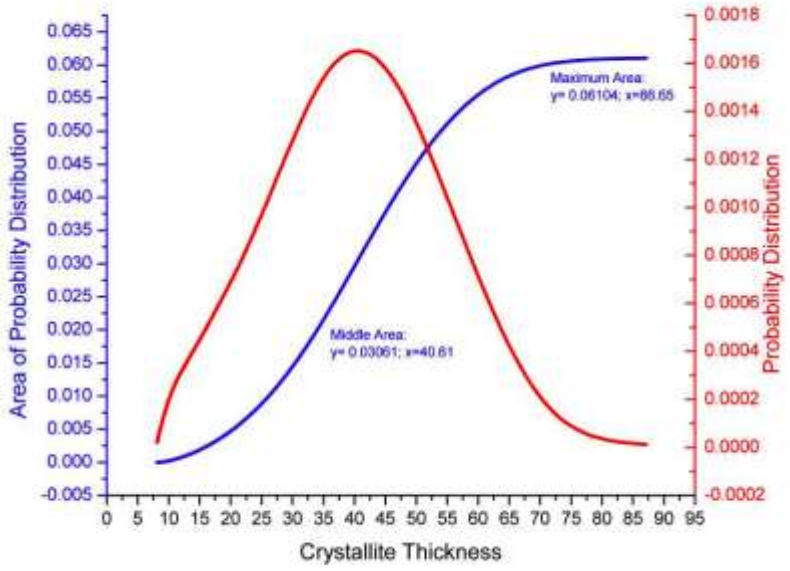

Figure 60: First Moment of 75 kGy, High Dose Rate, Gamma Irradiated Crystallite Thickness Distribution for the Center (Area Calculations)

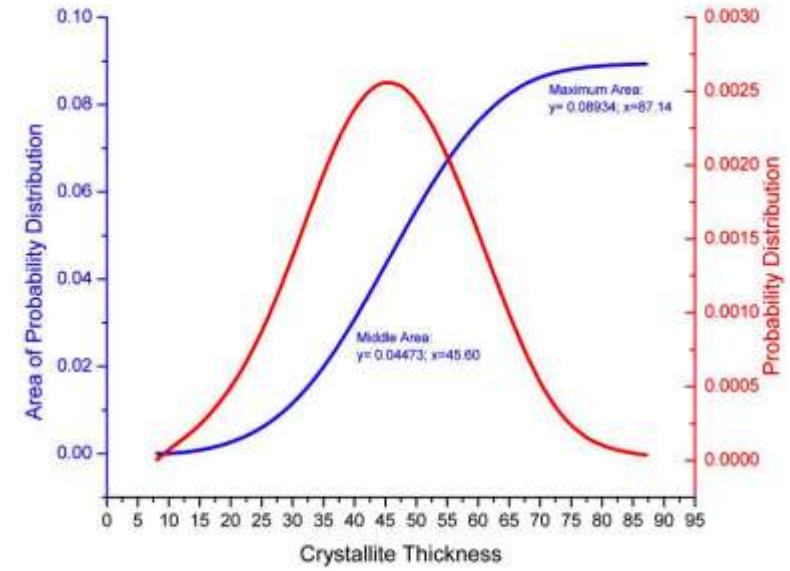

Figure 61: Second Moment of 75 kGy, High Dose Rate, Gamma Irradiated Crystallite Thickness Distribution for the Center (Area Calculations)

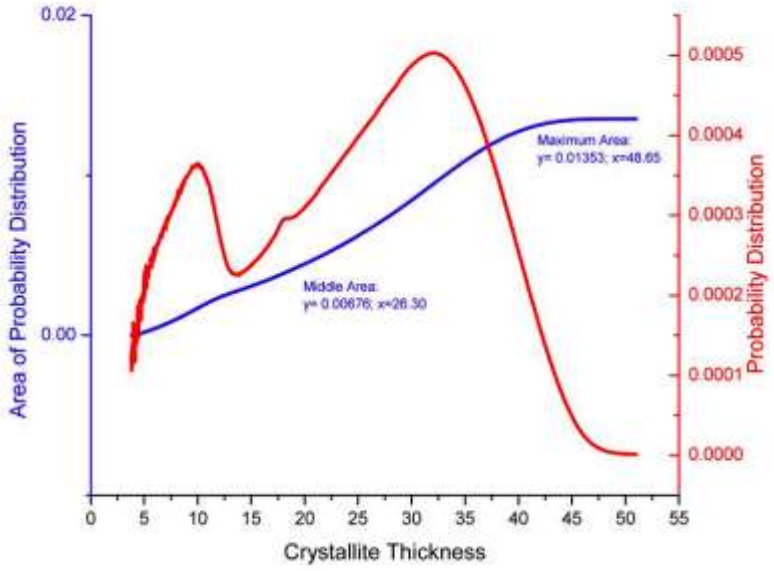

Figure 62: 150 kGy, High Dose Rate, Gamma Irradiated Crystallite Thickness Distribution for the Surface (Area Calculations)

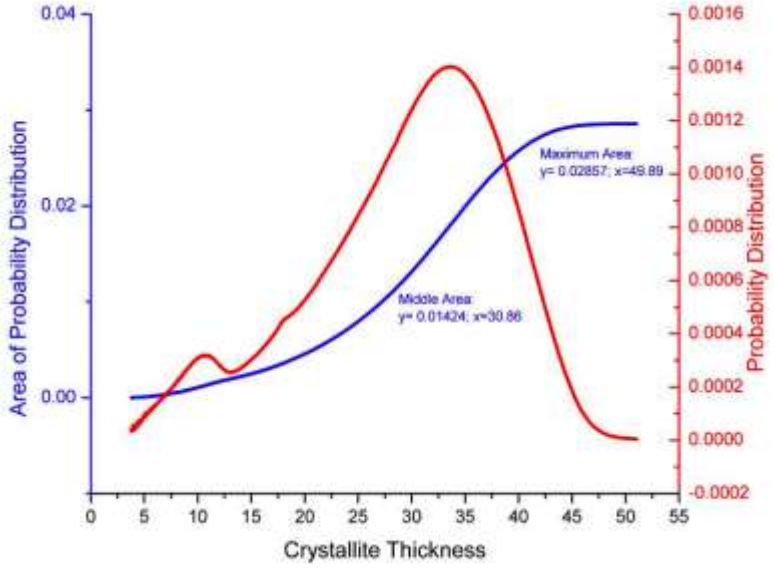

Figure 63: First Moment of 150 kGy, High Dose Rate, Gamma Irradiated Crystallite Thickness Distribution for the Surface (Area Calculations)

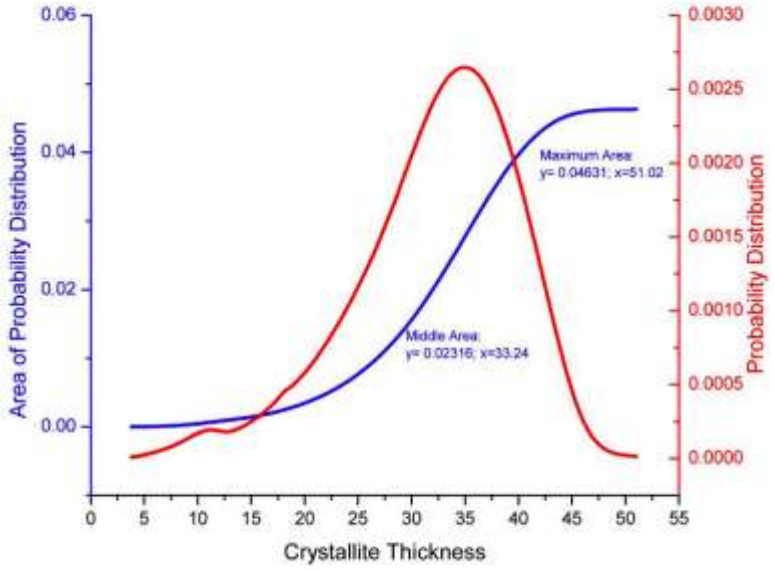

Figure 64: Second Moment of 150 kGy, High Dose Rate, Gamma Irradiated Crystallite Thickness Distribution for the Surface (Area Calculations)

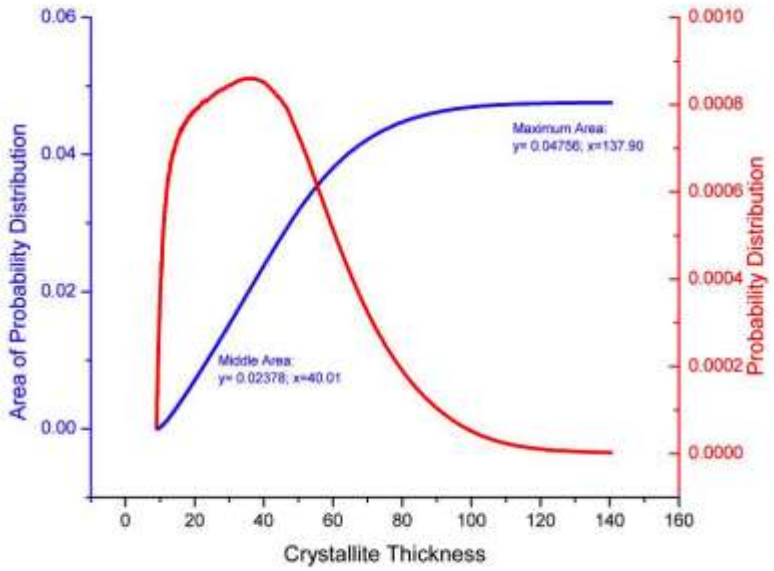

Figure 65: 150 kGy, High Dose Rate, Gamma Irradiated Crystallite Thickness Distribution for the Center (Area Calculations)

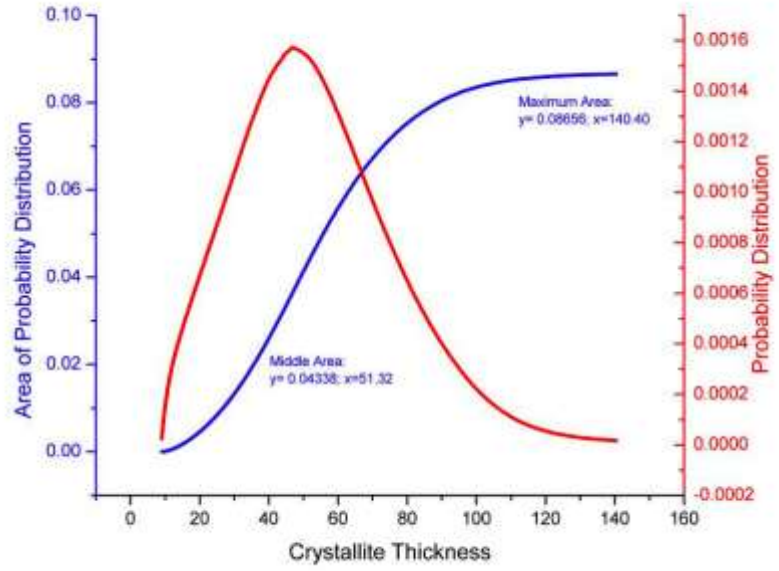

Figure 66: First Moment of 150 kGy, High Dose Rate, Gamma Irradiated Crystallite Thickness Distribution for the Center (Area Calculations)

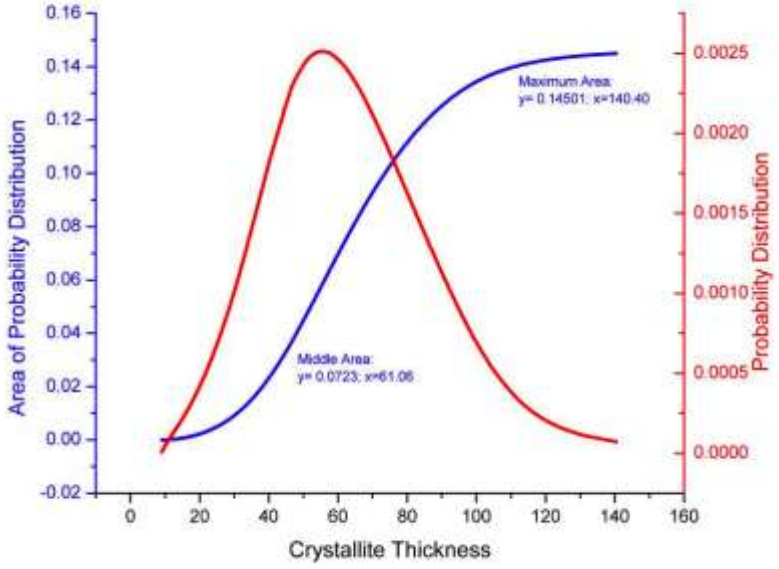

Figure 67: Second Moment of 150 kGy, High Dose Rate, Gamma Irradiated Crystallite Thickness Distribution for the Center (Area Calculations)

1.2.2 Low Dose Rate

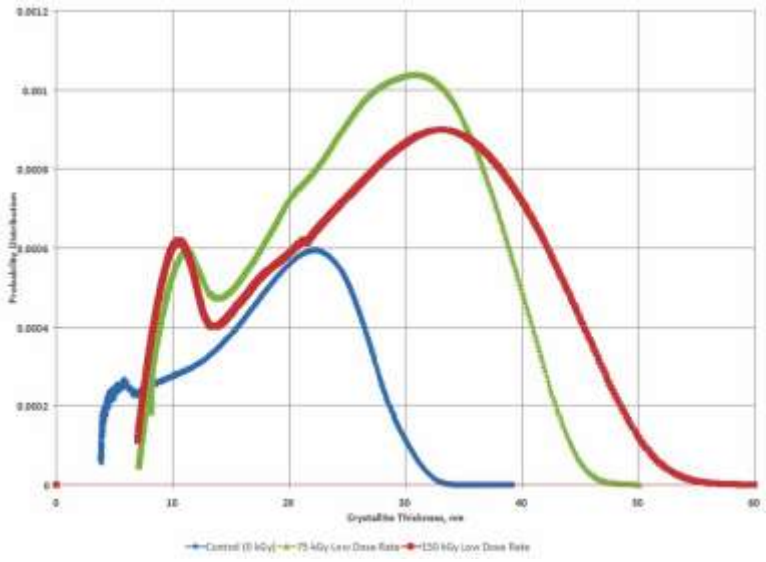

Figure 68: Effect of Integral Dose on the Surface of the Crystallite Thickness Distribution (Low Dose Rate)

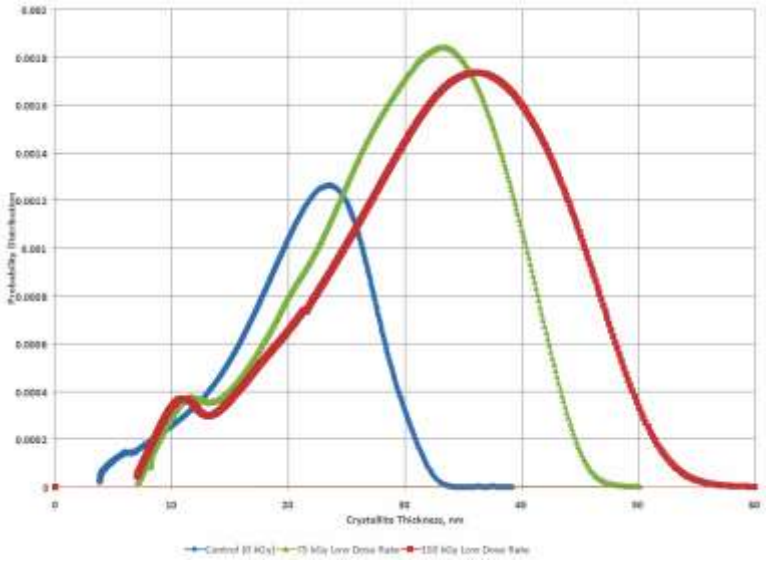

Figure 69: Effect of Integral Dose on the Surface of the First Moment of Crystallite Thickness Distribution (Low Dose Rate)

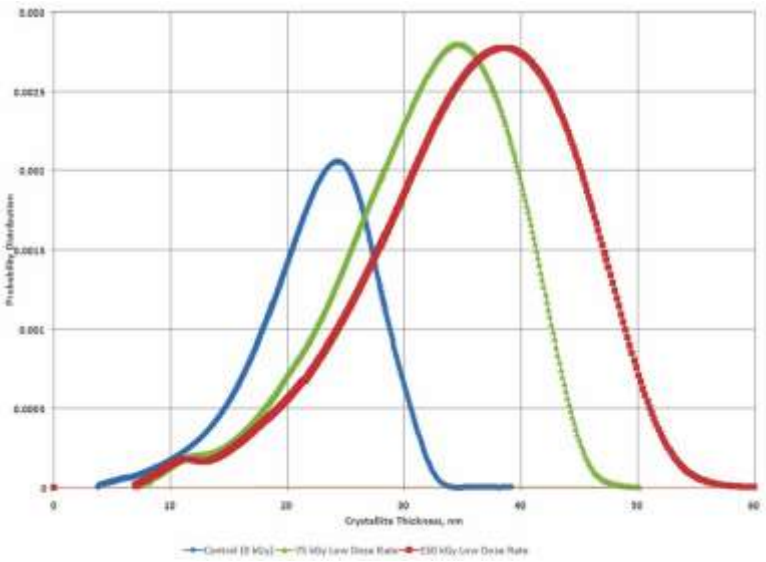

Figure 70: Effect of Integral Dose on the Surface of the Second Moment of Crystallite Thickness Distribution (Low Dose Rate)

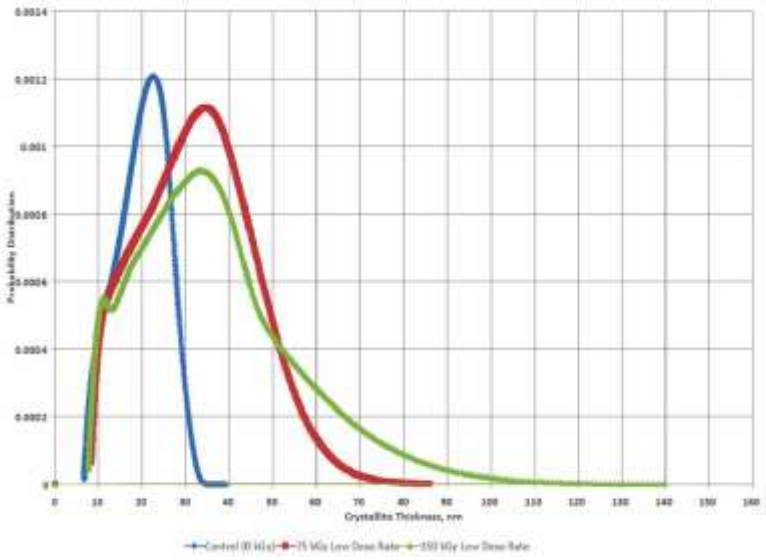

Figure 71: Effect of Integral Dose on the Center of the Crystallite Thickness Distribution (Low Dose Rate)

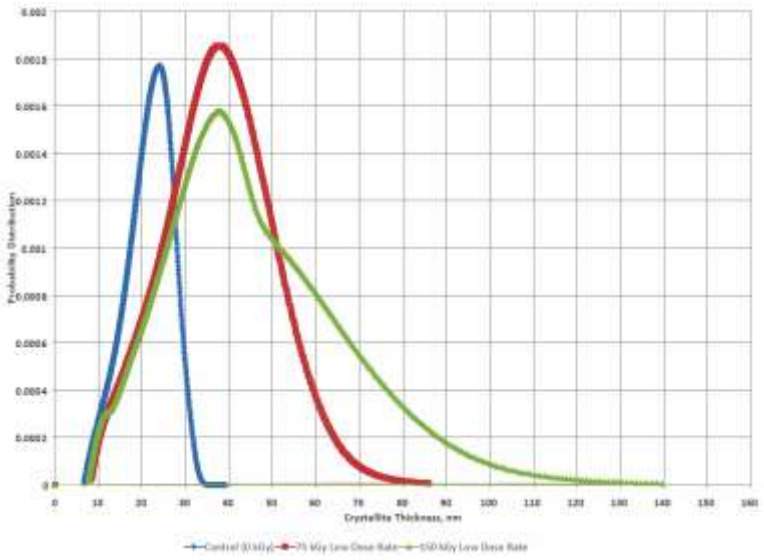

Figure 72: Effect of Integral Dose on the Center of the First Moment of Crystallite Thickness Distribution (Low Dose Rate)

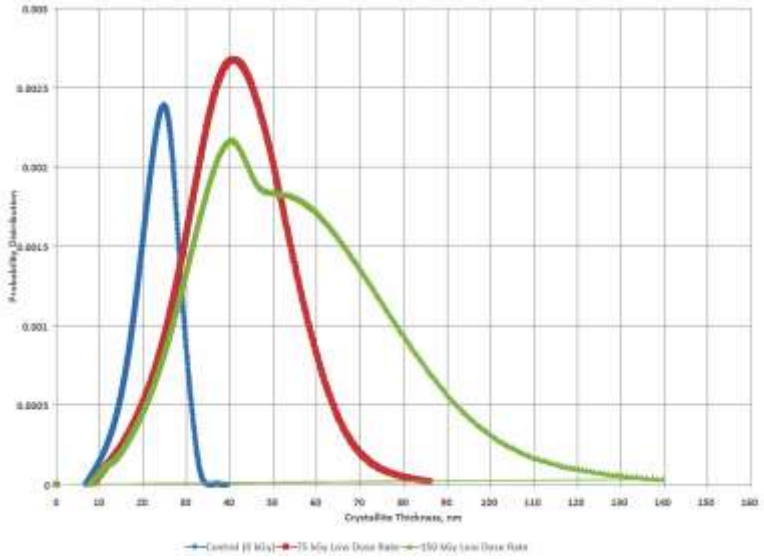

Figure 73: Effect of Integral Dose on the center of the Second Moment of Crystallite Thickness Distribution (Low Dose Rate)

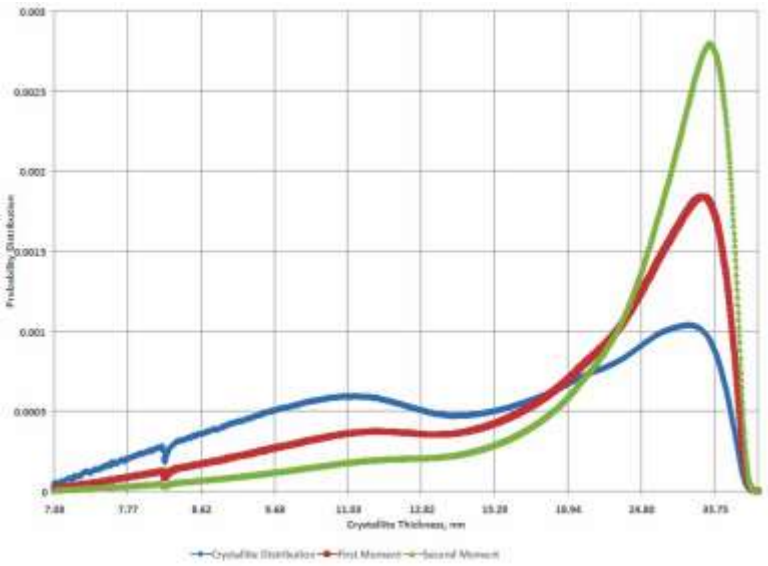

Figure 74: Surface of 75 kGy Low Dose Rate Gamma Irradiated Sample (4701)

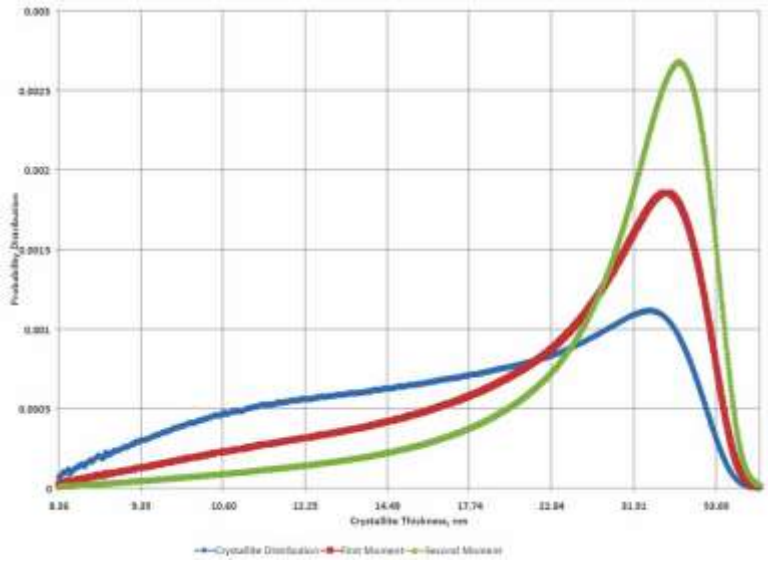

Figure 75: Center of 75 kGy Low Dose Rate Gamma Irradiated Sample (4703)

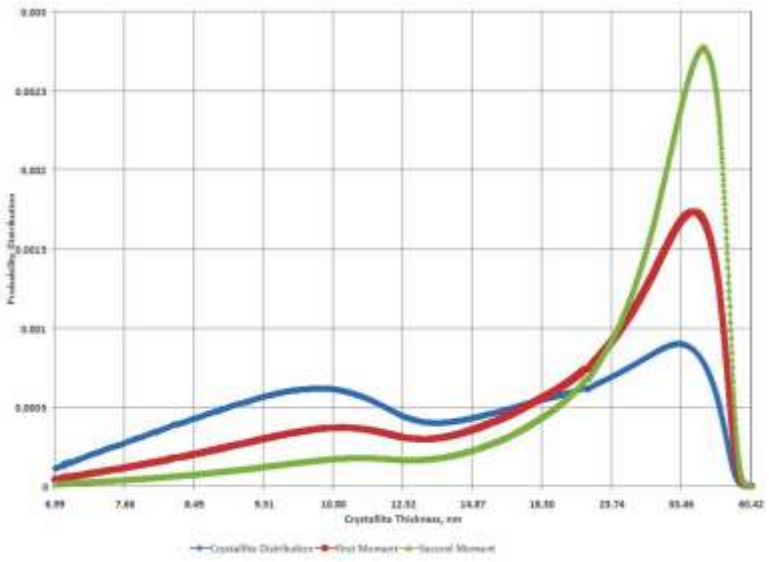

Figure 76: Surface of 150 kGy Low Dose Rate Gamma Irradiated Sample (5301)

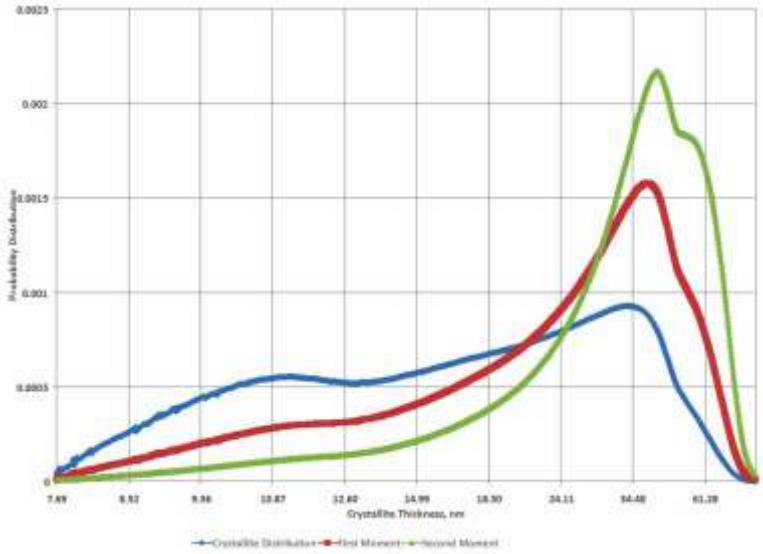

Figure 77: Center of 150 kGy Low Dose Rate Gamma Irradiated Sample (5303)

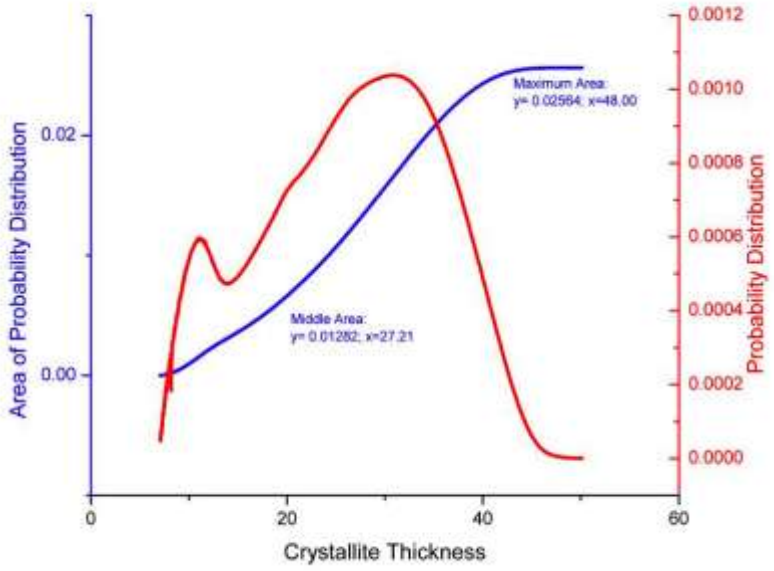

Figure 78: 75 kGy, Low Dose Rate, Gamma Irradiated Crystallite Thickness Distribution for the Surface (Area Calculations)

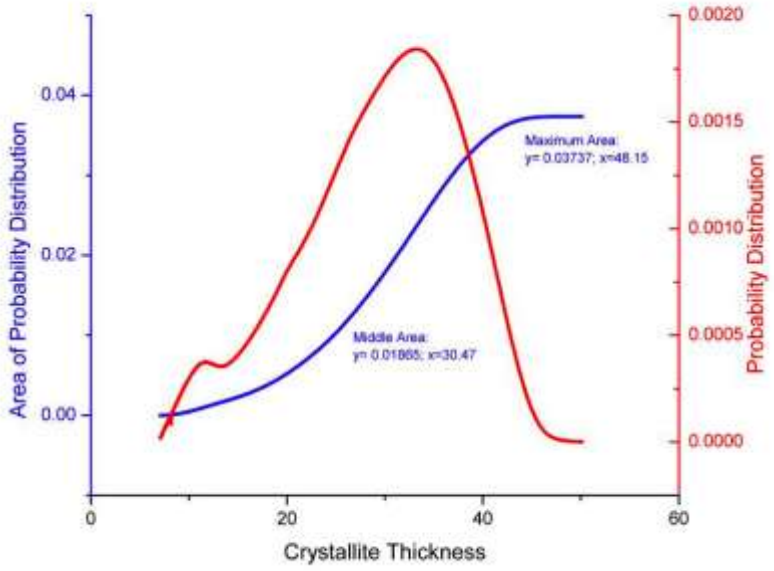

Figure 79: First Moment of 75 kGy, Low Dose Rate, Gamma Irradiated Crystallite Thickness Distribution for the Surface (Area Calculations)

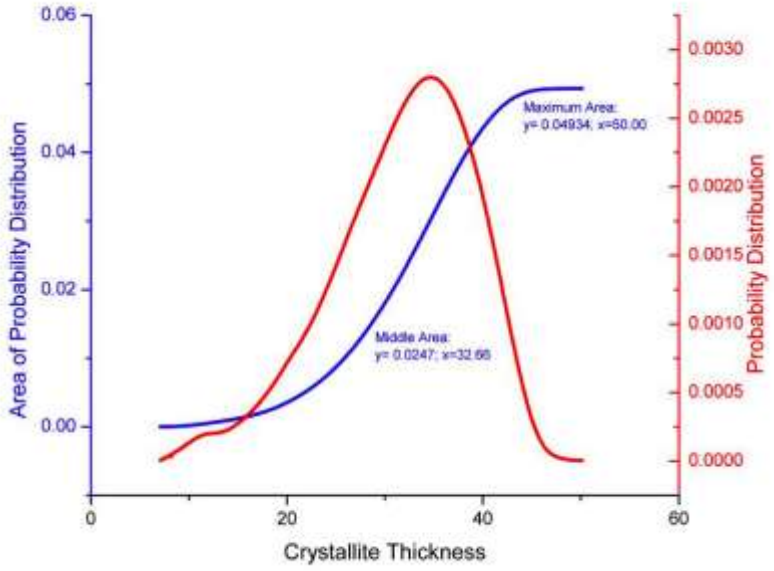

Figure 80: Second Moment of 75 kGy, Low Dose Rate, Gamma Irradiated Crystallite Thickness Distribution for the Surface (Area Calculations)

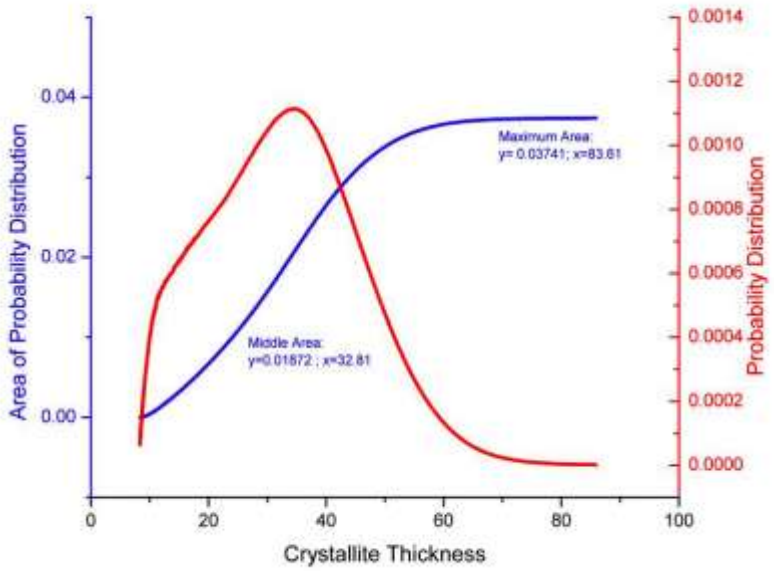

Figure 81: 75 kGy, Low Dose Rate, Gamma Irradiated Crystallite Thickness Distribution for the Center (Area Calculations)

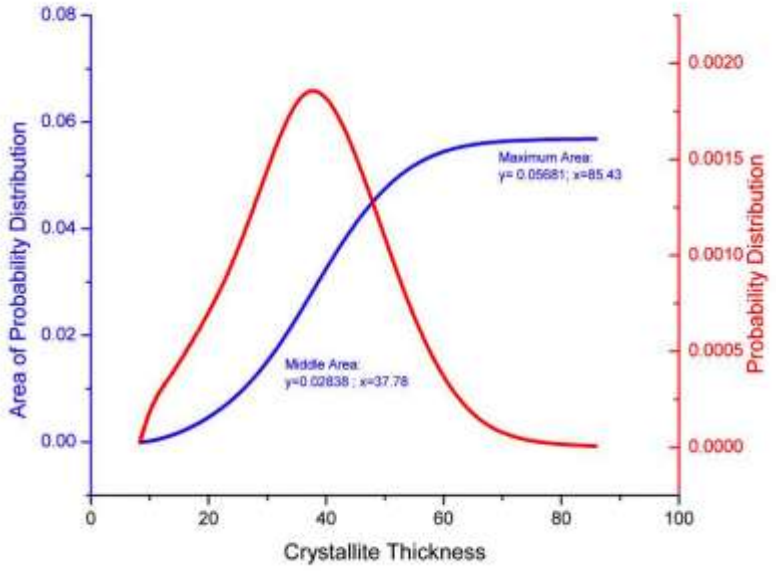

Figure 82: First Moment of 75 kGy, Low Dose Rate, Gamma Irradiated Crystallite Thickness Distribution for the Center (Area Calculations)

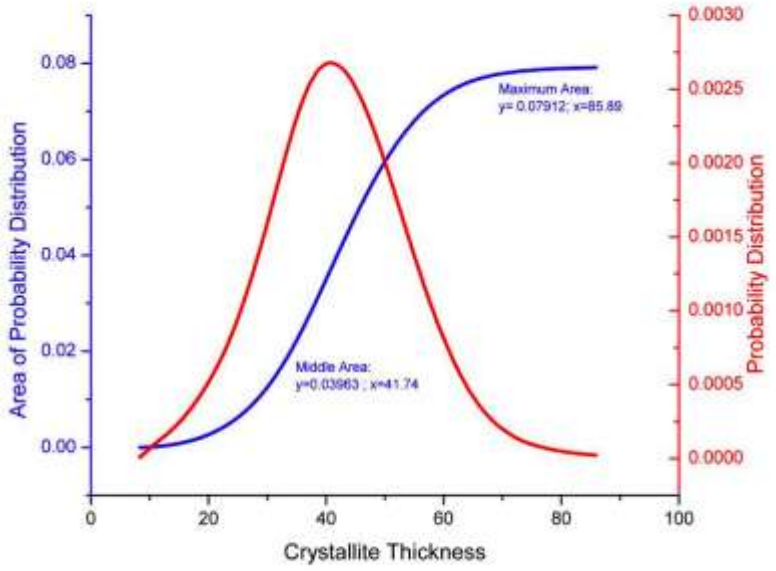

Figure 83: Second Moment of 75 kGy, Low Dose Rate, Gamma Irradiated Crystallite Thickness Distribution for the Center (Area Calculations)

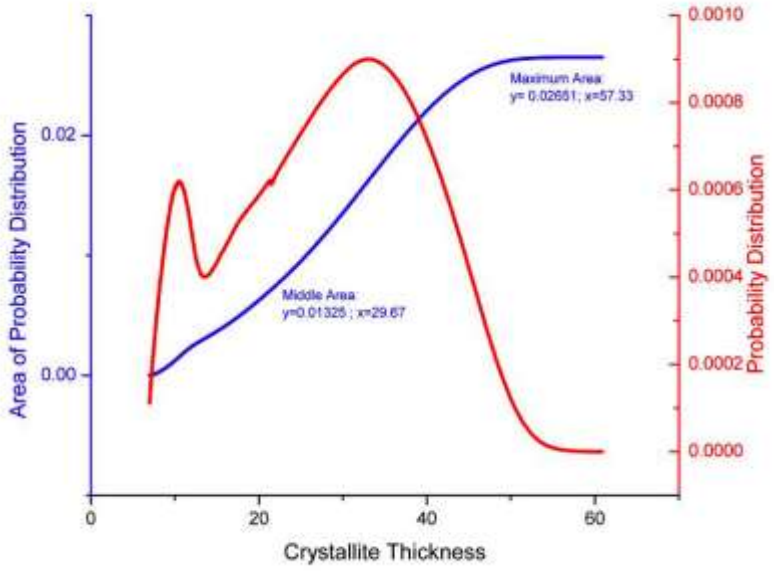

Figure 84: 150 kGy, Low Dose Rate, Gamma Irradiated Crystallite Thickness Distribution for the Surface (Area Calculations)

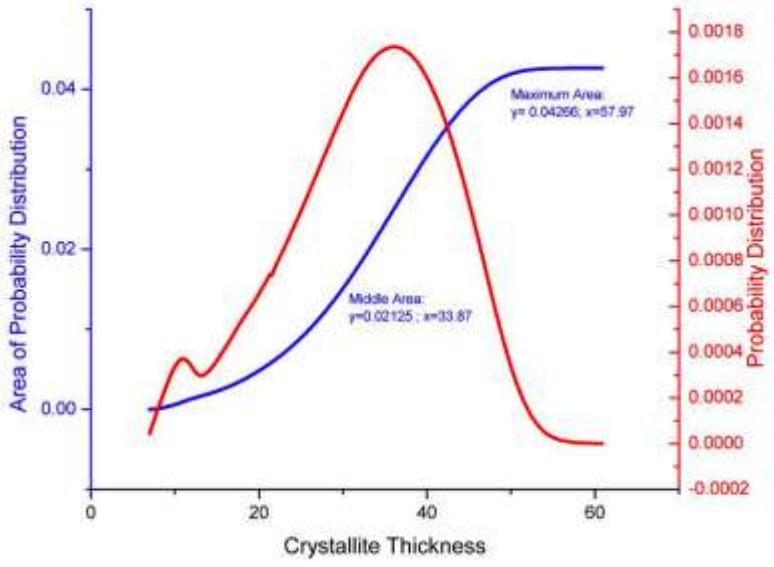

Figure 85: First Moment of 150 kGy, Low Dose Rate, Gamma Irradiated Crystallite Thickness Distribution for the Surface (Area Calculations)

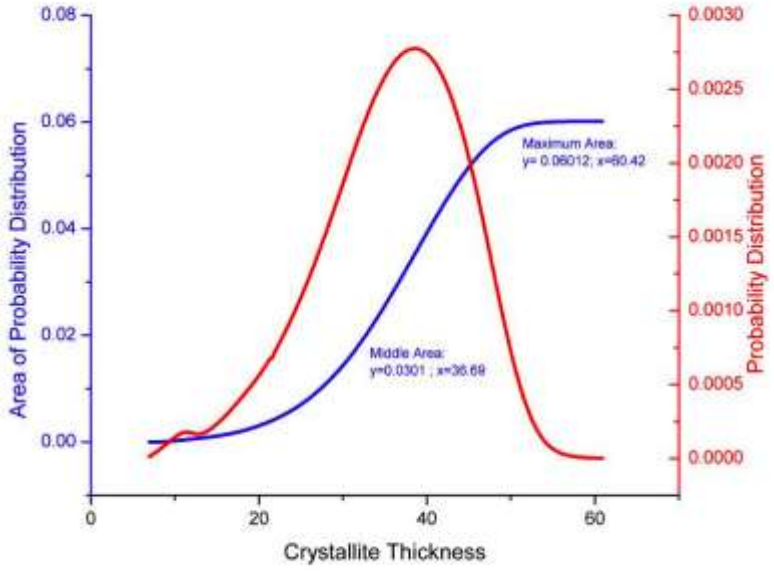

Figure 86: Second Moment of 150 kGy, Low Dose Rate, Gamma Irradiated Crystallite Thickness Distribution for the Surface (Area Calculations)

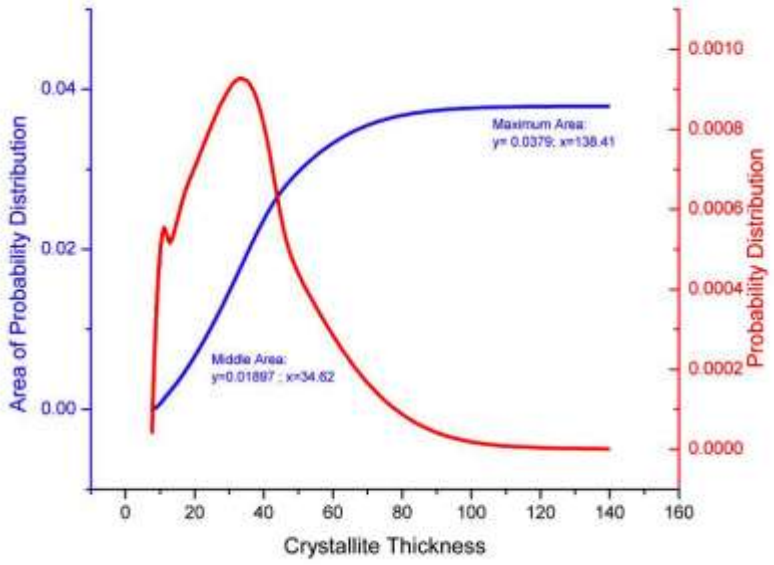

Figure 87: 150 kGy, Low Dose Rate, Gamma Irradiated Crystallite Thickness Distribution for the Center (Area Calculations)

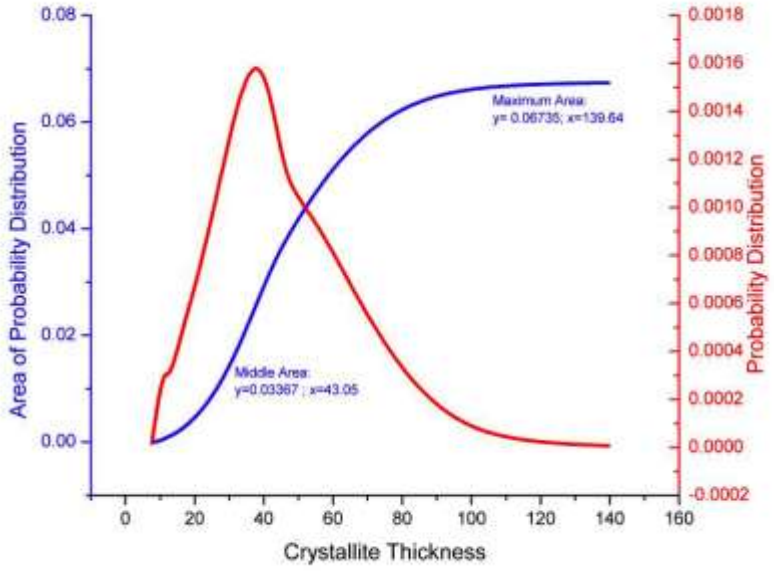

Figure 88: First Moment of 150 kGy, Low Dose Rate, Gamma Irradiated Crystallite Thickness Distribution for the Center (Area Calculations)

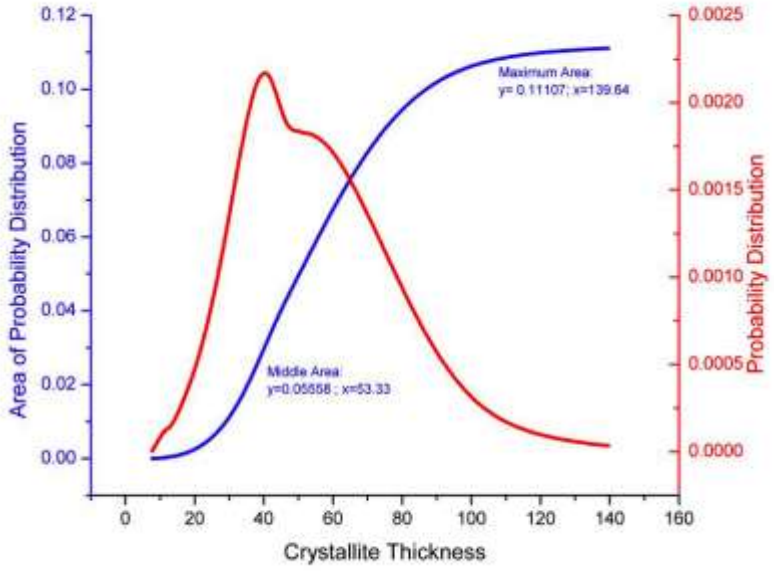

Figure 89: Second Moment of 150 kGy, Low Dose Rate, Gamma Irradiated Crystallite Thickness Distribution for the Center (Area Calculations)

2 Appendix II: Proton Irradiation Study

2.1 Thermal Analysis

2.1.1 Thermal Analysis of Post-Irradiated Samples (Run 1)

Table 24: Effect of Radiation for Run 1 of Proton Irradiated Samples

Dose (kGy)	Crystalinity
0	60 ± 9%
1.77	58 ±3%
5.89	62 ± 5%

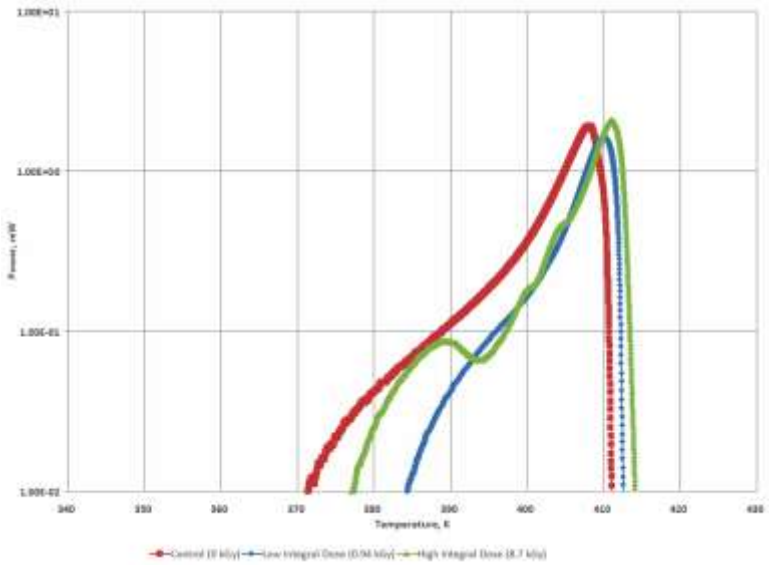

Figure 90: Endotherm for Run 1 of Proton Irradiated Samples

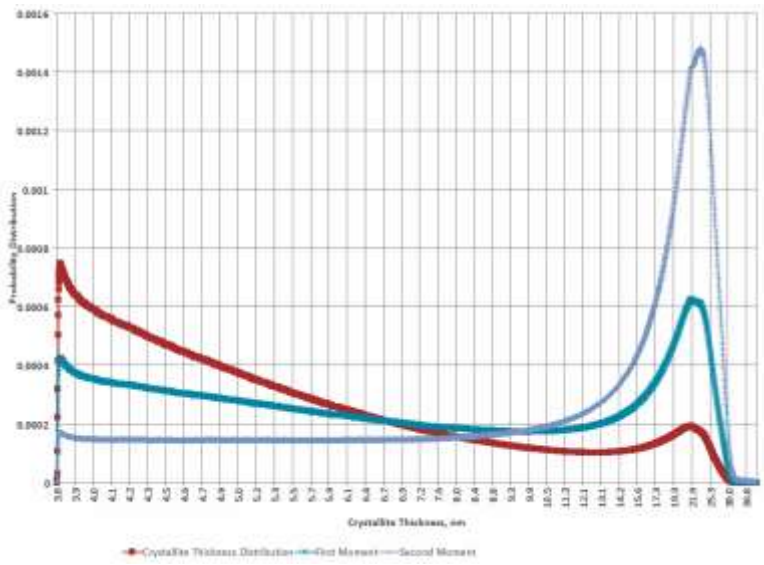

Figure 91: Run 1 of 0 kGy (Control) Proton Irradiated Sample (CPS04018B_1F)

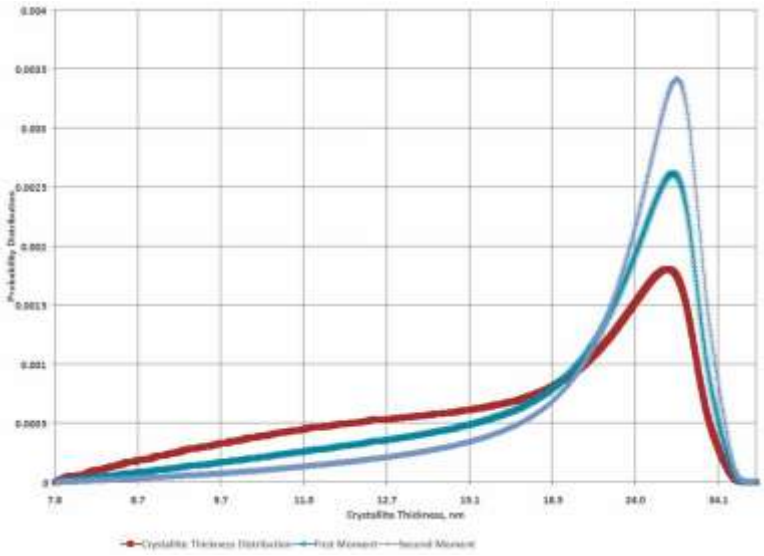

Figure 92: Run 1 of 0 kGy (Control) Proton Irradiated Sample (CPS04019C_1F)

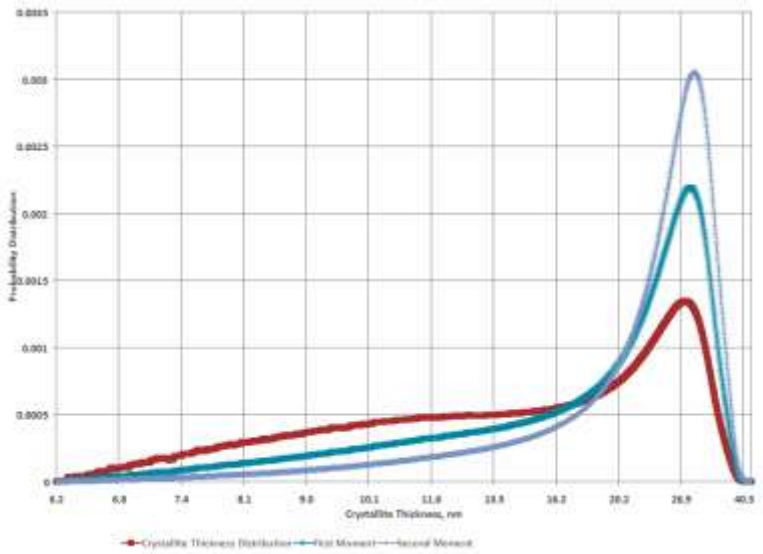

Figure 93: Run 1 of 0 kGy (Control) Proton Irradiated Sample (CPS04020C_1F)

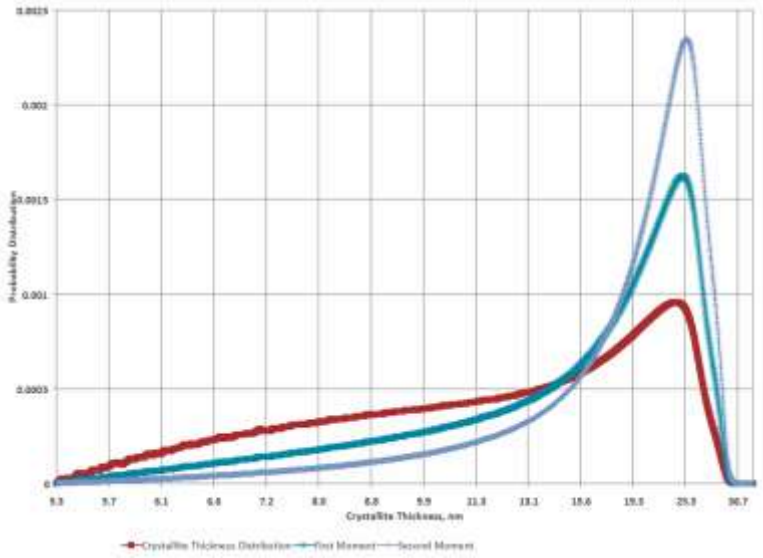

Figure 94: Run 1 of 0 kGy (Control) Proton Irradiated Sample (CPS04021A_1)

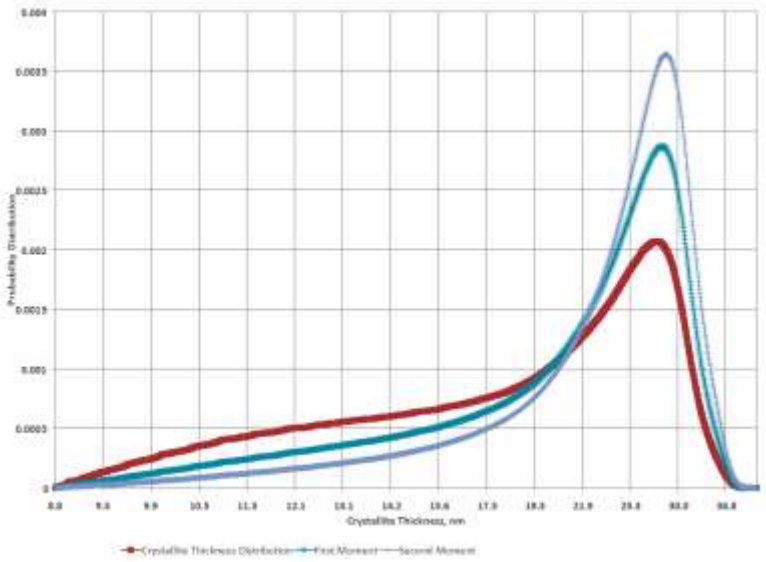

Figure 95: Run 1 of 0.96 kGy Proton Irradiated Sample (CPS04015A_1F)

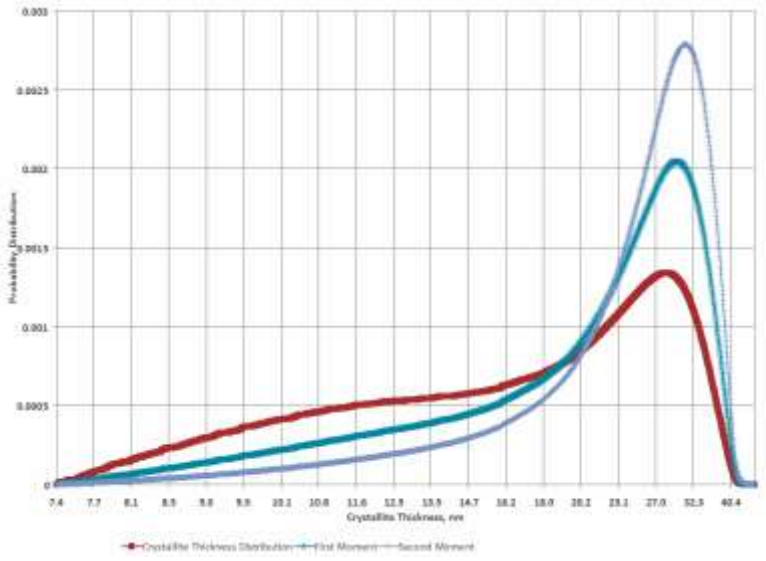

Figure 96: Run 1 of 0.94 kGy Proton Irradiated Sample (CPS04015C_1F)

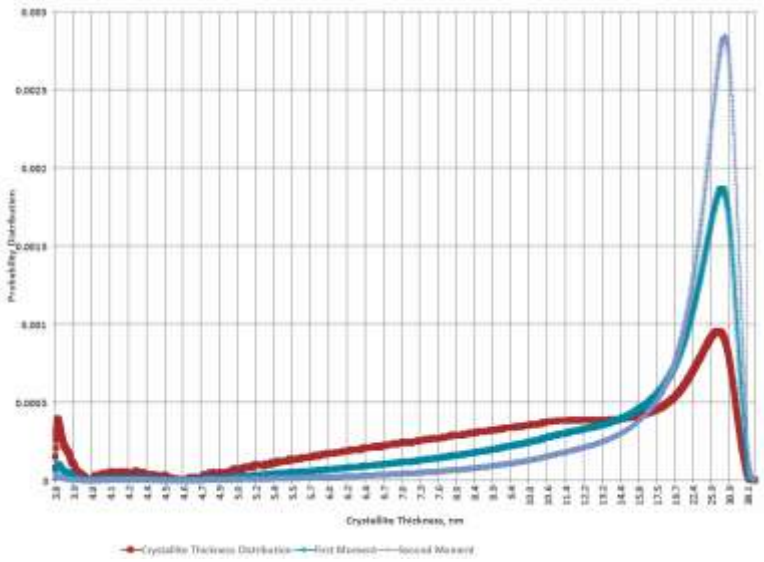

Figure 97: Run 1 of 1.08 kGy Proton Irradiated Sample (CPS04015B_1F)

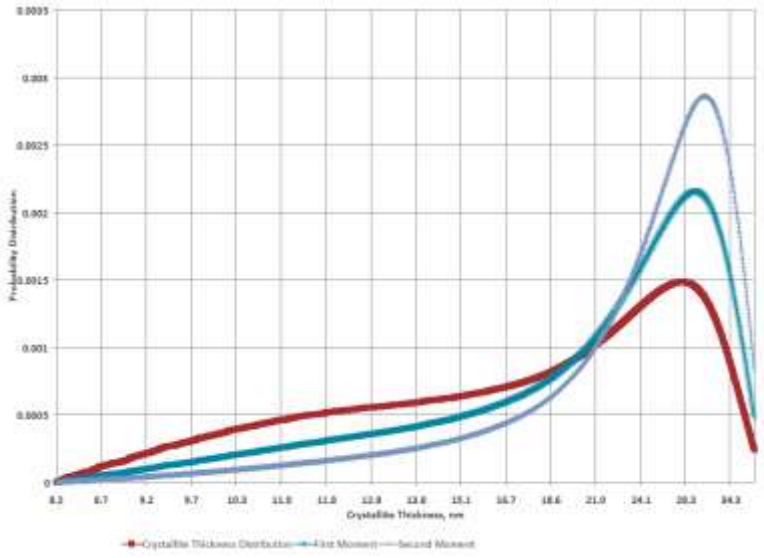

Figure 98: Run 1 of 1.15 kGy Proton Irradiated Sample (CPS04015D_1F)

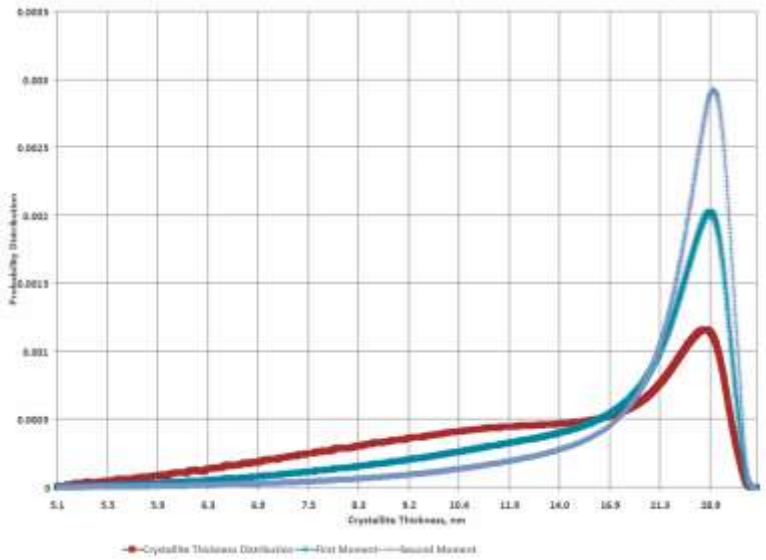

Figure 99: Run 1 of 1.33 kGy Proton Irradiated Sample (CPS04020B_1F)

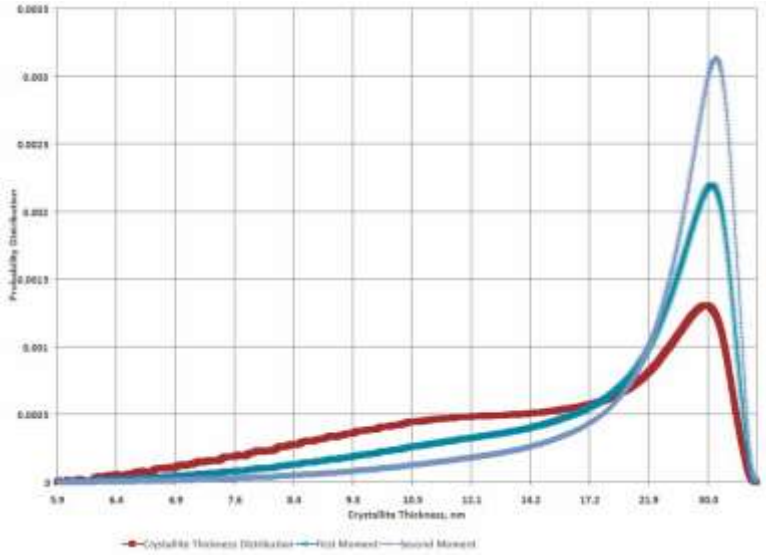

Figure 100: Run 1 of 3.7 kGy Proton Irradiated Sample (CPS04020A_1F)

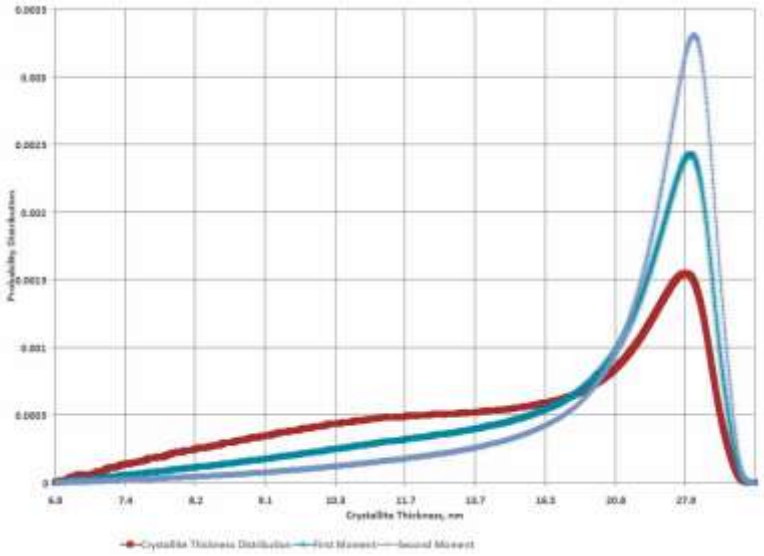

Figure 101: Run 1 of 3.7 kGy Proton Irradiated Sample (CPS04019A_1F)

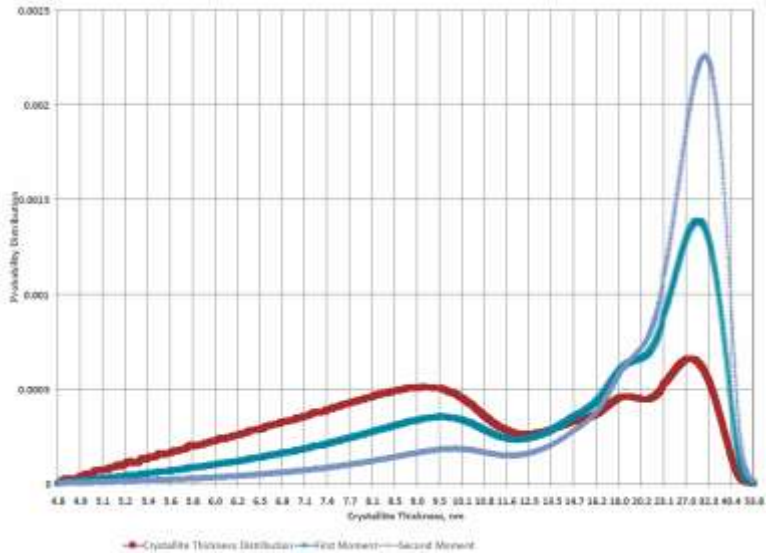

Figure 102: Run 1 of 6.8 kGy Proton Irradiated Sample (CPS04018C_1F)

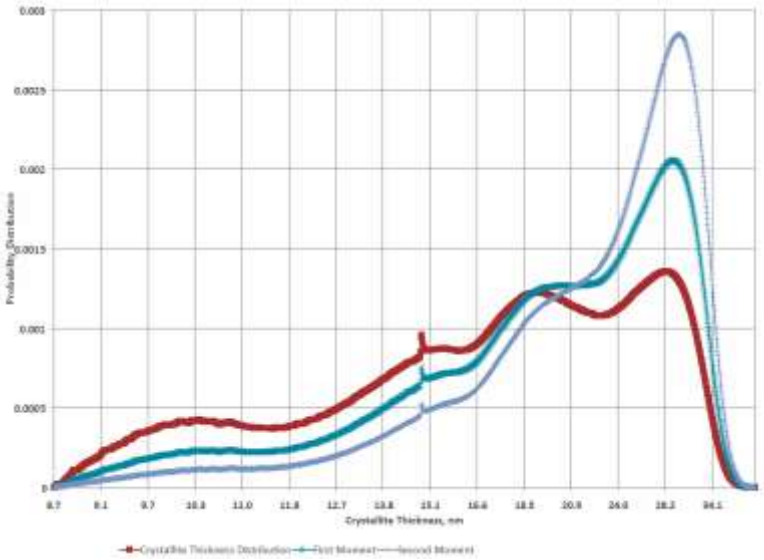

Figure 103: Run 1 of 8.3 kGy Proton Irradiated Sample (CPS04018D_1F)

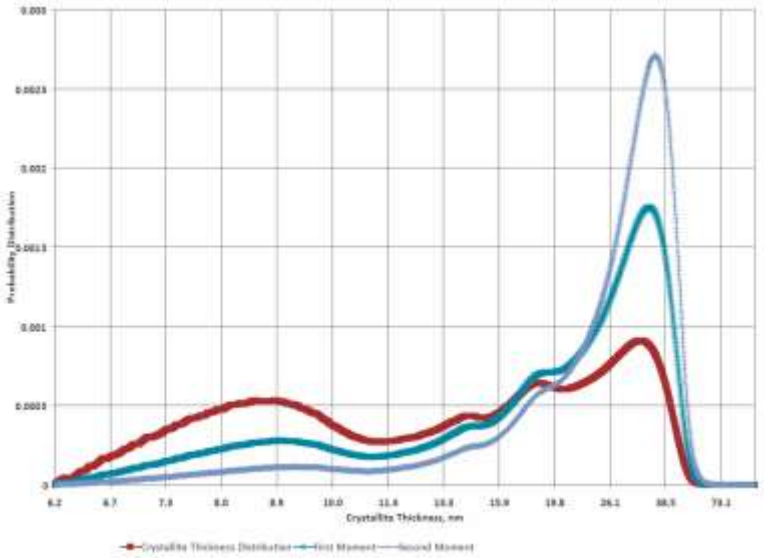

Figure 104: Run 1 of 8.7 kGy (Control) Proton Irradiated Sample (CPS04021B_1)

2.1.2 Melting Behavior of Thermally Treated Proton Irradiated UHMWPE (Run 2)

Table 25: Effect of Radiation for Run 2 of Proton Irradiated Samples

Dose (kGy)	Crystalinity
0	58 ± 3%
1.77	62 ± 4%
5.89	55 ± 4%

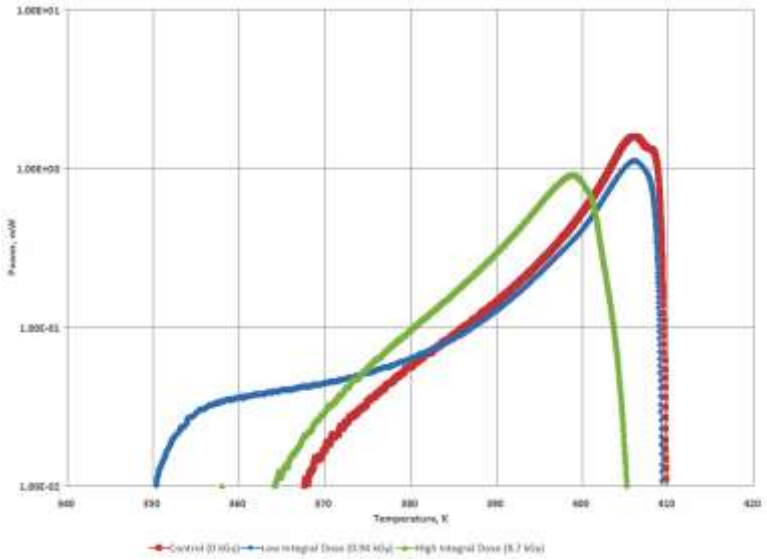

Figure 105: Endotherm for Run 2 of Proton Irradiated Samples

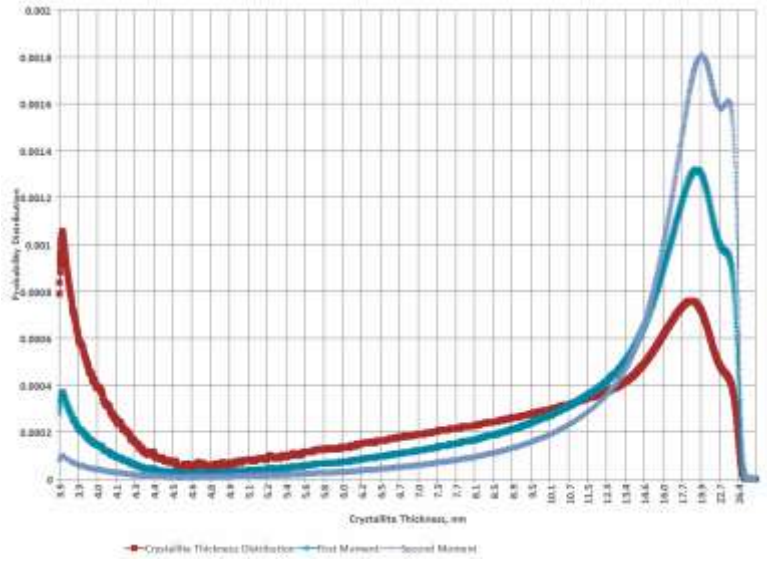

Figure 106: Run 2 of 0 kGy (Control) Proton Irradiated Sample (CPS04018B_3F)

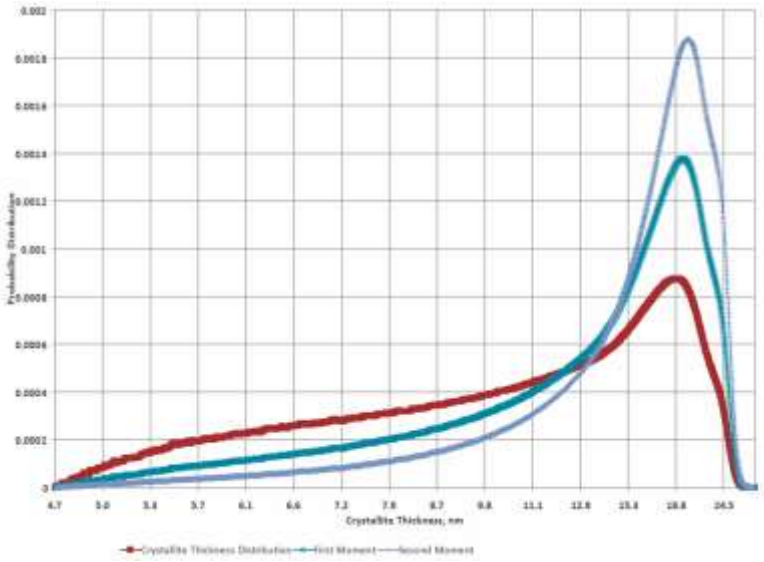

Figure 107: Run 2 of 0 kGy (Control) Proton Irradiated Sample (CPS04019C_3F)

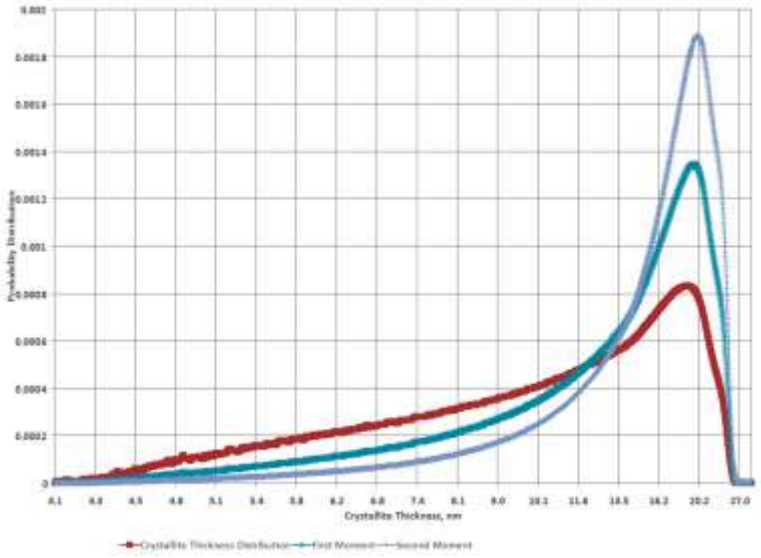

Figure 108: Run 2 of 0 kGy (Control) Proton Irradiated Sample (CPS04020C_3F)

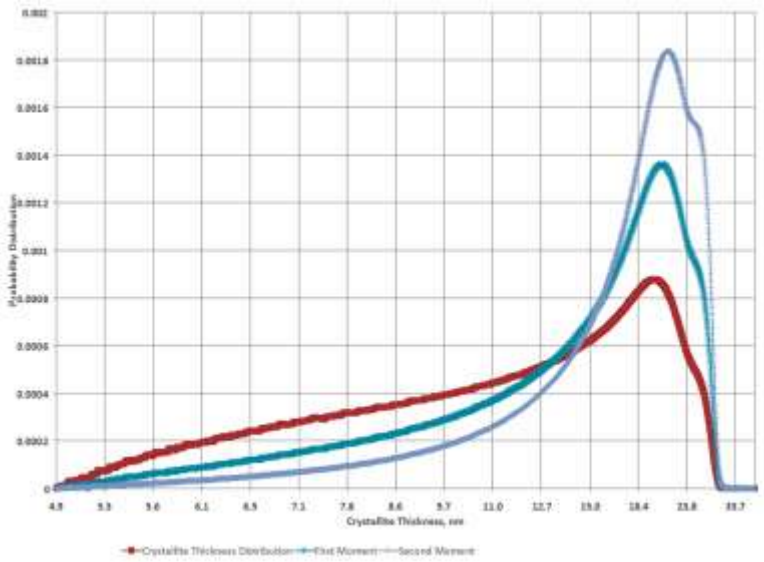

Figure 109: Run 2 of 0 kGy (Control) Proton Irradiated Sample (CPS04021A_3)

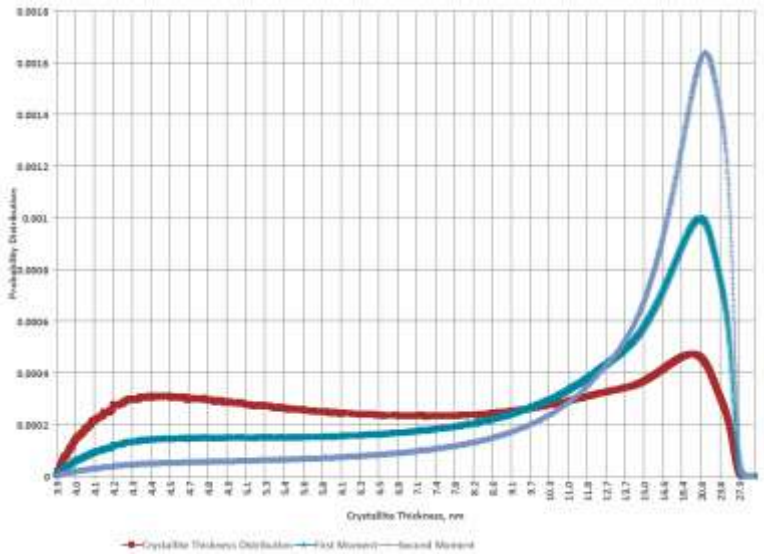

Figure 110: Run 2 of 0.94 kGy Proton Irradiated Sample (CPS04015C_3F)

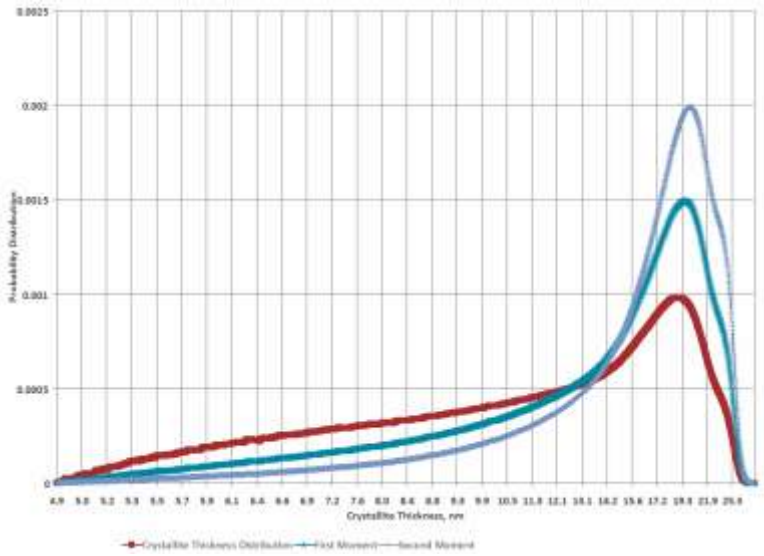

Figure 111: Run 2 of 0.96 kGy Proton Irradiated Sample (CPS04015A_3F)

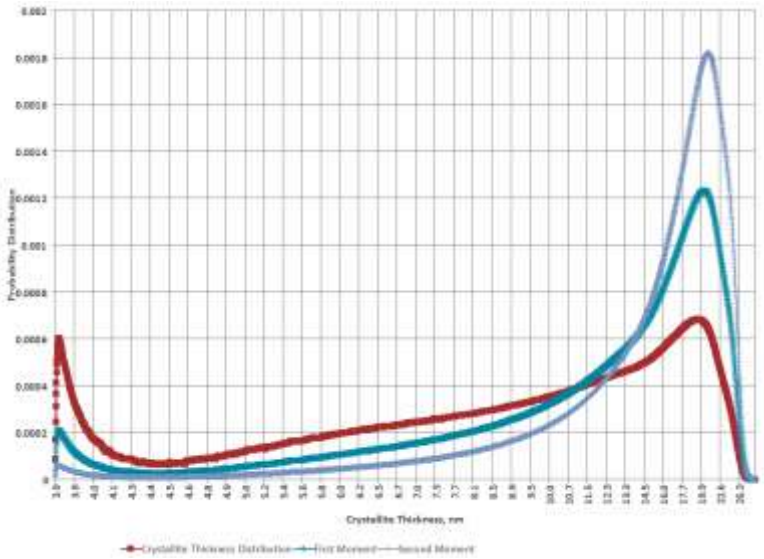

Figure 112: Run 2 of 1.08 kGy Proton Irradiated Sample (CPS04015B_3F)

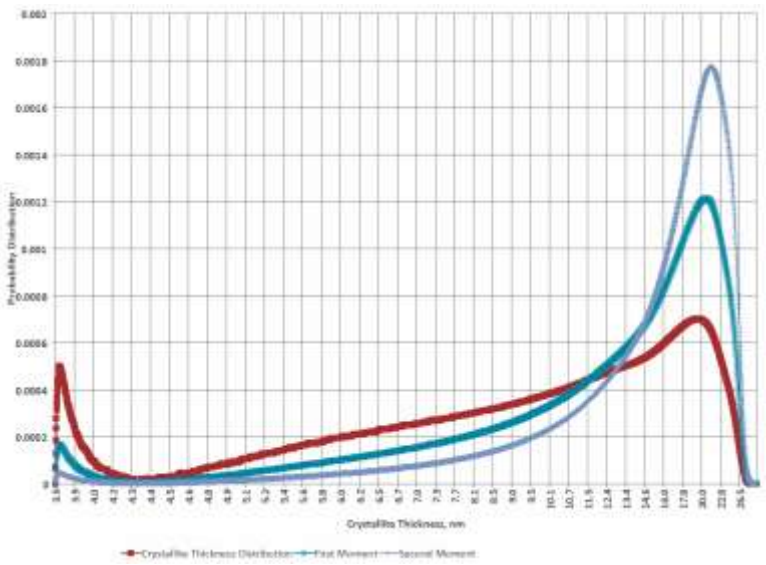

Figure 113: Run 2 of 1.15 kGy Proton Irradiated Sample (CPS04015D_3F)

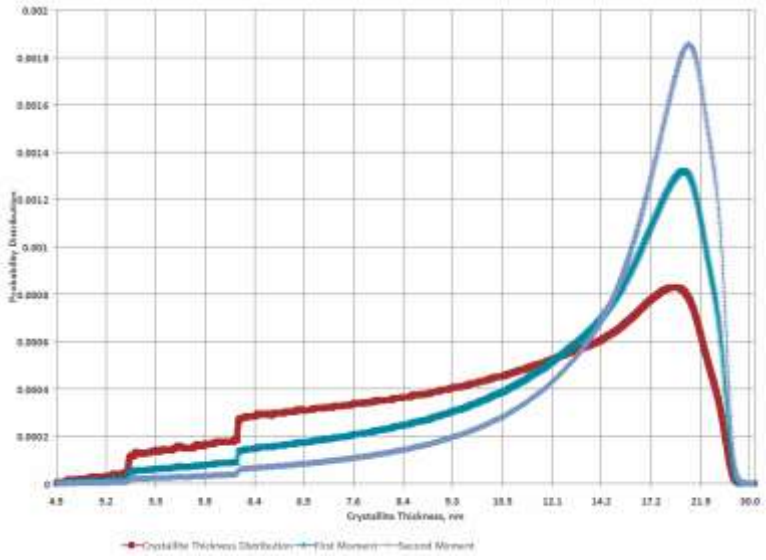

Figure 114: Run 2 of 1.33 kGy Proton Irradiated Sample (CPS04020B_3F)

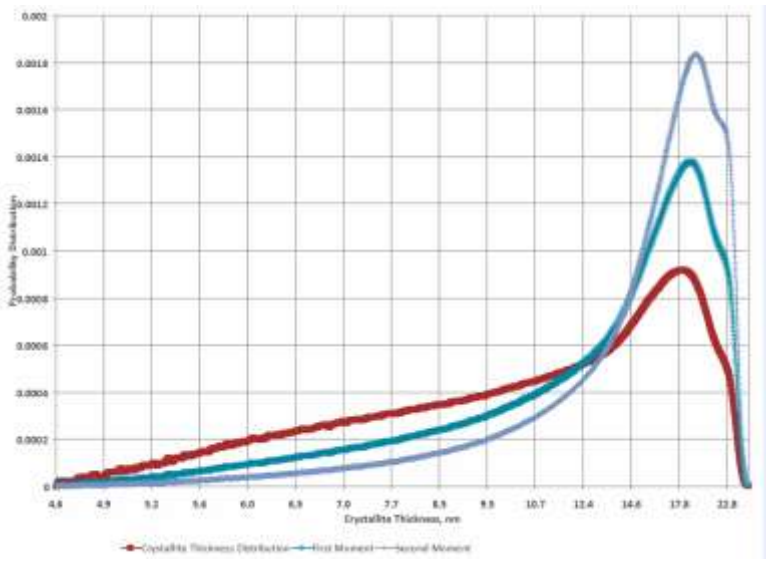

Figure 115: Run 2 of 1.33 kGy Proton Irradiated Sample (CPS04019B_3F)

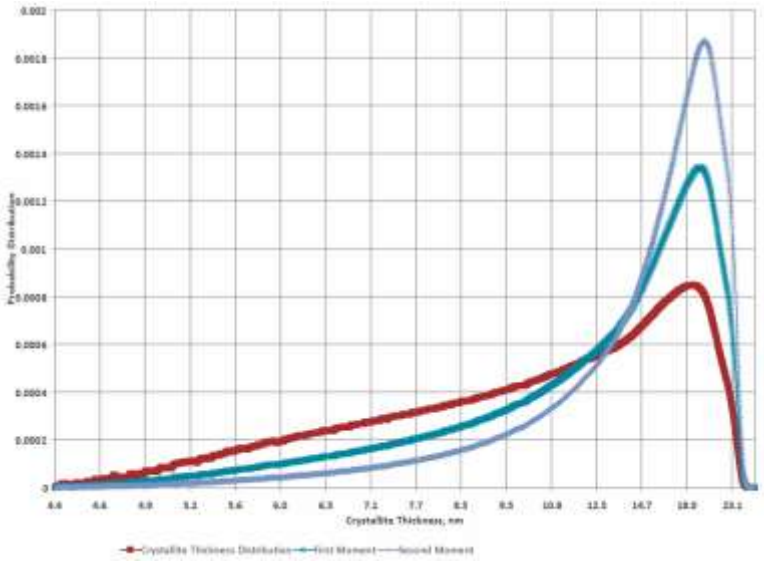

Figure 116: Run 2 of 3.7 kGy Proton Irradiated Sample (CPS04020A_3F)

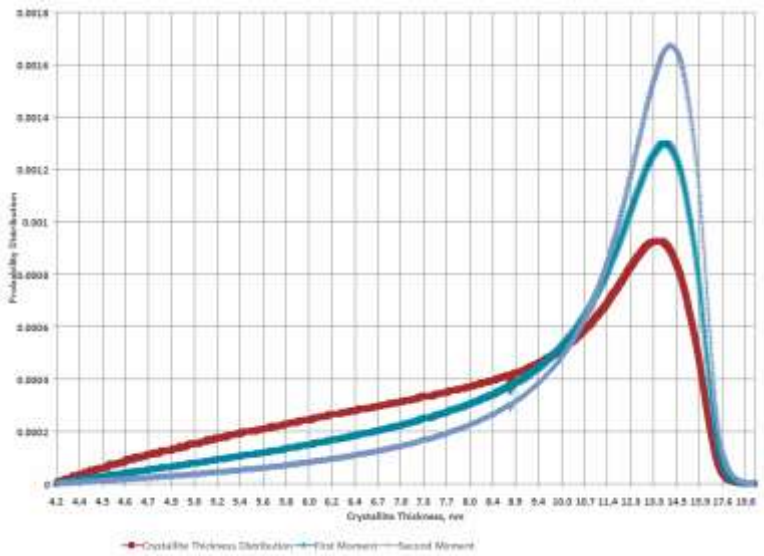

Figure 117: Run 2 of 6.8 kGy Proton Irradiated Sample (CPS04018C_3F)

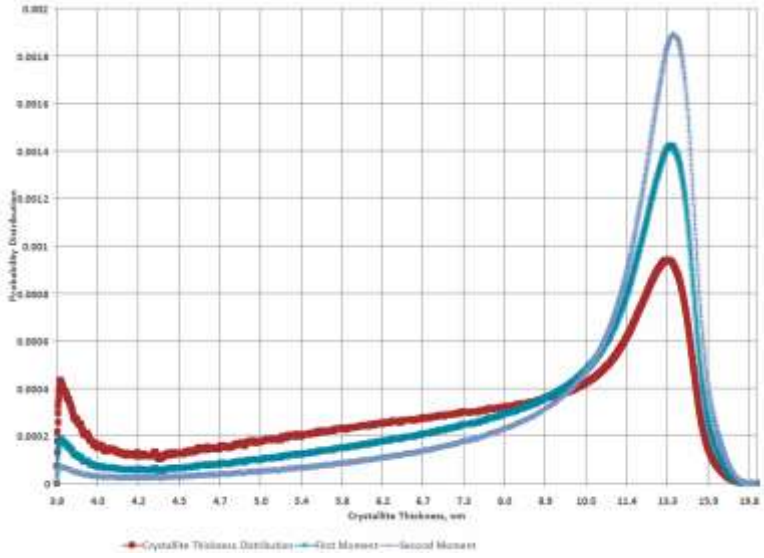

Figure 118: Run 2 of 8.3 kGy Proton Irradiated Sample (CPS04018D_3F)

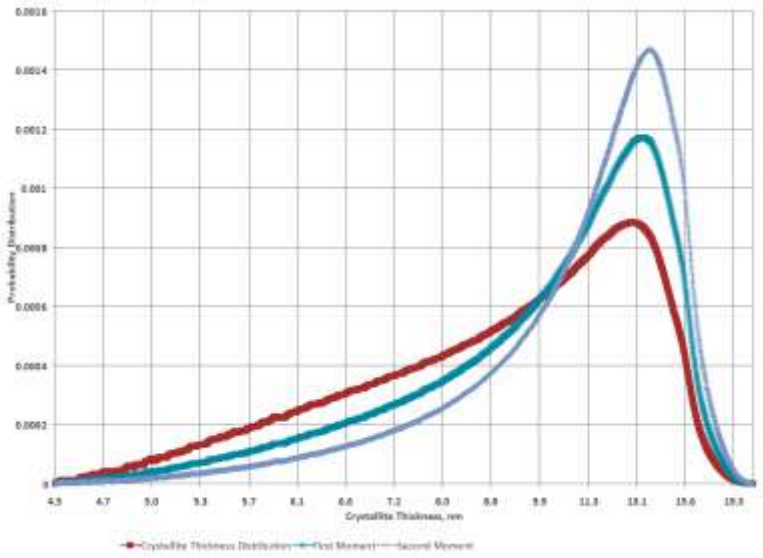

Figure 119: Run 2 of 8.7 kGy (Control) Proton Irradiated Sample (CPS04021B_3)

2.2 Crystallite Thickness

Table 26: Median and Maximum Crystallite Thicknesses for Proton Irradiation Control Samples

	Sample Number	19C		18B		20C		21A		Average	
	Run Number	1	2	1	2	1	2	1	2	1	2
Crystallite Thickness	Middle	24.53	17.06	14.01	17.63	24.71	16.65	20.76	18.30	21.00 ± 3.78	17.41 ± 1.82
	Maximum	41.74	27.61	31.28	30.87	40.39	29.79	35.45	29.63	37.22 ± 5.02	29.48 ± 3.90
First Moment	Middle	25.98	18.53	20.00	19.17	26.66	18.14	27.06	20.07	24.93 ± 3.33	18.98 ± 2.96
	Maximum	39.70	27.61	36.82	27.76	41.42	27.47	35.07	34.55	38.25 ± 2.70	29.35 ± 4.99
Second Moment	Middle	27.02	19.56	21.88	20.27	27.90	19.17	24.16	21.34	25.24 ± 2.72	20.09 ± 2.60
	Maximum	41.11	28.09	40.29	30.93	41.53	28.44	35.14	34.55	39.52 ± 3.20	30.50 ± 4.88

Table 27: Median and Maximum Crystallite Thicknesses for Low Integral Dose Proton Irradiation Samples

	Integral Dose	0.96		1.08		0.94		1.15		3.7		1.33	
	Sample Number	15A		15B		15C		15D		19A		19B	
	Run Number	1	2	1	2	1	2	1	2	1	2	1	2
Crystallite Thickness	Middle	25.25	17.36	24.31	17.02	26.02	16.65	25.9	17.24	25.06	14.96	22.24	16.6
	Maximum	40.49	27.2	40.09	27.99	40	28.44	41.85	28.44	39.03	26.27	39.6	25.41
First Moment	Middle	26.62	18.71	26.66	18.86	28.29	19.06	27.95	19.1	26.79	17.55	24.71	17.94
	Maximum	41.42	27.52	41.53	29.15	44.61	29.41	42.39	28.98	39.99	26.4	39.41	25.69
Second Moment	Middle	27.57	19.68	28.09	20.02	29.96	20.47	29.47	20.37	27.94	18.81	25.9	18.88
	Maximum	42.17	27.66	41.85	29.31	47.76	28.94	42.28	29.31	41.63	29.52	39.89	25.69

	Integral Dose	3.7		1.33		1.77 ± 1.2	
	Sample Number	20A		20B		Average	
	Run Number	1	2	1	2	1	2
Crystallite Thickness	Middle	26.27	16.24	24.71	16.9	24.97 ± 1.29	16.62 ± 0.76
	Maximum	41.63	24.94	41.85	27.43	40.57 ± 1.09	27.02 ± 1.34
First Moment	Middle	28.29	17.69	26.93	18.53	27.03 ± 1.18	18.43 ± 0.62
	Maximum	42.62	26.32	40.09	27.61	41.51 ± 1.71	27.64 ± 1.43
Second Moment	Middle	30.01	18.66	28.34	19.63	28.41 ± 1.38	19.57 ± 0.71
	Maximum	42.73	25.25	40.9	28.39	42.40 ± 2.34	28.01 ± 1.68

Table 28: Median and Maximum Crystallite Thicknesses for High Integral Dose Proton Irradiation Samples

	Integral Dose	6.8		8.3		8.7		7.93 ± 1	
	Sample Number	18C		18D		21B		Average	
	Run Number	1	2	1	2	1	2	1	2
Crystallite Thickness	Middle	24.83	12.29	23.7	11.99	28.14	11.85	25.56 ± 1.88	12.04 ± 0.18
	Maximum	49.81	19.44	39.03	18.53	59.69	19.26	49.51 ± 8.44	19.08 ± 0.39
First Moment	Middle	28.54	13.02	26.02	12.66	31.77	12.61	28.78 ± 2.35	12.76 ± 0.18
	Maximum	53.41	19.28	39.89	18.28	60.81	20.92	51.37 ± 8.66	19.49 ± 1.09
Second Moment	Middle	30.75	13.53	27.57	13.09	34.11	13.18	30.81 ± 2.67	13.27 ± 0.91
	Maximum	53.41	18.92	40.39	19.56	61.74	20.3	51.85 ± 8.79	19.59 ± 0.56

2.2.1 Crystallite Thickness of Post-Irradiated Samples (Run 1)

Table 29: Median Crystallite Thicknesses for Proton Irradiated Samples in the First DSC Run Crystallite Thickness

Dose (kGy)	Crystallite Thicknesss Distribution, ln	First Moment, lw	Second Moment, lz	lw/ln	lz/ln
0	21.00 ± 3.78	24.93 ± 3.33	25.24 ± 2.72	1.19	1.20
1.77	24.97 ± 1.29	27.03 ± 1.18	28.41 ± 1.38	1.08	1.14
5.89	25.56 ± 1.88	28.78 ± 2.35	30.81 ± 2.67	1.13	1.21

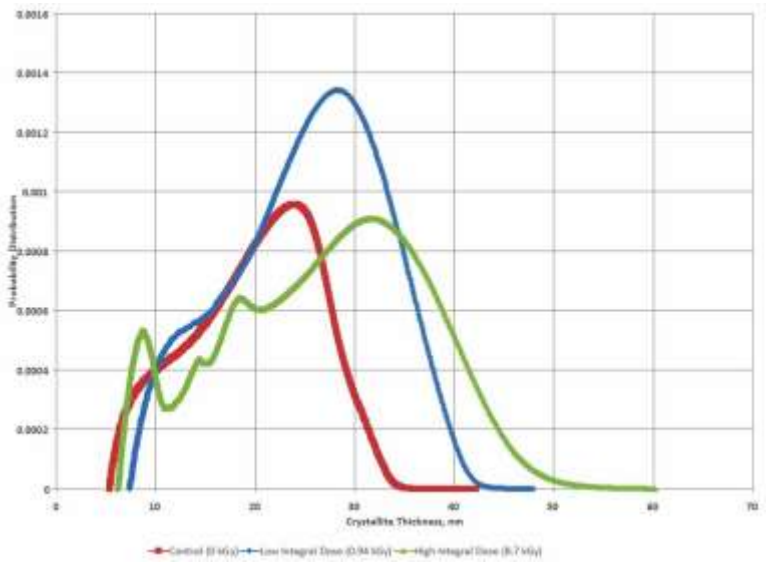

Figure 120: Crystallite Thickness Distribution of Run 1

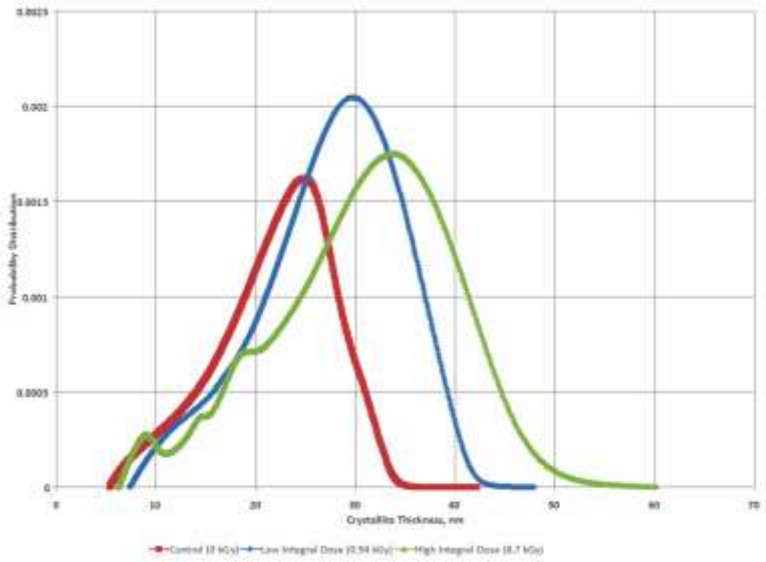

Figure 121: The First Moment of the Crystallite Thickness Distribution for Run 1

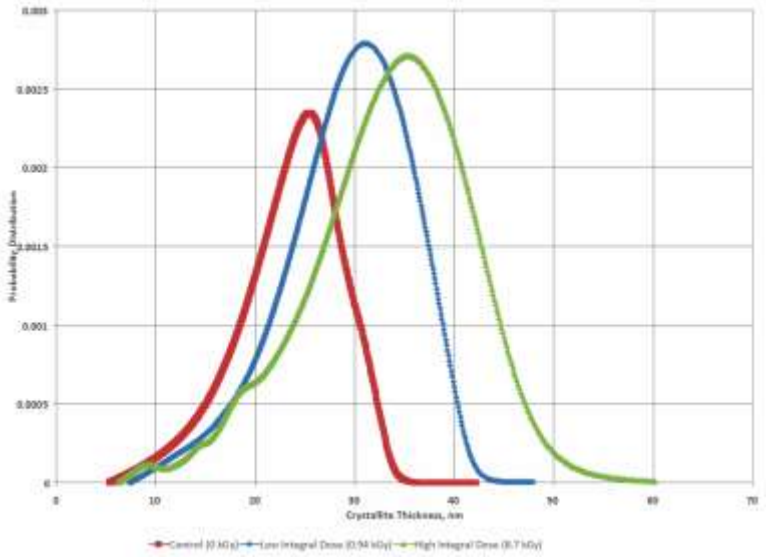

Figure 122: The Second Moment of the Crystallite Thickness Distribution for Run 1

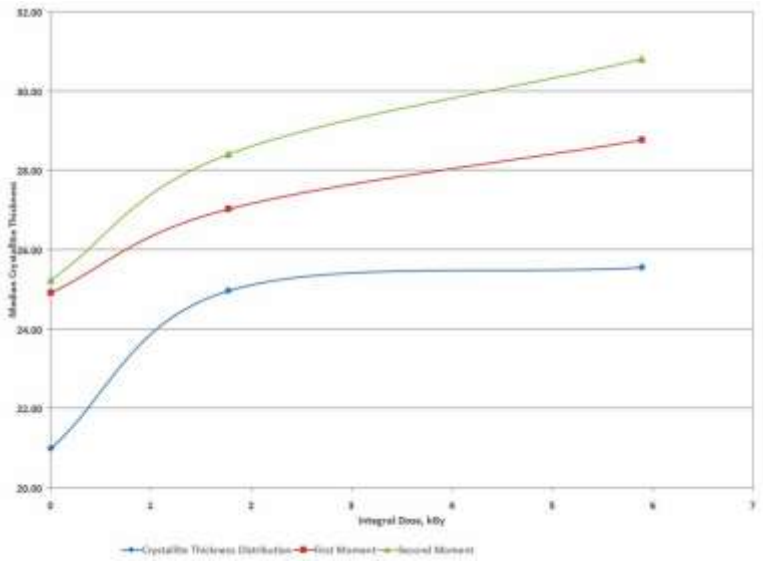

Figure 123: Median Crystallite Thicknesses for Proton Irradiated Samples in the First DSC Run

Table 30: Crystallizable Fraction and Sequence Length for Proton Irradiated Samples in the First DSC Run Dose

Dose (kGy)	Crystallizable Fraction	Sequence Length
0	0.964	82
1.77	0.970	98
5.89	0.971	100

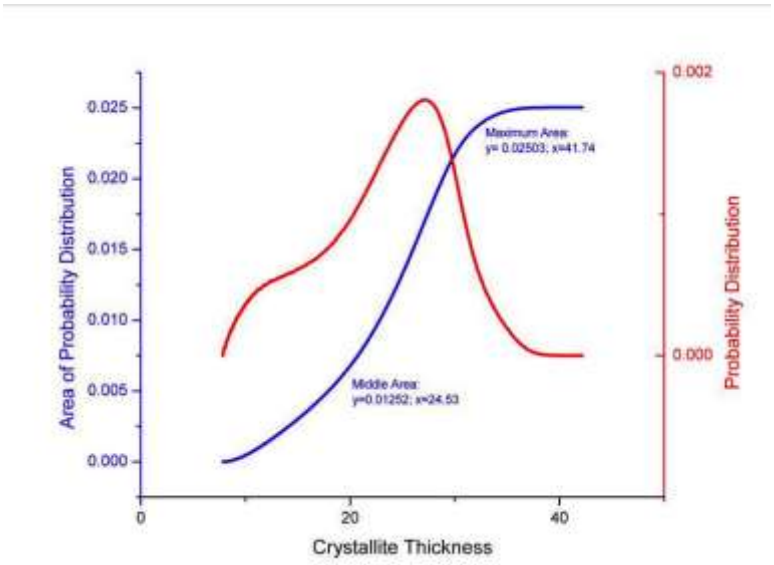

Figure 124: Control (0 kGy) Proton Irradiated (Sample 68) Crystallite Thickness Distribution for Run 1 (Area Calculations)

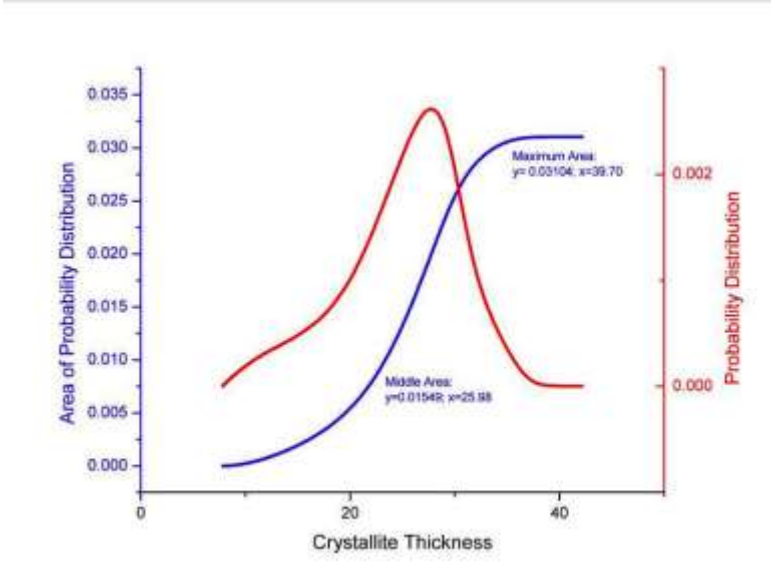

Figure 125: First Moment of Control (0 kGy) Proton Irradiated (Sample 68) Crystallite Thickness Distribution for Run 1 (Area Calculations)

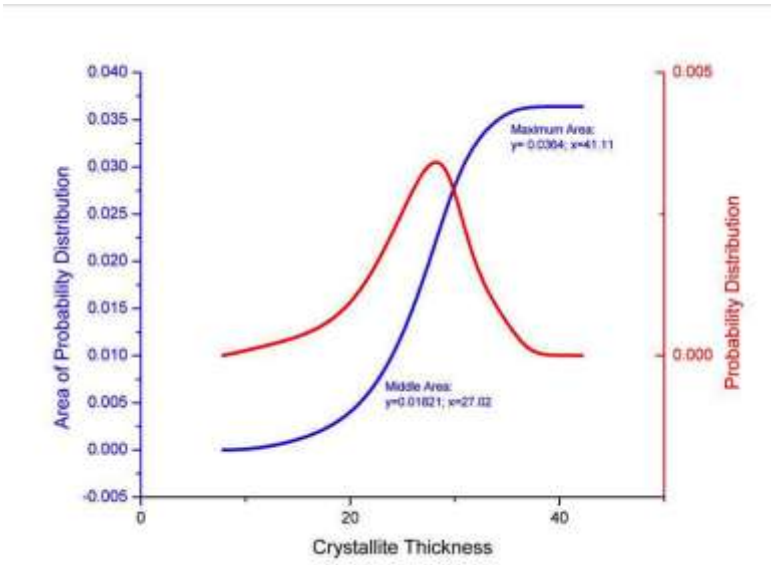

Figure 126: Second Moment of Control (0 kGy) Proton Irradiated (Sample 68) Crystallite Thickness Distribution for Run 1 (Area Calculations)

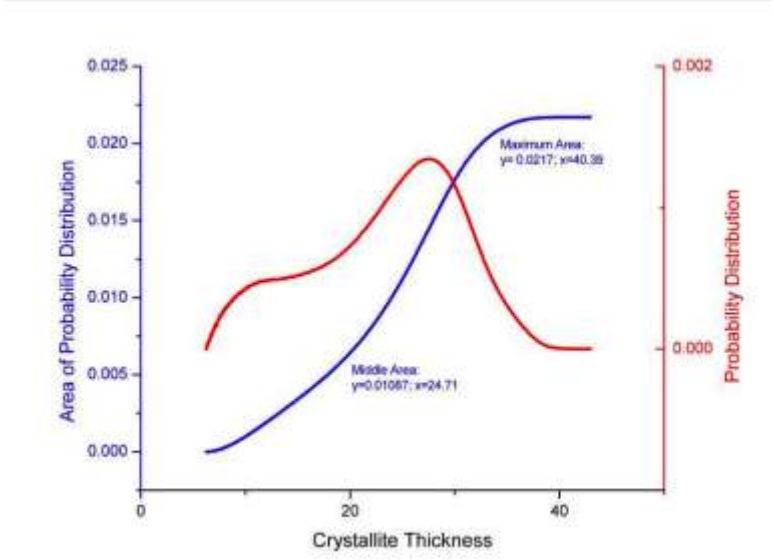

Figure 127: Control (0 kGy) Proton Irradiated (Sample 68) Crystallite Thickness Distribution for Run 1 (Area Calculations)

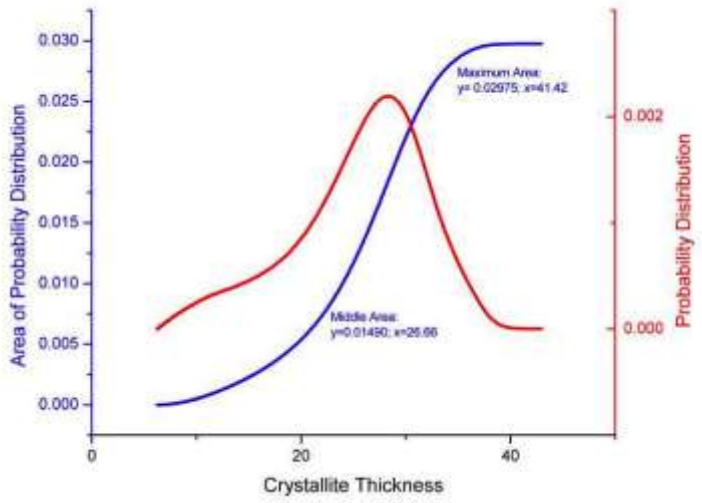

Figure 128: First Moment of Control (0 kGy) Proton Irradiated (Sample 68) Crystallite Thickness Distribution for Run 1 (Area Calculations)

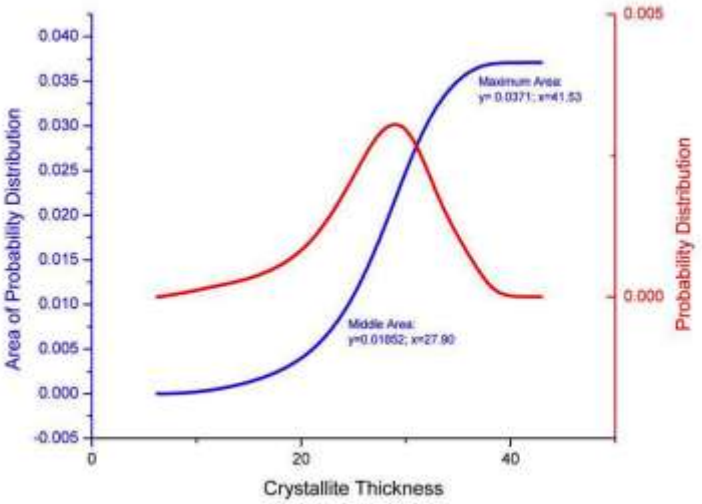

Figure 129: Second Moment of Control (0 kGy) Proton Irradiated (Sample 68) Crystallite Thickness Distribution for Run 1 (Area Calculations)

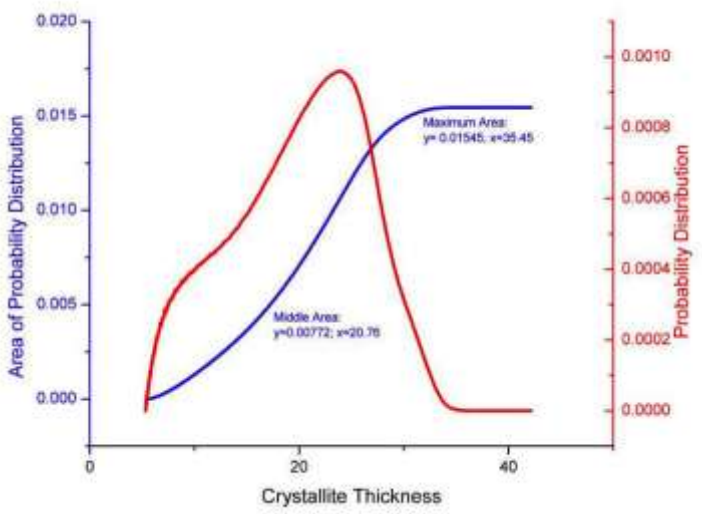

Figure 130: Control (0 kGy) Proton Irradiated (Sample 26) Crystallite Thickness Distribution for Run 1 (Area Calculations)

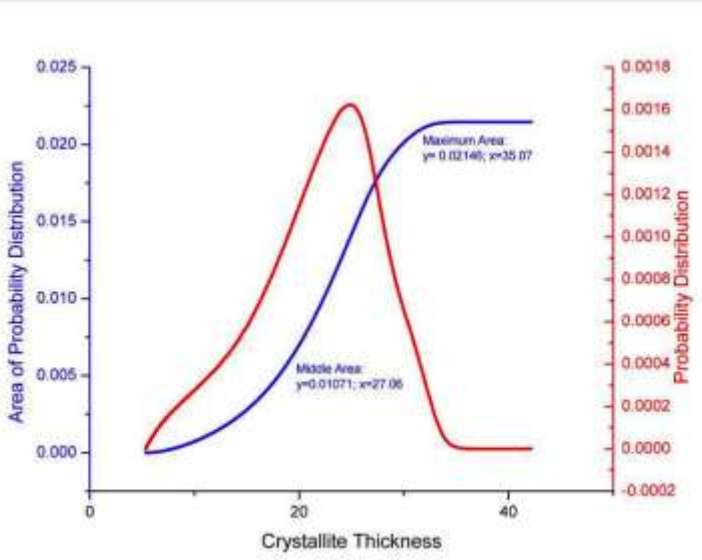

Figure 131: First Moment of Control (0 kGy) Proton Irradiated (Sample 26) Crystallite Thickness Distribution for Run 1 (Area Calculations)

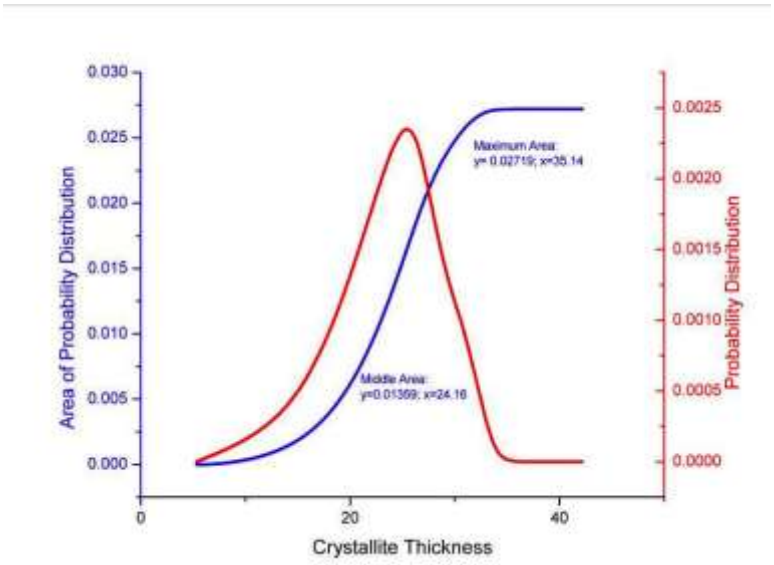

Figure 132: Second Moment of Control (0 kGy) Proton Irradiated (Sample 26) Crystallite Thickness Distribution for Run 1 (Area Calculations)

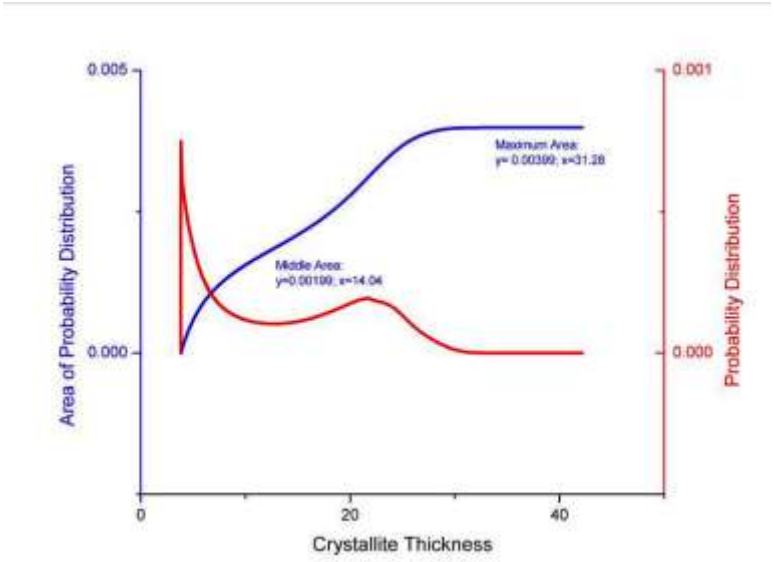

Figure 133: Control (0 kGy) Proton Irradiated (Sample 30) Crystallite Thickness Distribution for Run 1 (Area Calculations)

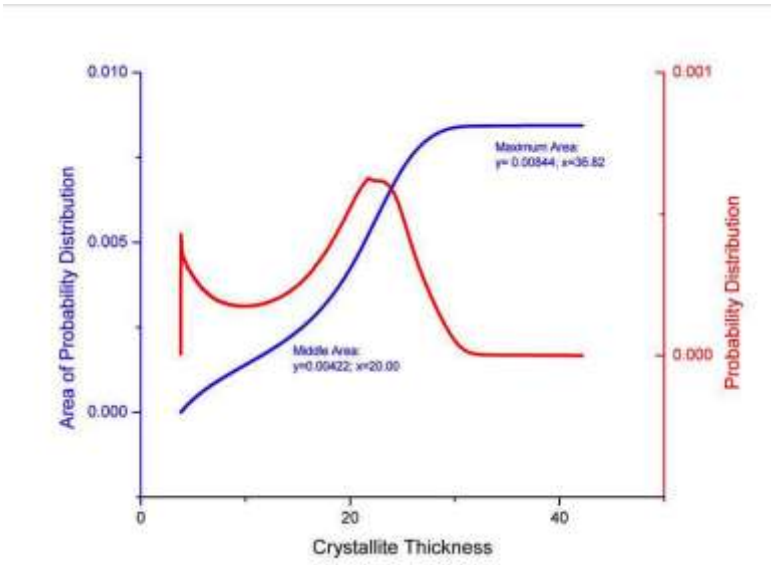

Figure 134: First Moment of Control (0 kGy) Proton Irradiated (Sample 30) Crystallite Thickness Distribution for Run 1 (Area Calculations)

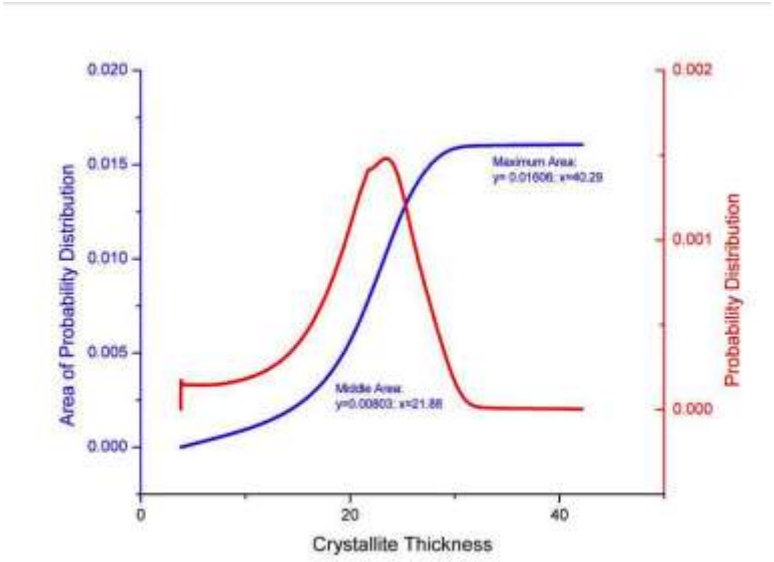

Figure 135: Second Moment of Control (0 kGy) Proton Irradiated (Sample 30) Crystallite Thickness Distribution for Run 1 (Area Calculations)

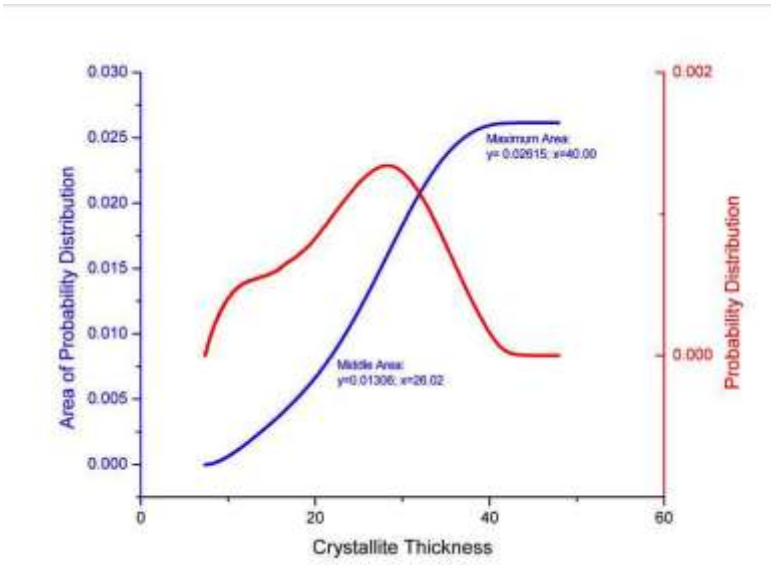

Figure 136: 0.9402 kGy Proton Irradiated (Sample 74) Crystallite Thickness Distribution for Run 1 (Area Calculations)

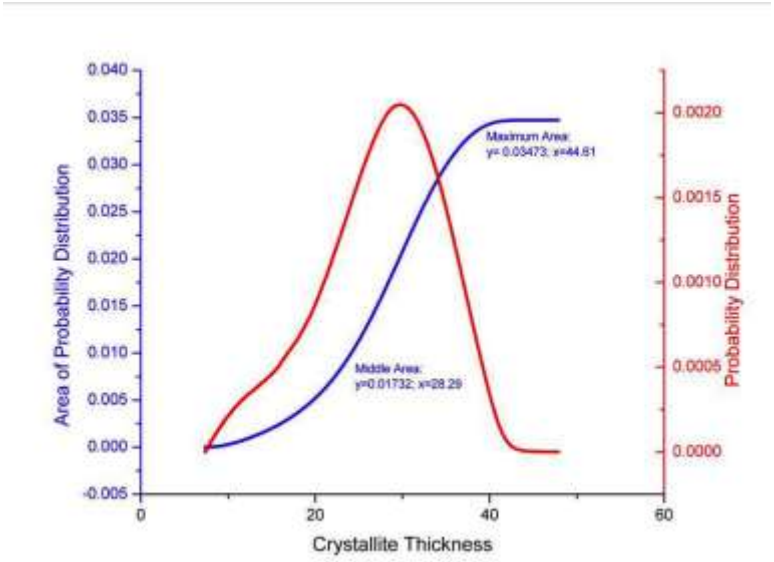

Figure 137: First Moment of 0.9402 kGy Proton Irradiated (Sample 74) Crystallite Thickness Distribution for Run 1 (Area Calculations)

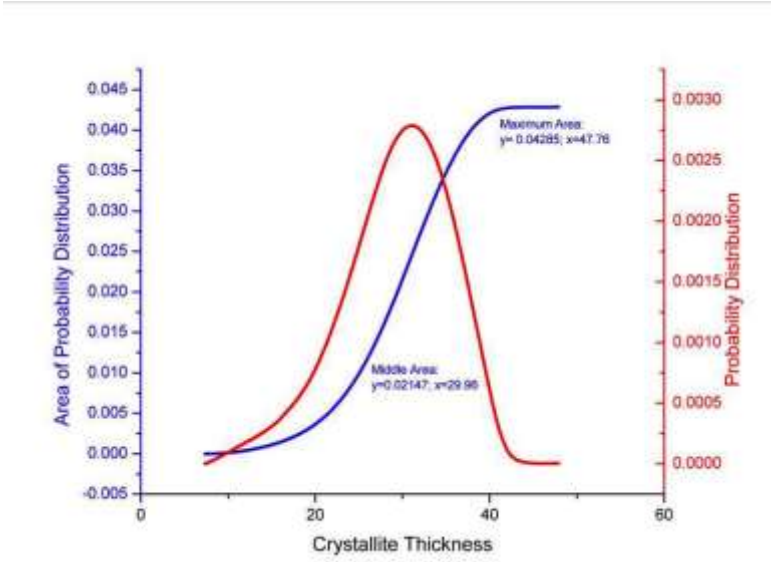

Figure 138: Second Moment of 0.9402 kGy Proton Irradiated (Sample 74) Crystallite Thickness Distribution for Run 1 (Area Calculations)

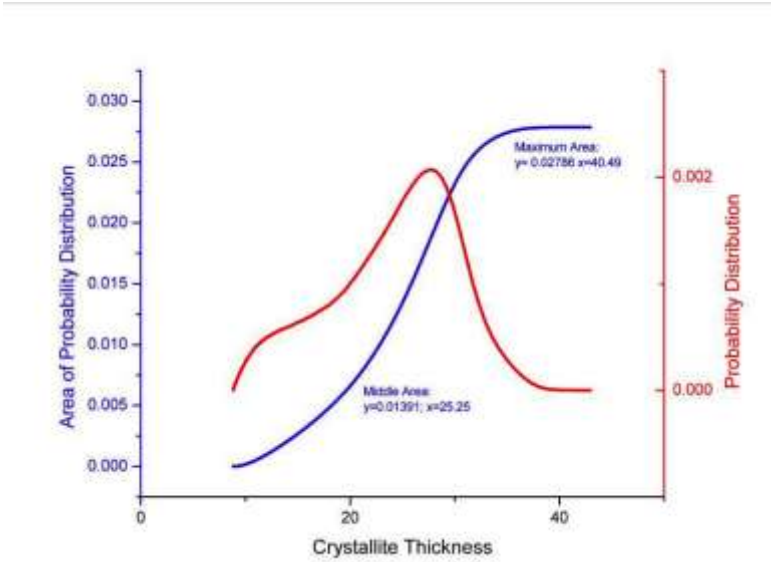

Figure 139: 0.963 kGy Proton Irradiated (Sample 66) Crystallite Thickness Distribution for Run 1 (Area Calculations)

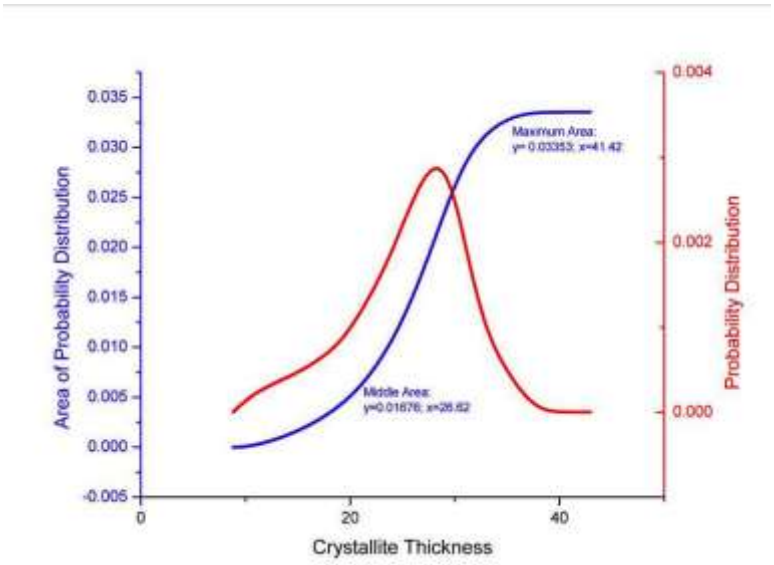

Figure 140: First Moment of 0.963 kGy Proton Irradiated (Sample 66) Crystallite Thickness Distribution for Run 1 (Area Calculations)

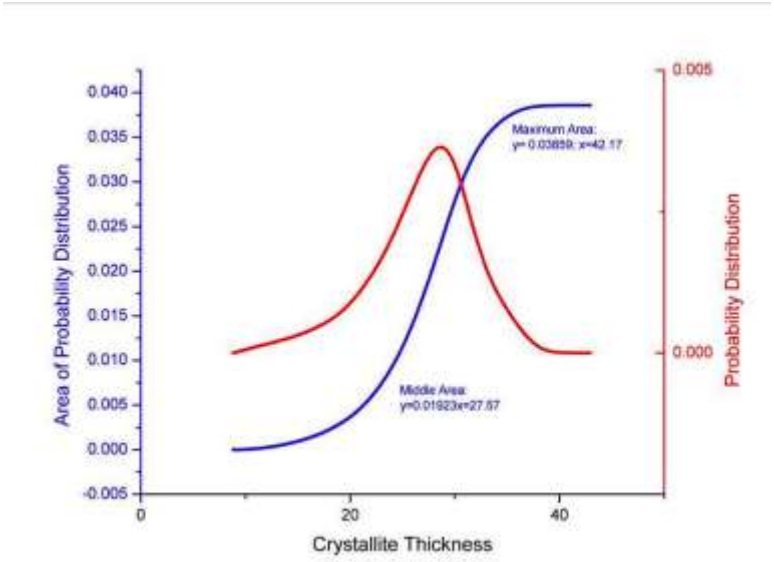

Figure 141: Second Moment of 0.963 kGy Proton Irradiated (Sample 66) Crystallite Thickness Distribution for Run 1 (Area Calculations)

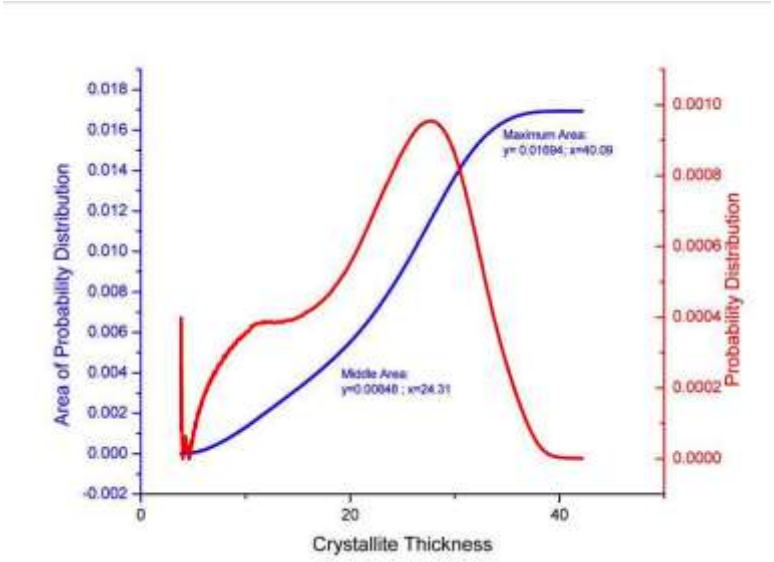

Figure 142: 1.0773 kGy Proton Irradiated (Sample 63) Crystallite Thickness Distribution for Run 1 (Area Calculations)

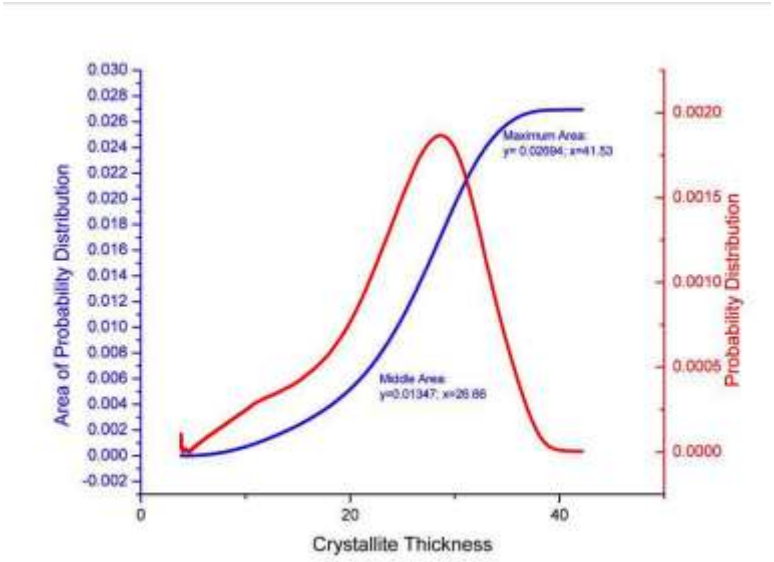

Figure 143: First Moment of 1.0773 kGy Proton Irradiated (Sample 63) Crystallite Thickness Distribution for Run 1 (Area Calculations)

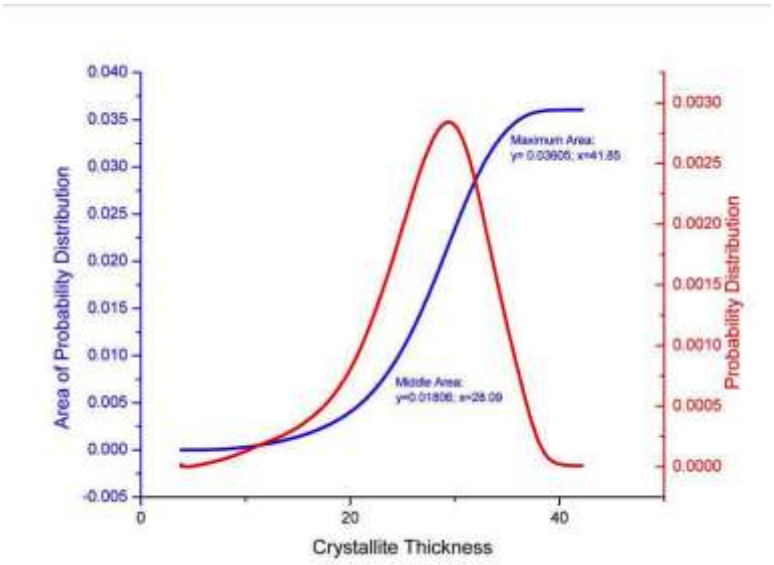

Figure 144: Second Moment of 1.0773 kGy Proton Irradiated (Sample 63) Crystallite Thickness Distribution for Run 1 (Area Calculations)

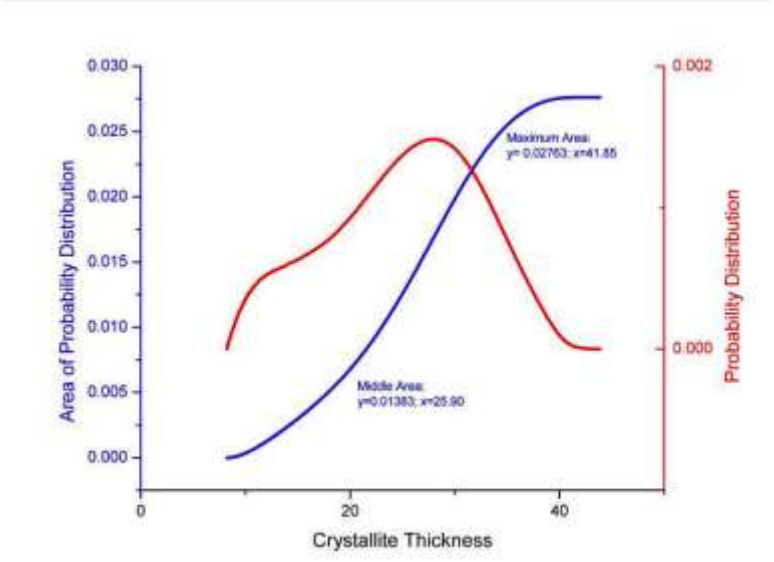

Figure 145: 1.1506 kGy Proton Irradiated (Sample 70) Crystallite Thickness Distribution for Run 1 (Area Calculations)

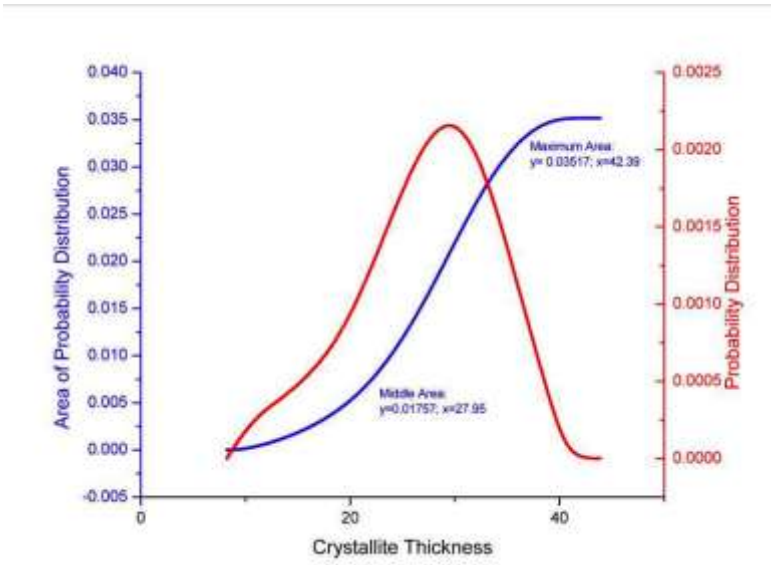

Figure 146: First Moment of 1.1506 kGy Proton Irradiated (Sample 70) Crystallite Thickness Distribution for Run 1 (Area Calculations)

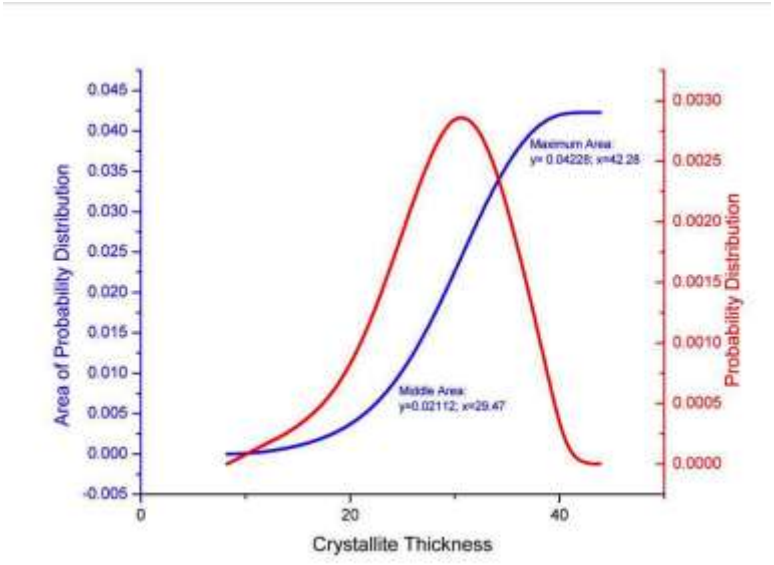

Figure 147: Second Moment of 1.1506 kGy Proton Irradiated (Sample 70) Crystallite Thickness Distribution for Run 1 (Area Calculations)

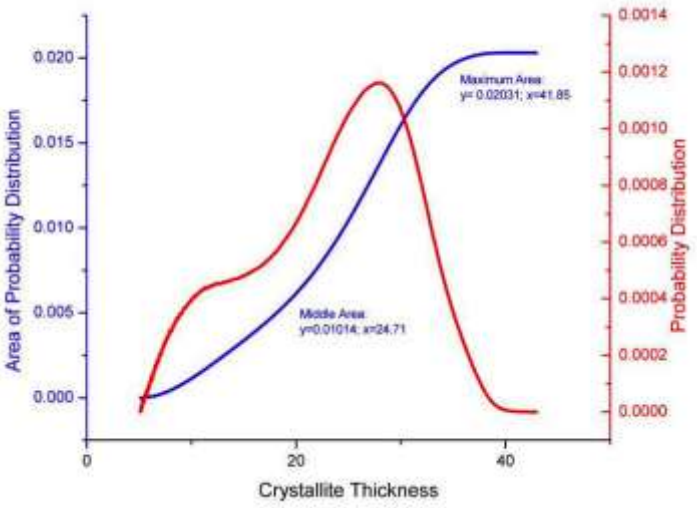

Figure 148: 1.3289 kGy Proton Irradiated (Sample 57) Crystallite Thickness Distribution for Run 1 (Area Calculations)

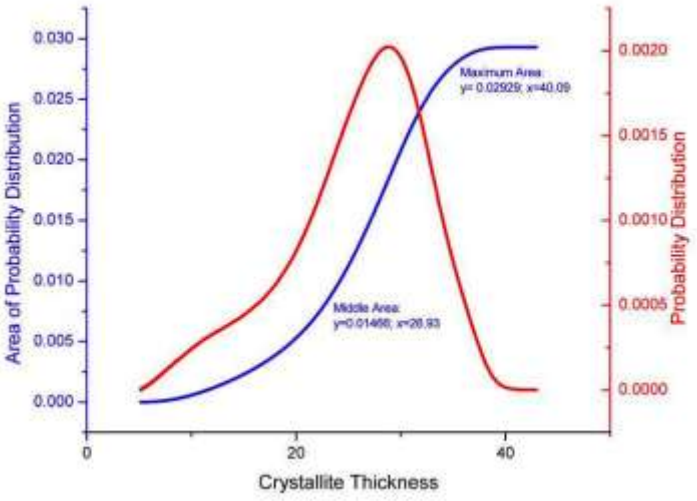

Figure 149: First Moment of 1.3289 kGy Proton Irradiated (Sample 57) Crystallite Thickness Distribution for Run 1 (Area Calculations)

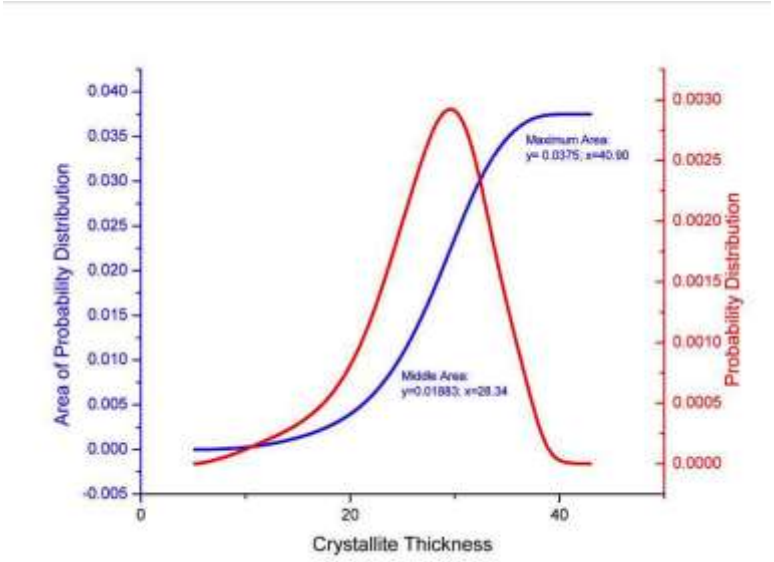

Figure 150: Second Moment of 1.3289 kGy Proton Irradiated (Sample 57) Crystallite Thickness Distribution for Run 1 (Area Calculations)

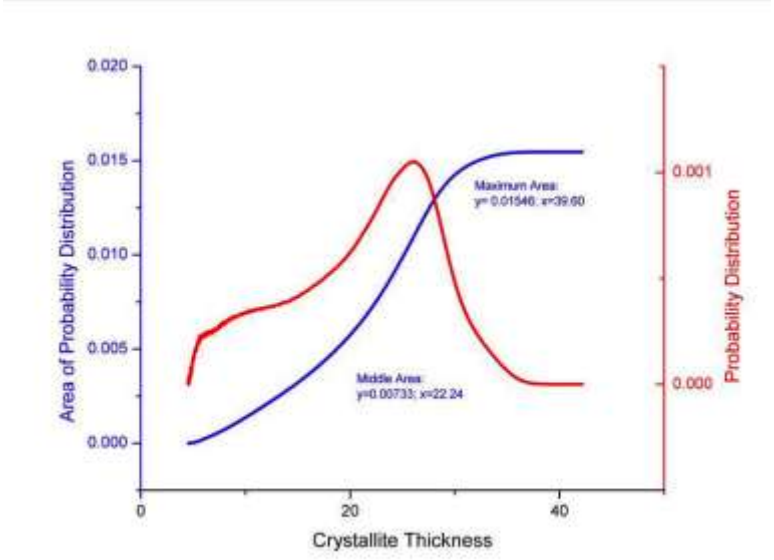

Figure 151: 1.3289 kGy Proton Irradiated (Sample 57) Crystallite Thickness Distribution for Run 1 (Area Calculations)

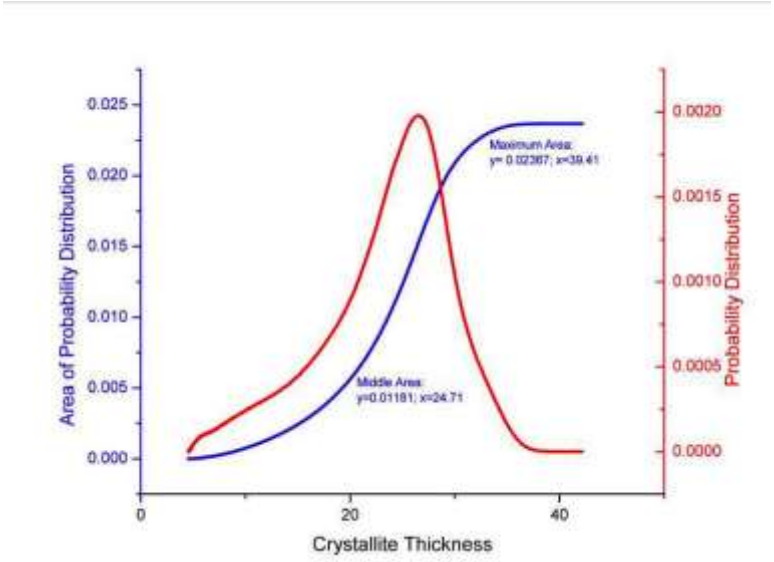

Figure 152: First Moment of 1.3289 kGy Proton Irradiated (Sample 57) Crystallite Thickness Distribution for Run 1 (Area Calculations)

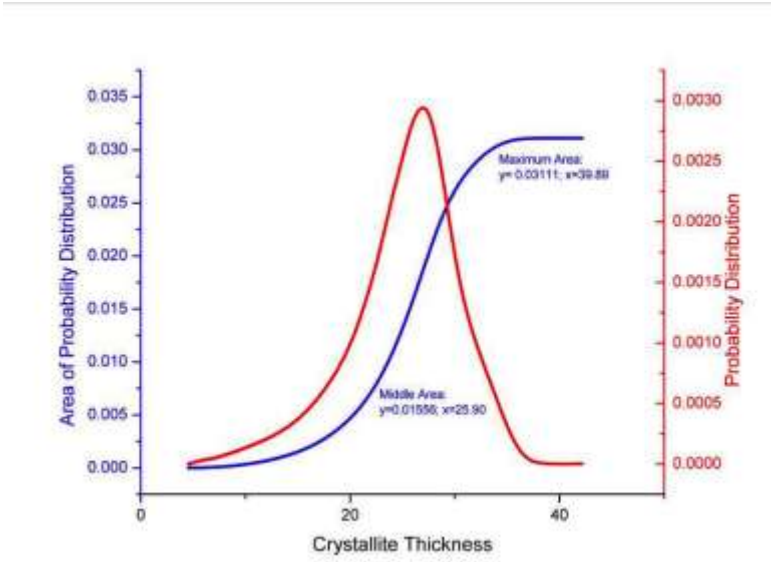

Figure 153: Second Moment of 1.3289 kGy Proton Irradiated (Sample 57) Crystallite Thickness Distribution for Run 1 (Area Calculations)

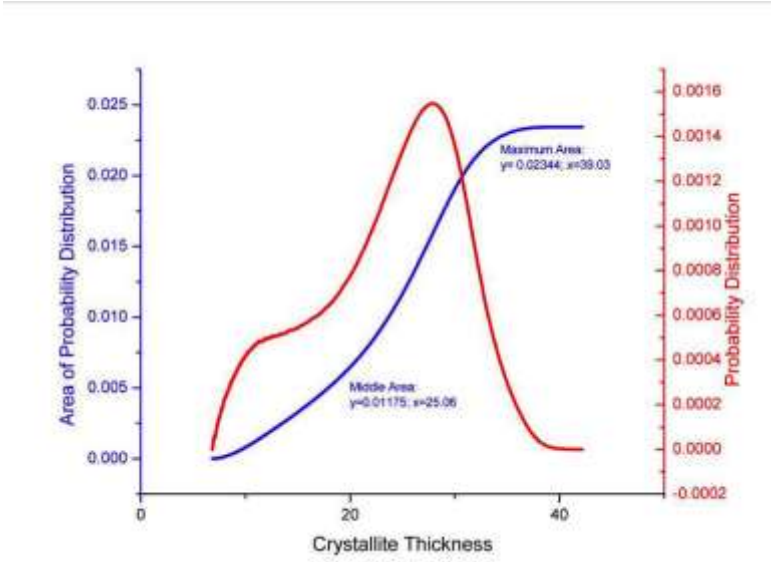

Figure 154: 3.7 kGy Proton Irradiated (Sample 58) Crystallite Thickness Distribution for Run 1 (Area Calculations)

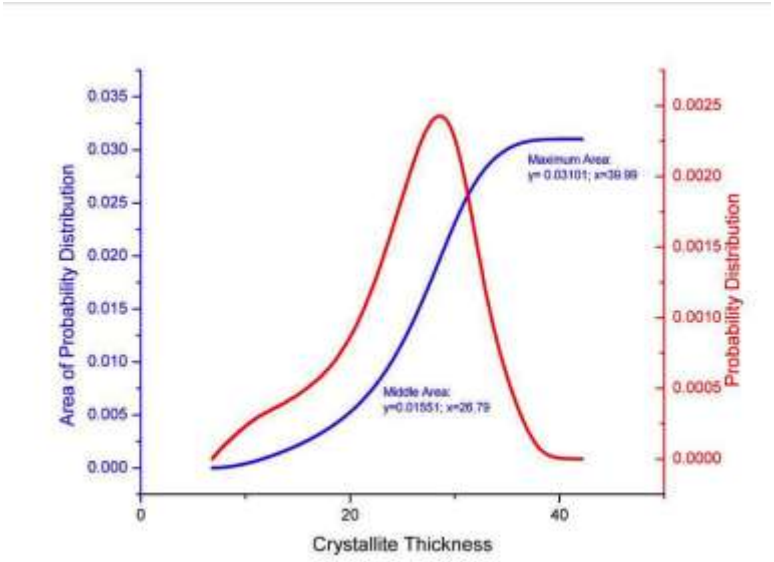

Figure 155: First Moment of 3.7 kGy Proton Irradiated (Sample 58) Crystallite Thickness Distribution for Run 1 (Area Calculations)

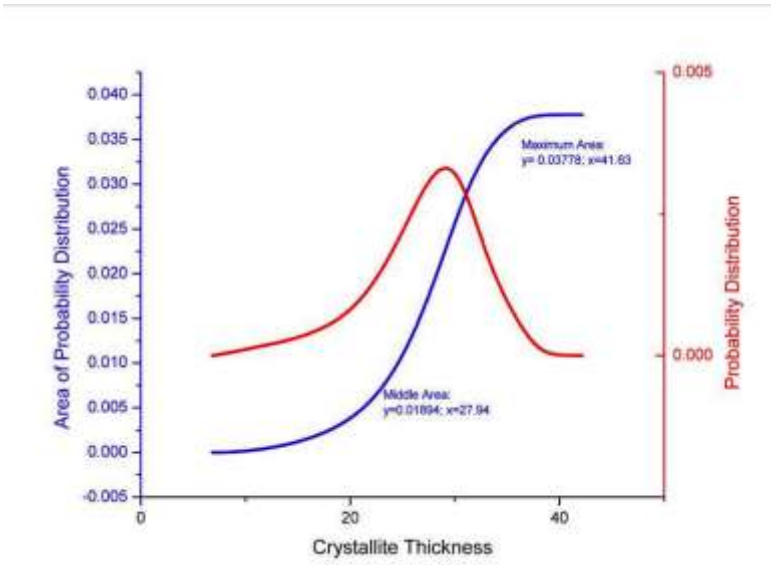

Figure 156: Second Moment of 3.7 kGy Proton Irradiated (Sample 58) Crystallite Thickness Distribution for Run 1 (Area Calculations)

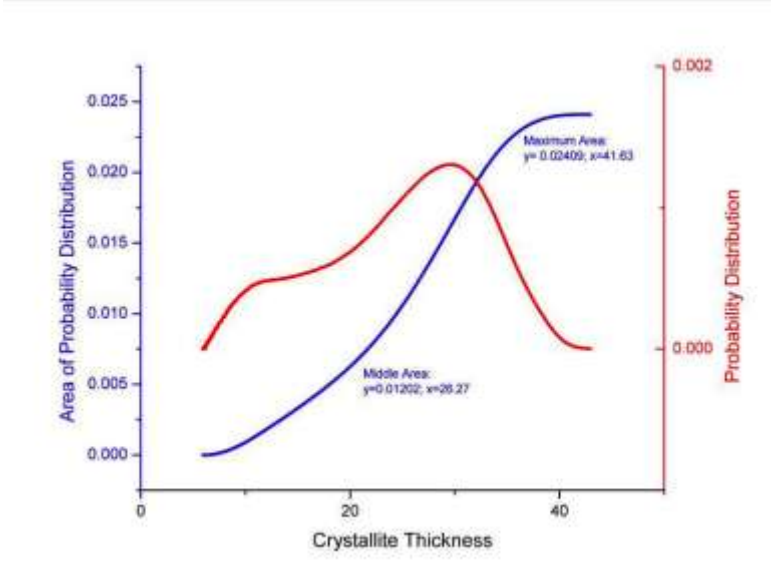

Figure 157: 3.7 kGy Proton Irradiated (Sample 58) Crystallite Thickness Distribution for Run 1 (Area Calculations)

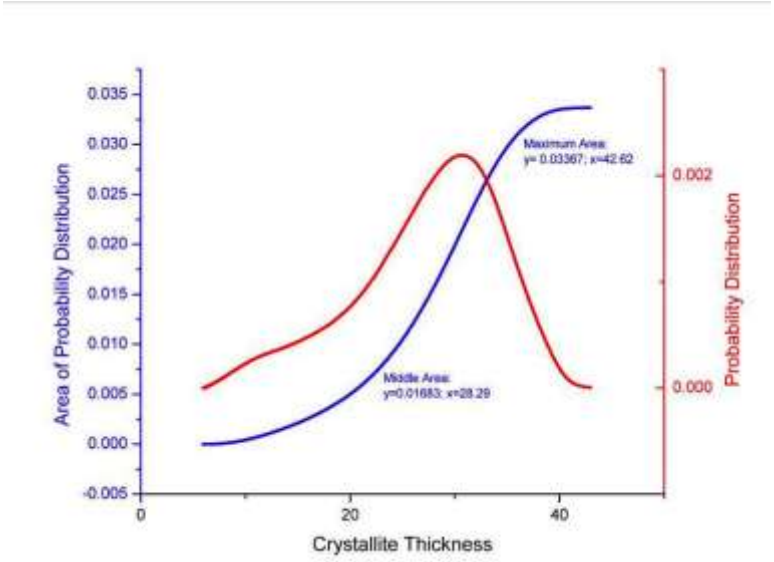

Figure 158: First Moment of 3.7 kGy Proton Irradiated (Sample 58) Crystallite Thickness Distribution for Run 1 (Area Calculations)

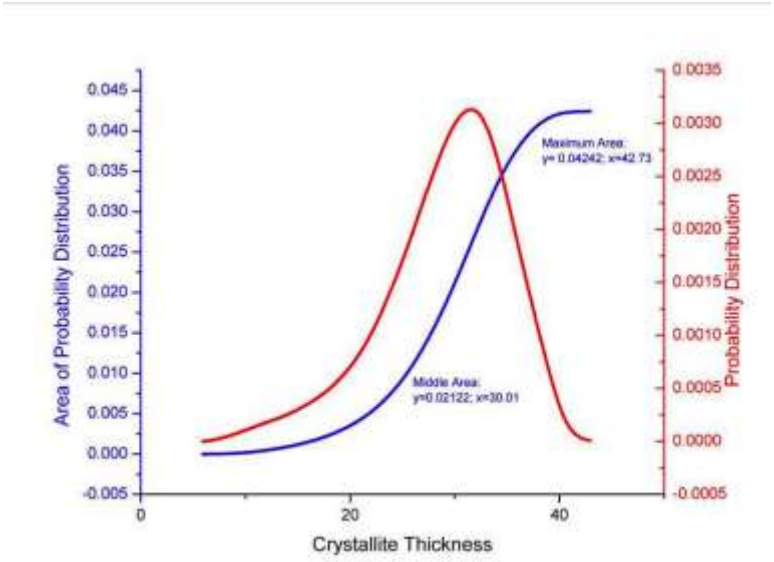

Figure 159: Second Moment of 3.7 kGy Proton Irradiated (Sample 58) Crystallite Thickness Distribution for Run 1 (Area Calculations)

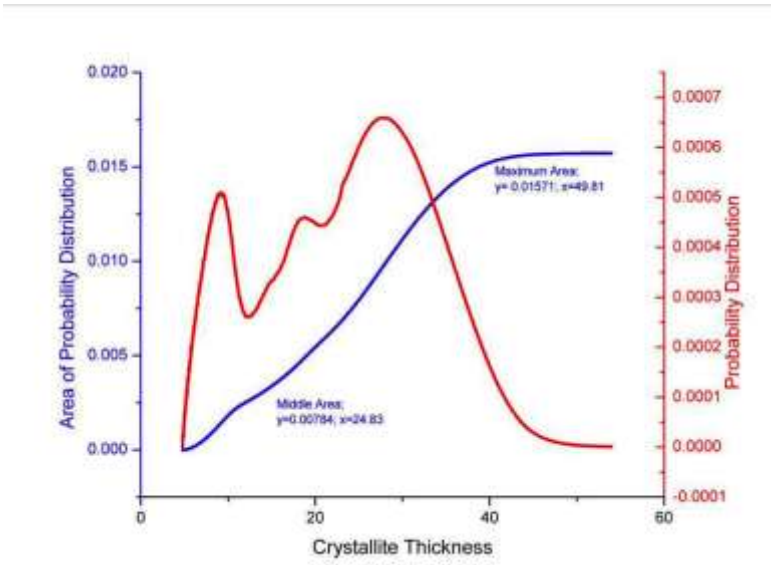

Figure 160: 6.8 kGy Proton Irradiated (Sample 87) Crystallite Thickness Distribution for Run 1 (Area Calculations)

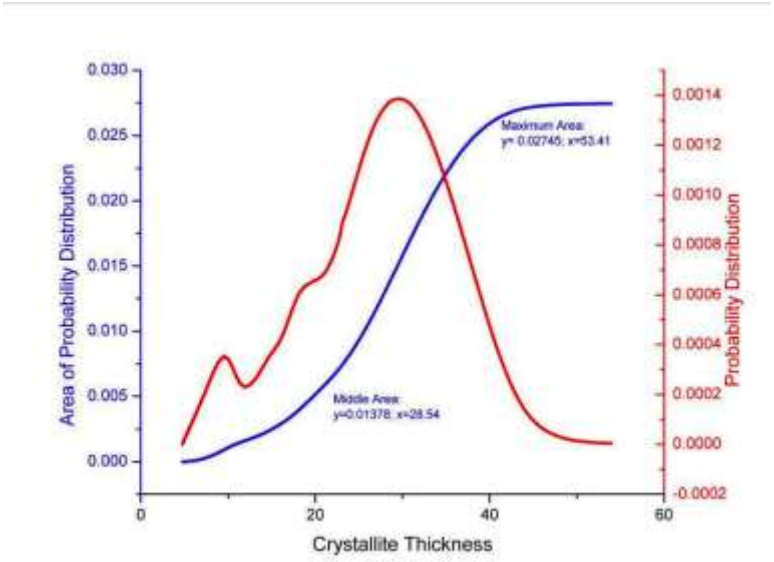

Figure 161: First Moment of 6.8 kGy Proton Irradiated (Sample 87) Crystallite Thickness Distribution for Run 1 (Area Calculations)

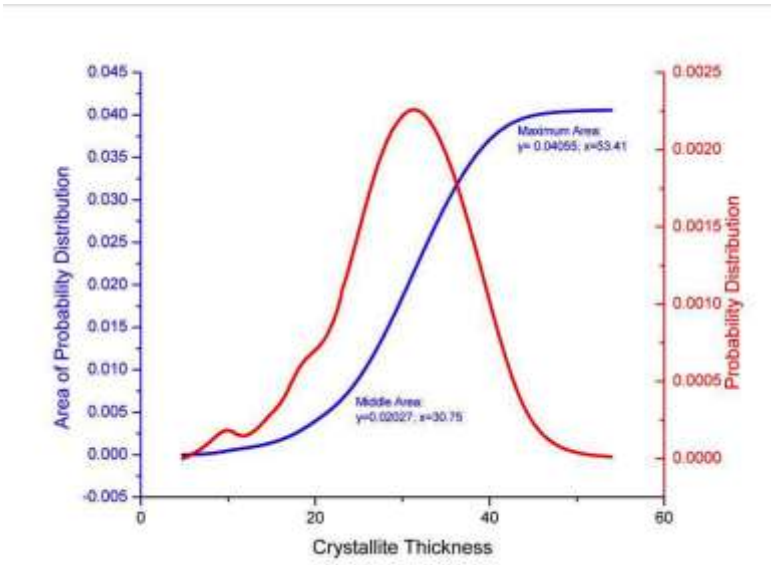

Figure 162: Second Moment of 6.8 kGy Proton Irradiated (Sample 87) Crystallite Thickness Distribution for Run 1 (Area Calculations)

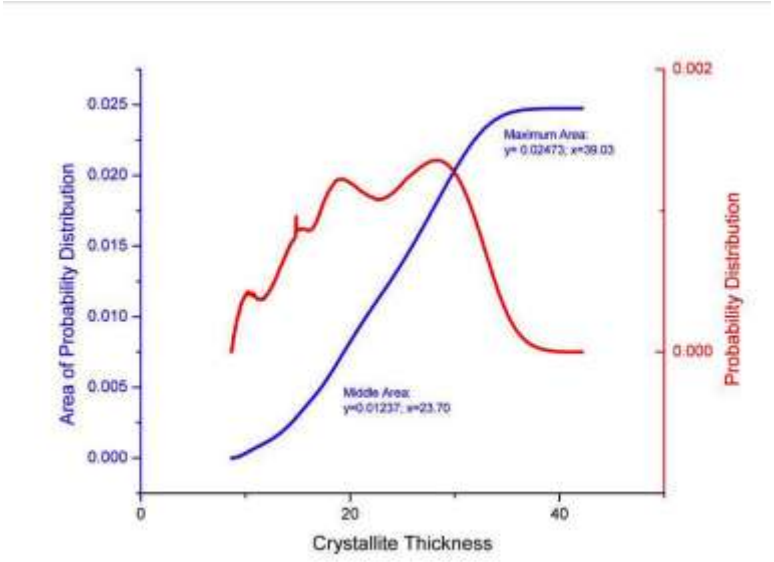

Figure 163: 8.3 kGy Proton Irradiated (Sample 80) Crystallite Thickness Distribution for Run 1 (Area Calculations)

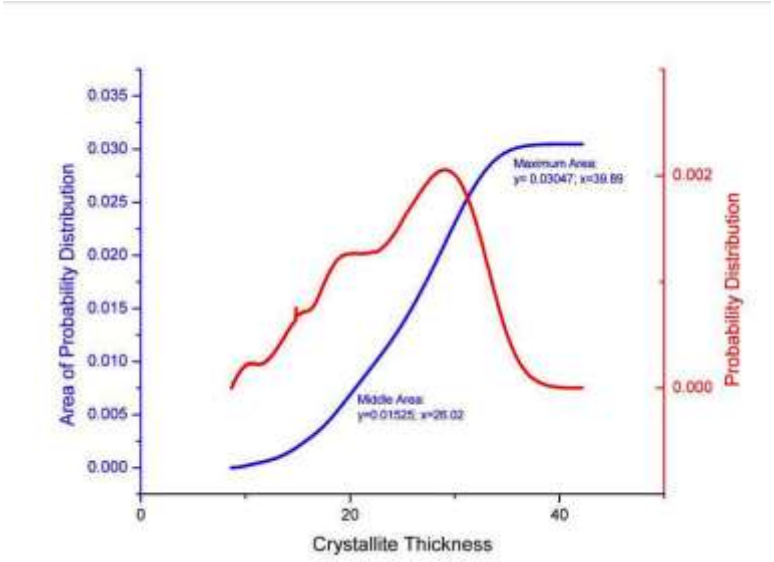

Figure 164: First Moment of 8.3 kGy Proton Irradiated (Sample 80) Crystallite Thickness Distribution for Run 1 (Area Calculations)

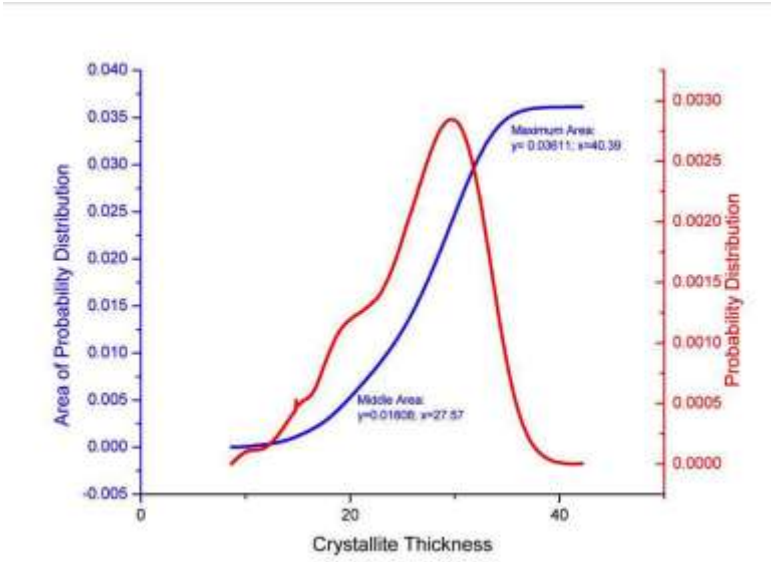

Figure 165: Second Moment of 8.3 kGy Proton Irradiated (Sample 80) Crystallite Thickness Distribution for Run 1 (Area Calculations)

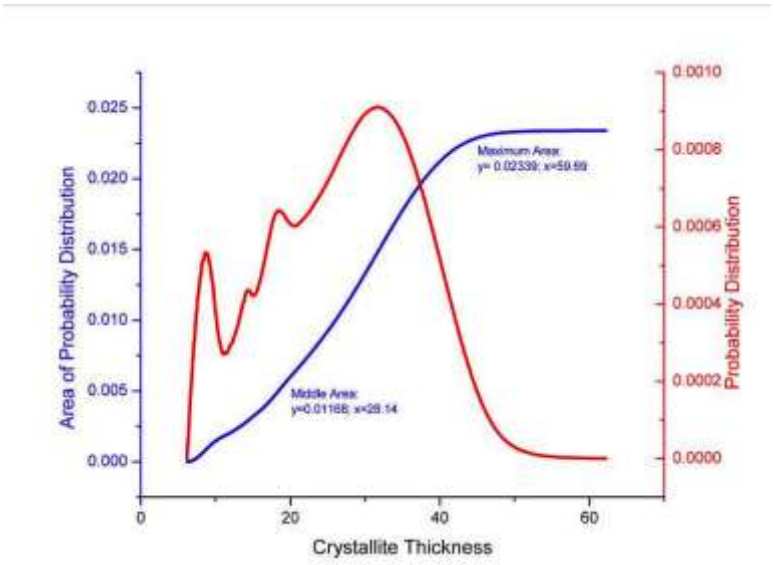

Figure 166: 8.7 kGy Proton Irradiated (Sample 83) Crystallite Thickness Distribution for Run 1 (Area Calculations)

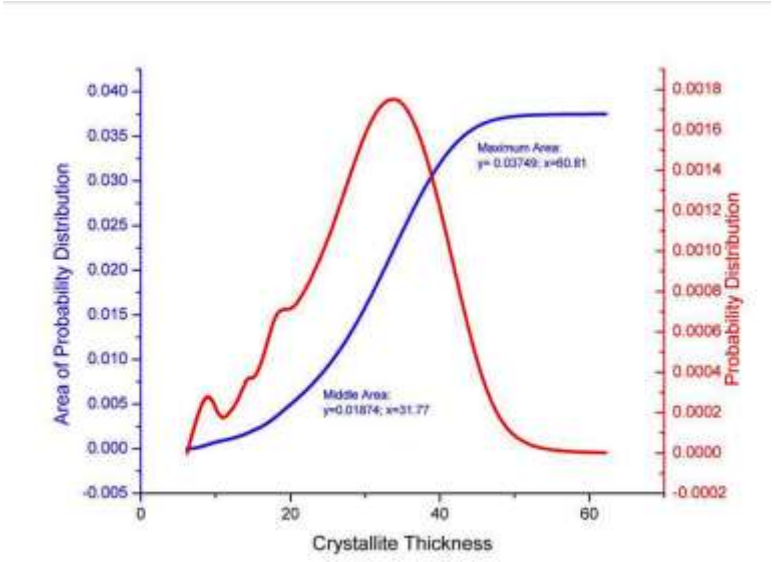

Figure 167: First Moment of 8.7 kGy Proton Irradiated (Sample 83) Crystallite Thickness Distribution for Run 1 (Area Calculations)

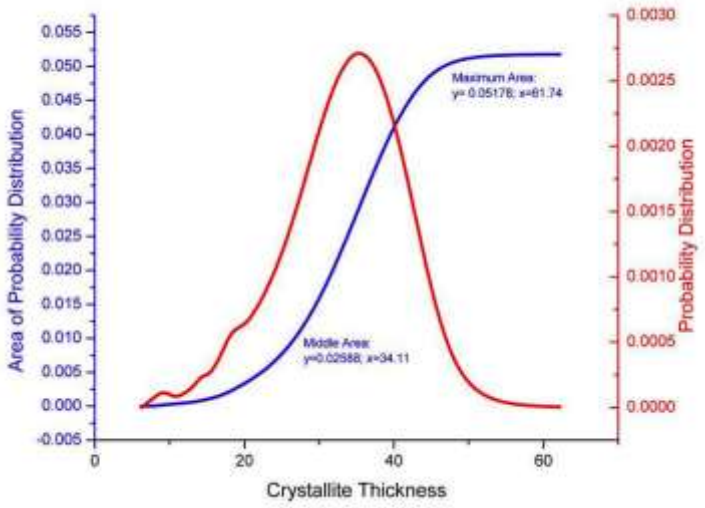

Figure 168: Second Moment of 8.7 kGy Proton Irradiated (Sample 83) Crystallite Thickness Distribution for Run 1 (Area Calculations)

2.2.2 Crystallite Thickness of Thermally Treated Samples (Run 2)

Table 31: Median Crystallite Thicknesses for Proton Irradiation Samples in the Second DSC Run

Dose (kGy)	Crystallite Thicknesss Distribution, l_n	First Moment, l_w	Second Moment, l_z	l_w/l_n	l_z/l_n
0	17.41 ± 1.82	18.98 ± 2.96	20.09 ± 2.60	1.09	1.15
1.77	16.62 ± 0.76	18.43 ± 0.62	19.57 ± 0.71	1.11	1.18
5.89	12.04 ± 0.18	12.76 ± 0.18	13.27 ± 0.19	1.06	1.10

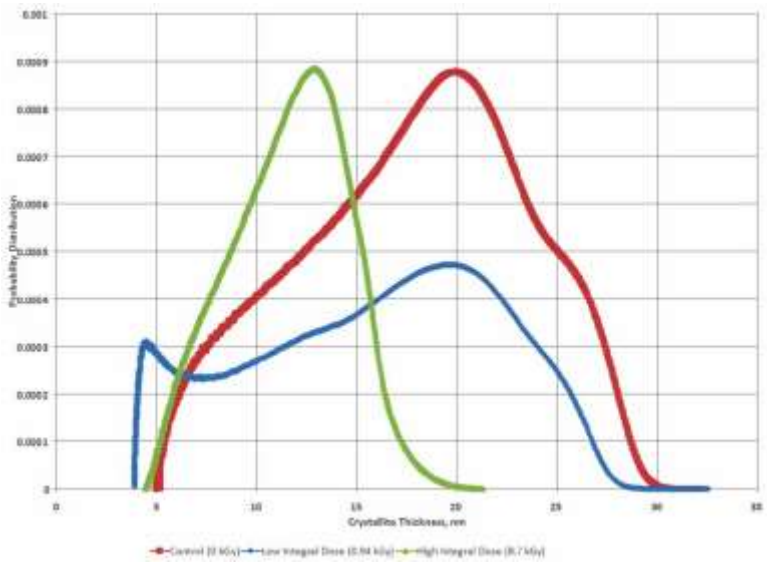

Figure 169: Crystallite Thickness Distribution for Run 2

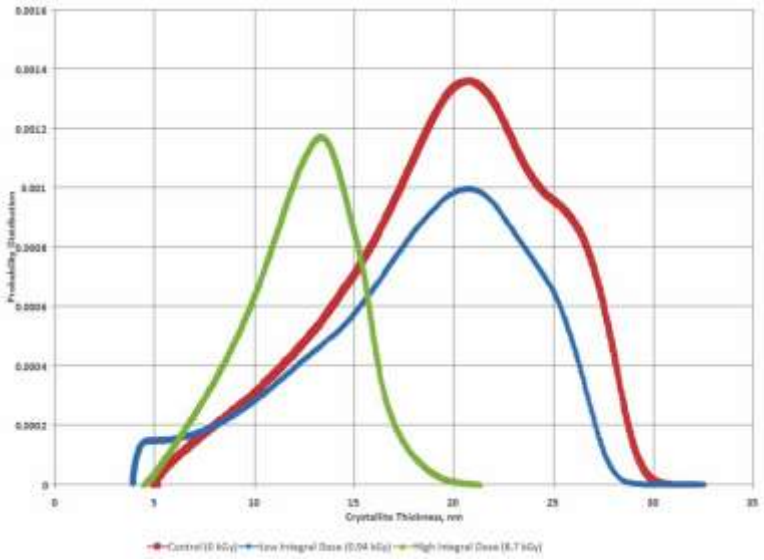

Figure 170: First Moment in Crystallite Thickness Distribution for Run 2

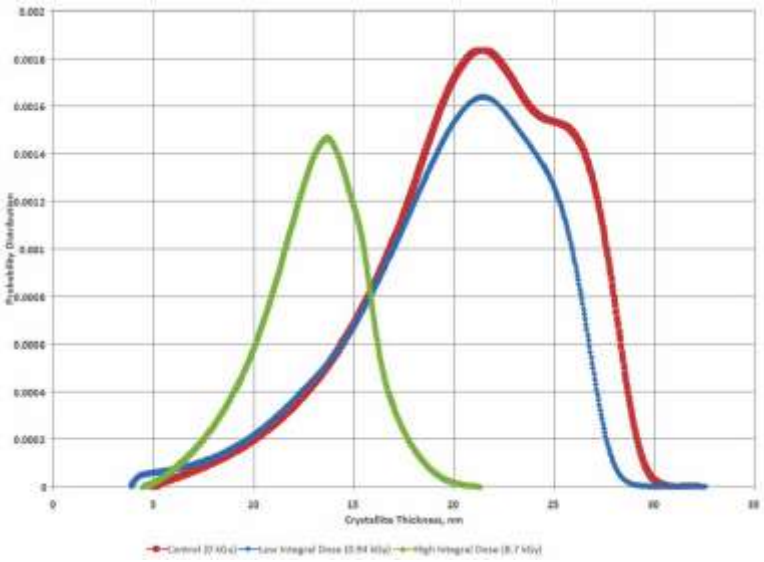

Figure 171: Second Moment in Crystallite Thickness Distribution for Run 2

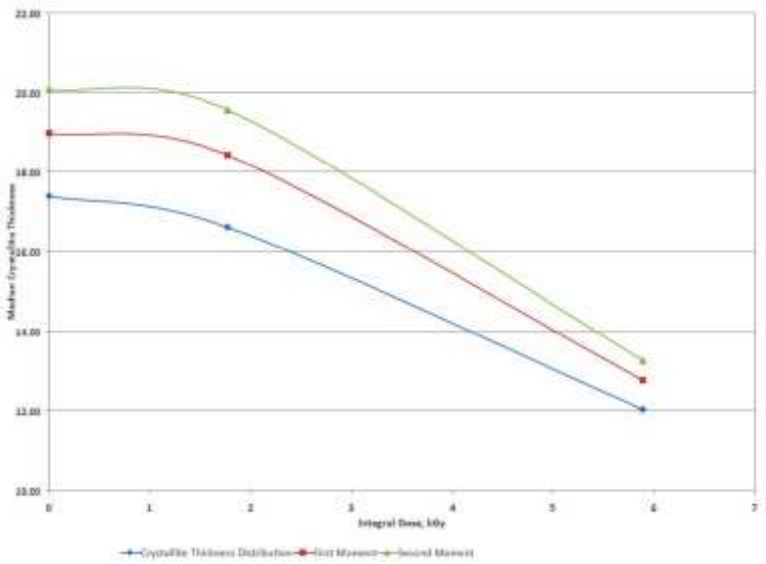

Figure 172: Crystallite Thicknesses for Proton Irradiated Samples in the Second DSC Run

Table 32: Crystallizable Fraction and Sequence Length for Proton Irradiation Samples in the Second DSC Run

Dose (kGy)	Crystallizable Fraction	Sequence Length
0	0.956	68
1.77	0.954	65
5.89	0.937	47

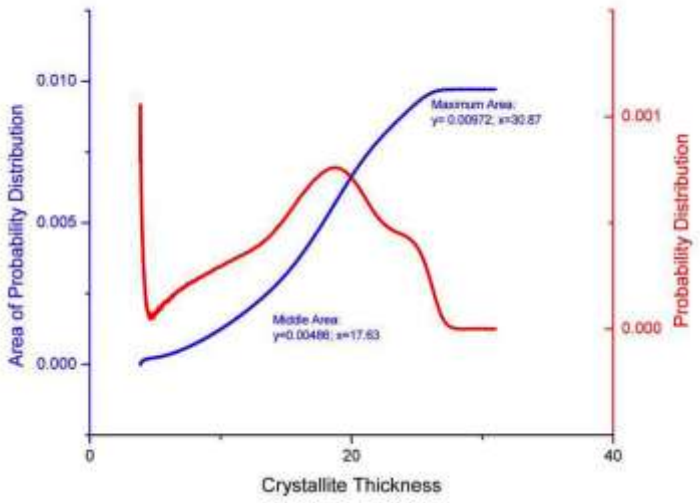

Figure 173: Control (0 kGy) Proton Irradiated (Sample 30) Crystallite Thickness Distribution for Run 2 (Area Calculations)

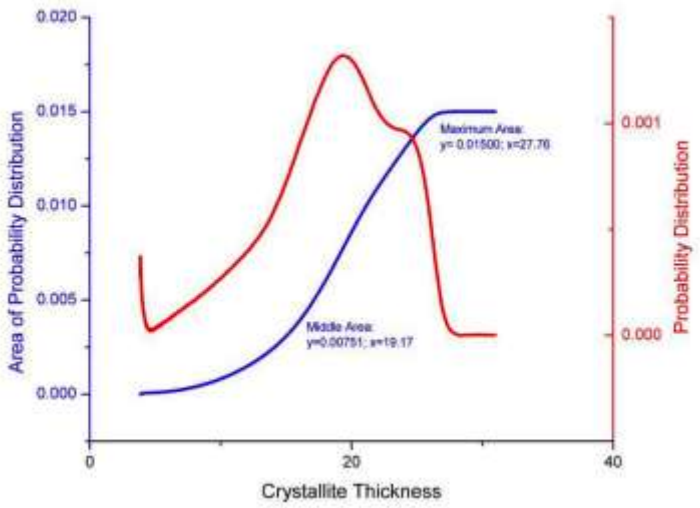

Figure 174: First Moment of Control (0 kGy) Proton Irradiated (Sample 30) Crystallite Thickness Distribution for Run 2 (Area Calculations)

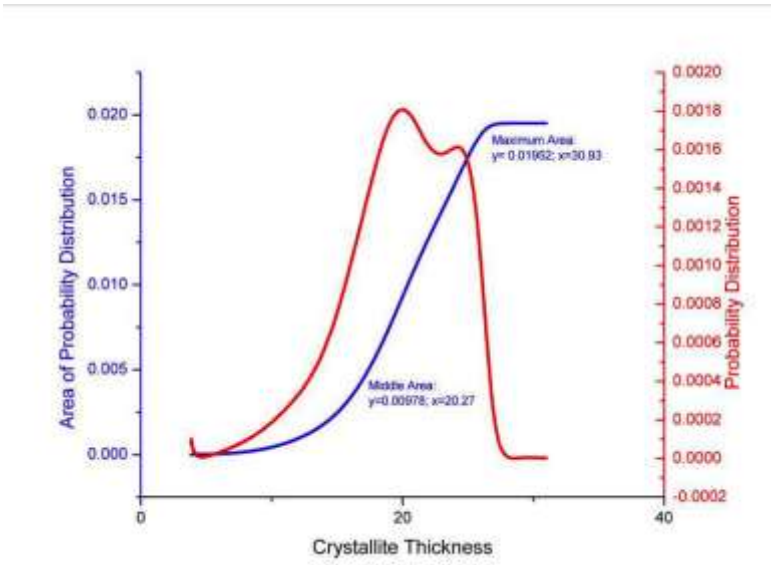

Figure 175: Second Moment of Control (0 kGy) Proton Irradiated (Sample 30) Crystallite Thickness Distribution for Run 2 (Area Calculations)

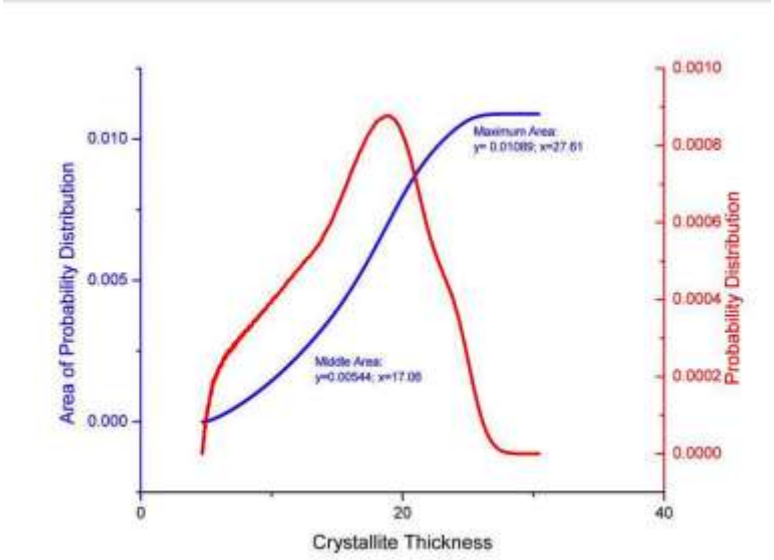

Figure 176: Control (0 kGy) Proton Irradiated (Sample 68) Crystallite Thickness Distribution for Run 2 (Area Calculations)

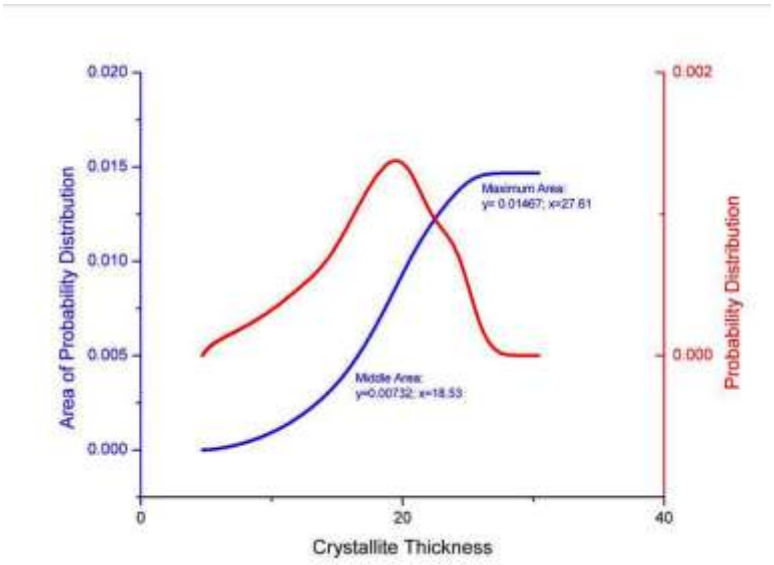

Figure 177: First Moment of Control (0 kGy) Proton Irradiated (Sample 68) Crystallite Thickness Distribution for Run 2 (Area Calculations)

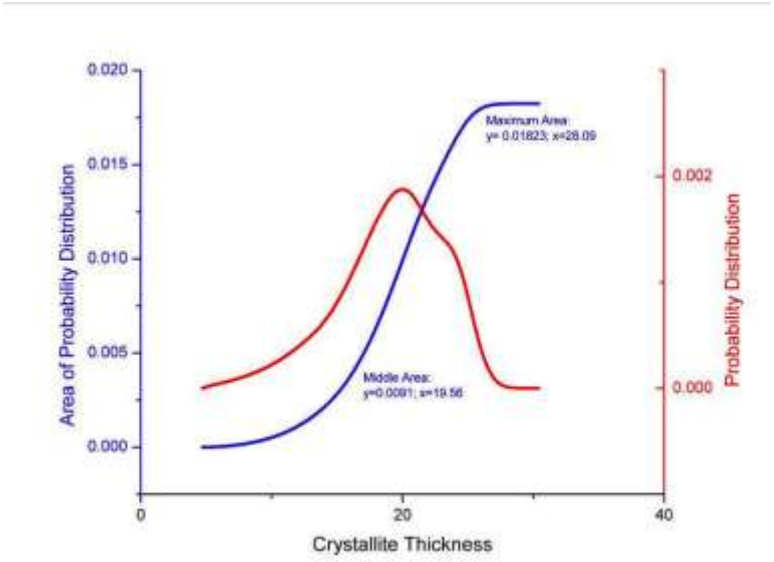

Figure 178: Second Moment of Control (0 kGy) Proton Irradiated (Sample 68) Crystallite Thickness Distribution for Run 2 (Area Calculations)

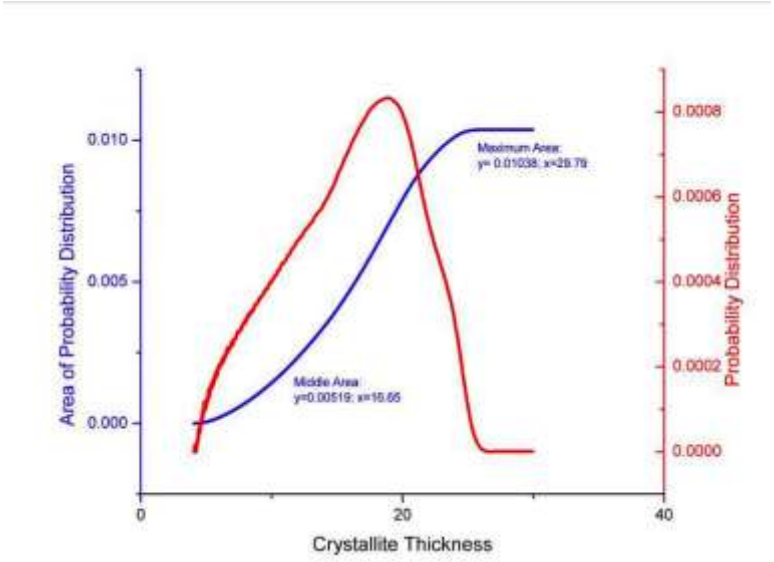

Figure 179: Control (0 kGy) Proton Irradiated (Sample 68) Crystallite Thickness Distribution for Run 2 (Area Calculations)

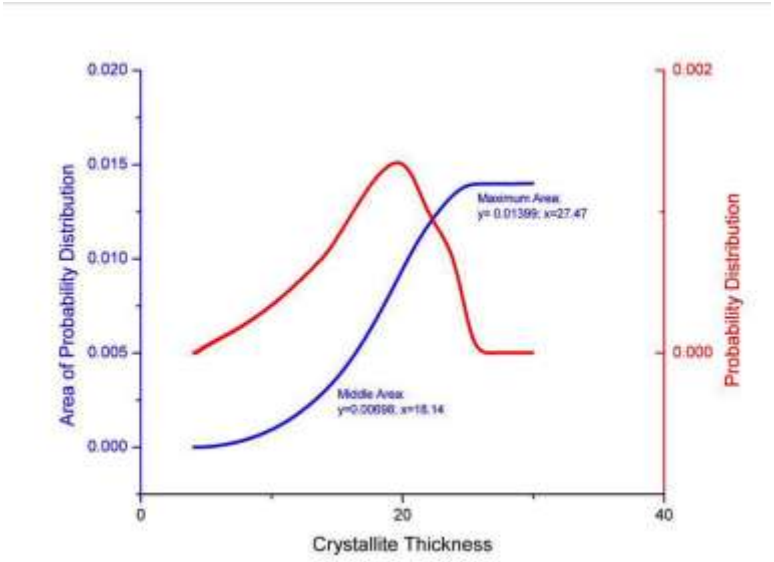

Figure 180: First Moment of Control (0 kGy) Proton Irradiated (Sample 68) Crystallite Thickness Distribution for Run 2 (Area Calculations)

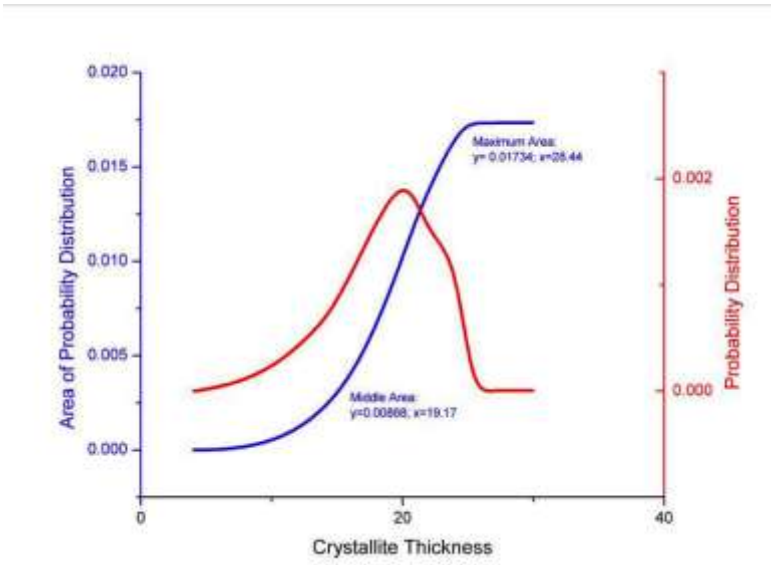

Figure 181: Second Moment of Control (0 kGy) Proton Irradiated (Sample 68) Crystallite Thickness Distribution for Run 2 (Area Calculations)

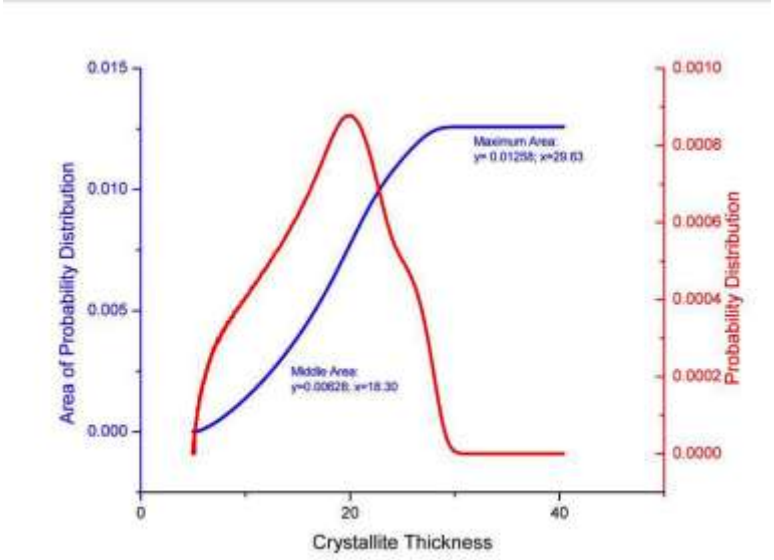

Figure 182: Control (0 kGy) Proton Irradiated (Sample 26) Crystallite Thickness Distribution for Run 2 (Area Calculations)

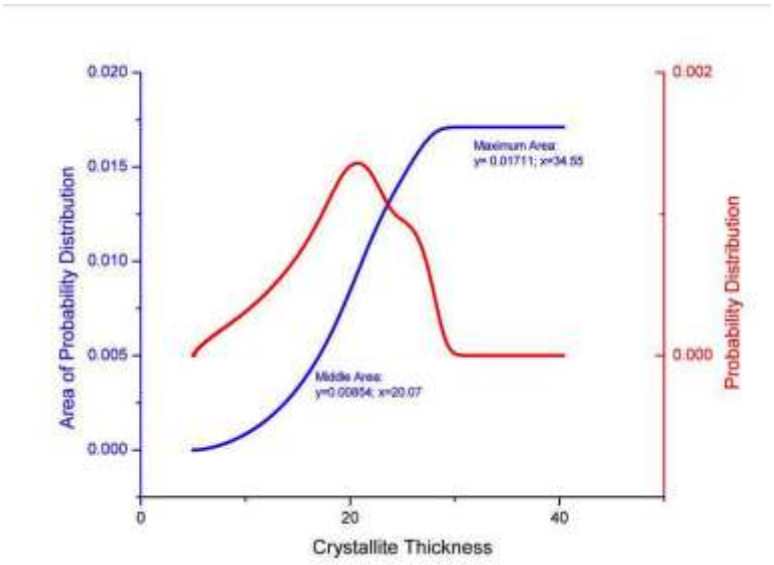

Figure 183: First Moment of Control (0 kGy) Proton Irradiated (Sample 26) Crystallite Thickness Distribution for Run 2 (Area Calculations)

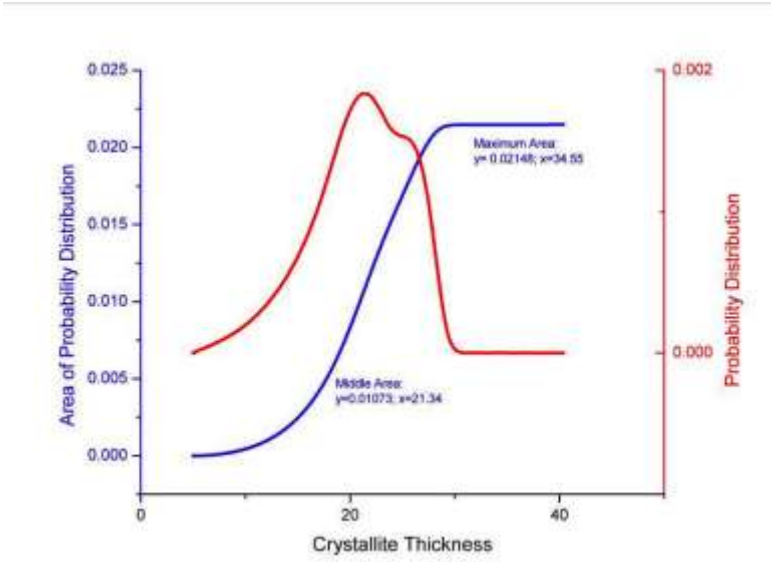

Figure 184: Second Moment of Control (0 kGy) Proton Irradiated (Sample 26) Crystallite Thickness Distribution for Run 1 (Area Calculations)

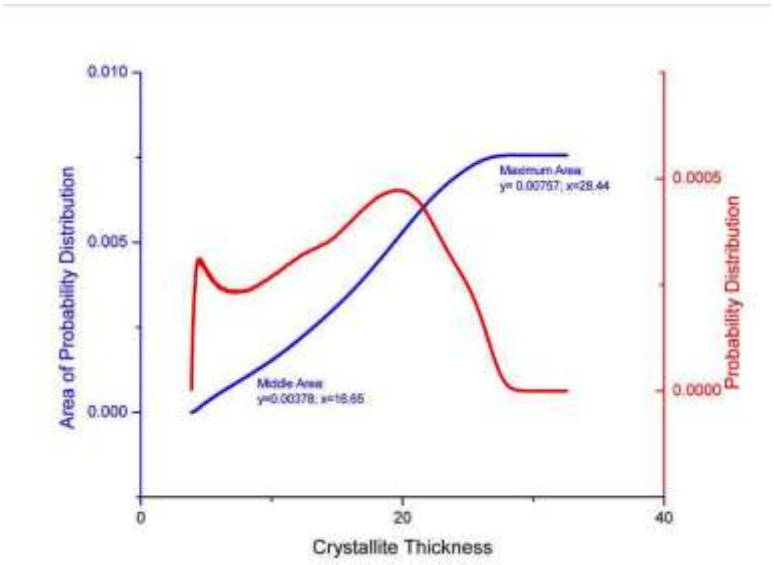

Figure 185: 0.9402 kGy Proton Irradiated (Sample 74) Crystallite Thickness Distribution for Run 2 (Area Calculations)

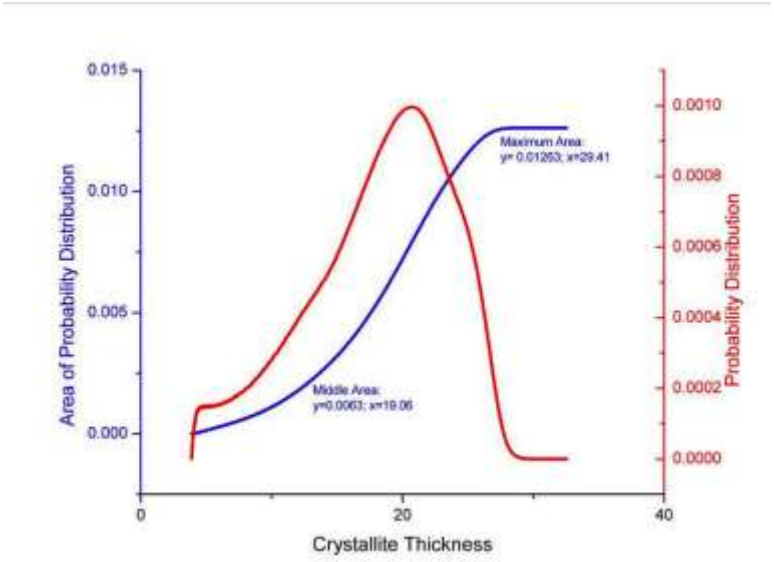

Figure 186: First Moment of 0.9402 kGy Proton Irradiated (Sample 74) Crystallite Thickness Distribution for Run 2 (Area Calculations)

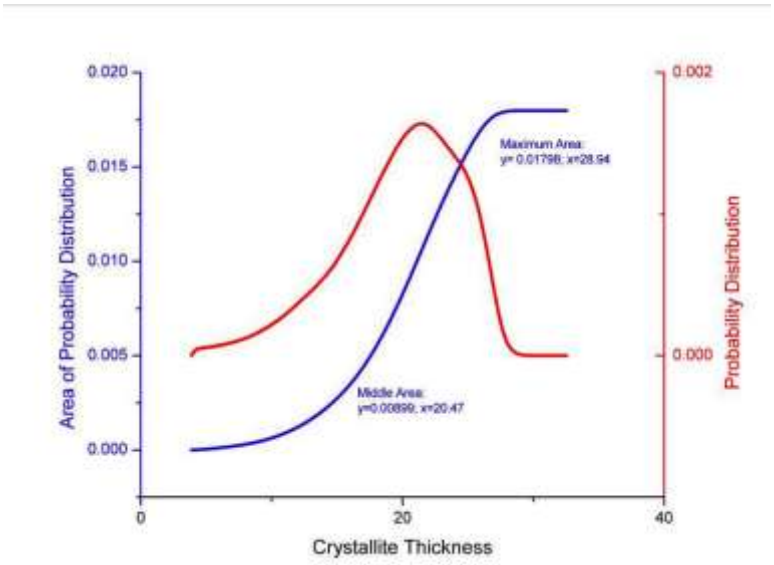

Figure 187: Second Moment of 0.9402 kGy Proton Irradiated (Sample 74) Crystallite Thickness Distribution for Run 2 (Area Calculations)

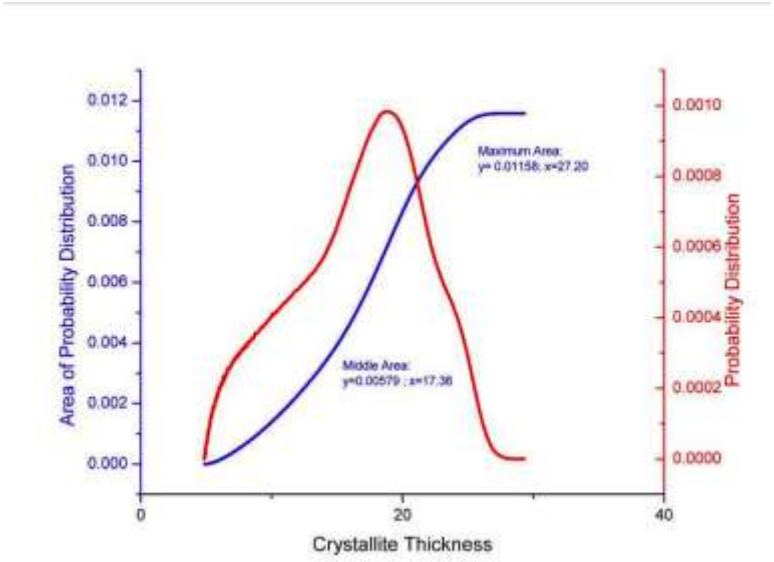

Figure 188: 0.963 kGy Proton Irradiated (Sample 66) Crystallite Thickness Distribution for Run 2 (Area Calculations)

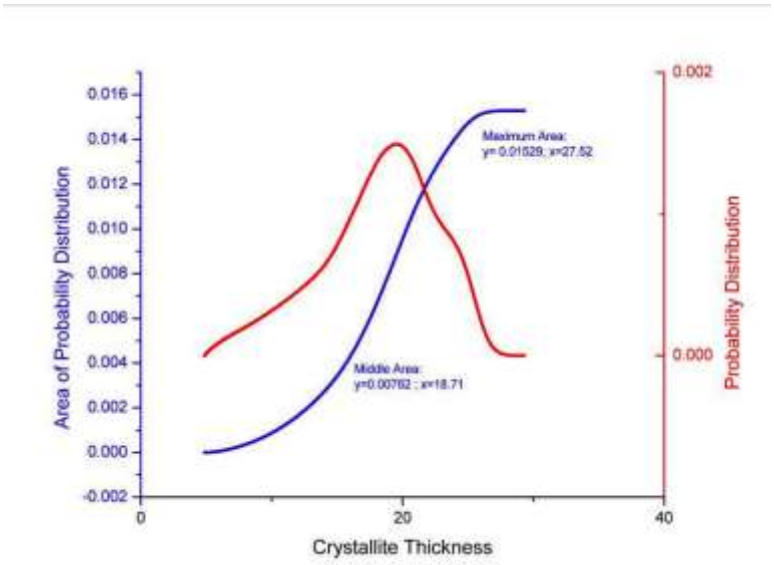

Figure 189: First Moment of 0.963 kGy Proton Irradiated (Sample 66) Crystallite Thickness Distribution for Run 2 (Area Calculations)

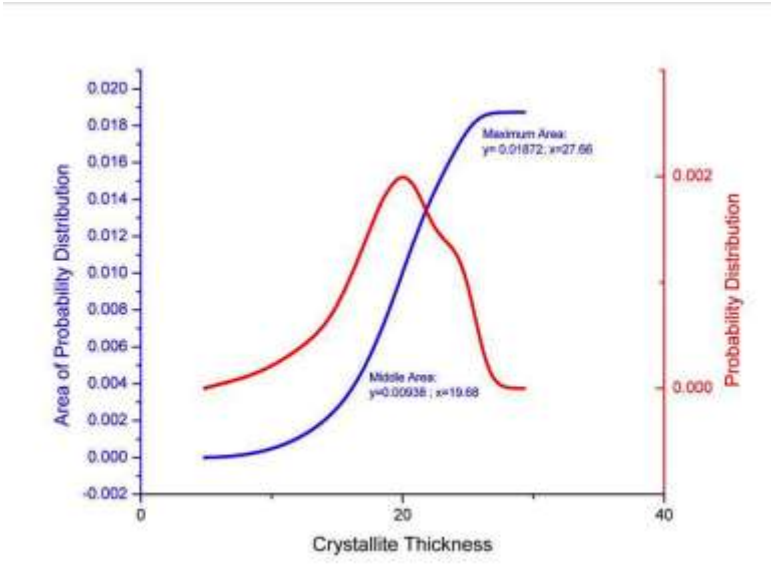

Figure 190: Second Moment of 0.963 kGy Proton Irradiated (Sample 66) Crystallite Thickness Distribution for Run 2 (Area Calculations)

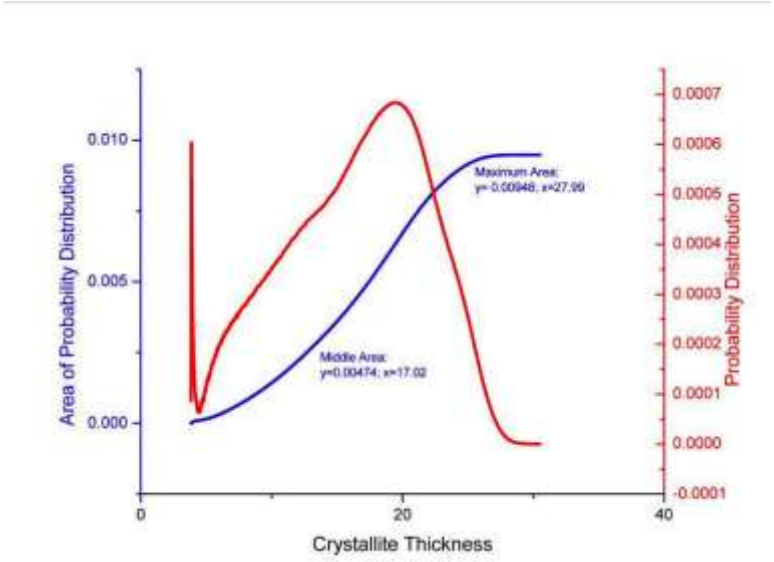

Figure 191: 1.0773 kGy Proton Irradiated (Sample 63) Crystallite Thickness Distribution for Run 2 (Area Calculations)

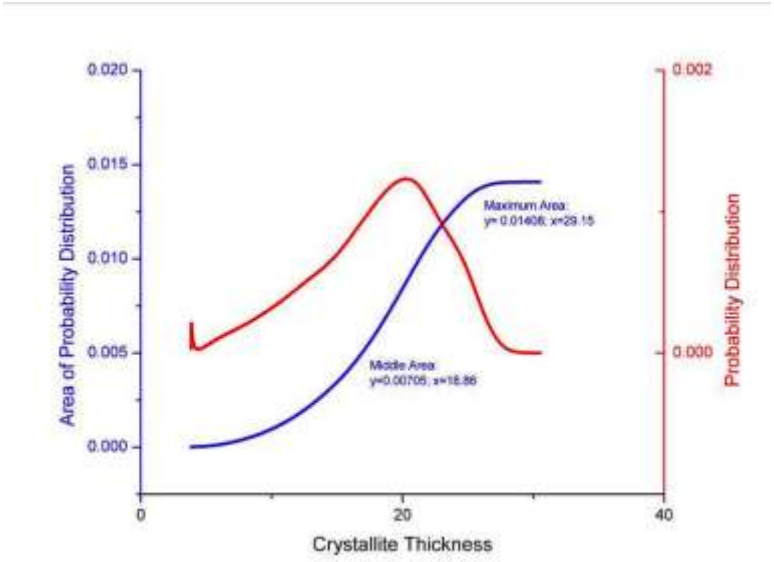

Figure 192: First Moment of 1.0773 kGy Proton Irradiated (Sample 63) Crystallite Thickness Distribution for Run 2 (Area Calculations)

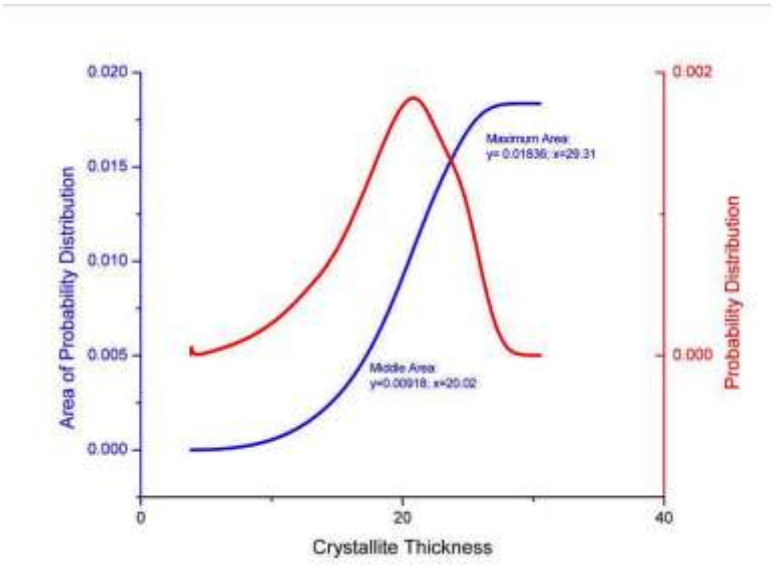

Figure 193: Second Moment of 1.0773 kGy Proton Irradiated (Sample 63) Crystallite Thickness Distribution for Run 2 (Area Calculations)

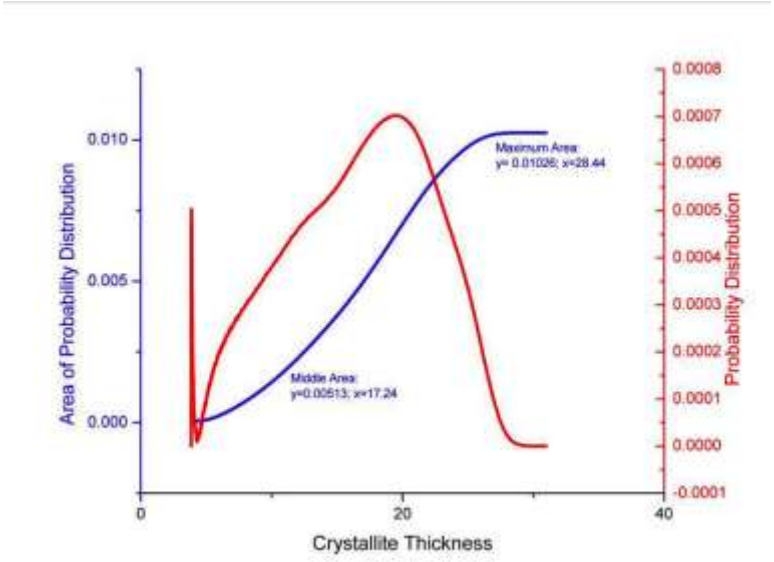

Figure 194: 1.1506 kGy Proton Irradiated (Sample 70) Crystallite Thickness Distribution for Run 2 (Area Calculations)

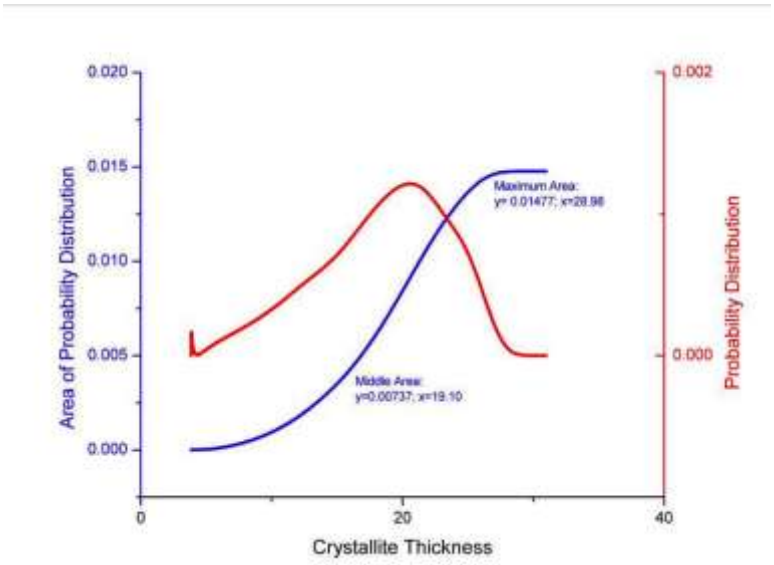

Figure 195: First Moment of 1.1506 kGy Proton Irradiated (Sample 70) Crystallite Thickness Distribution for Run 2 (Area Calculations)

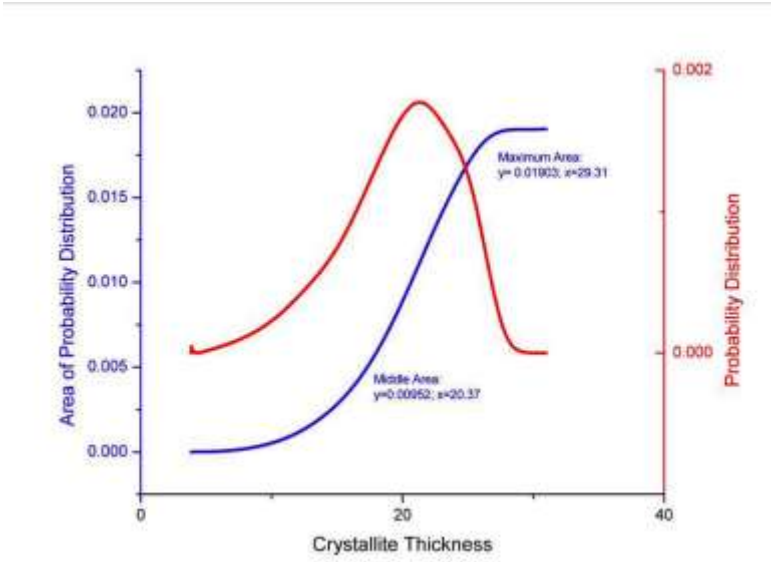

Figure 196: Second Moment of 1.1506 kGy Proton Irradiated (Sample 70) Crystallite Thickness Distribution for Run 2 (Area Calculations)

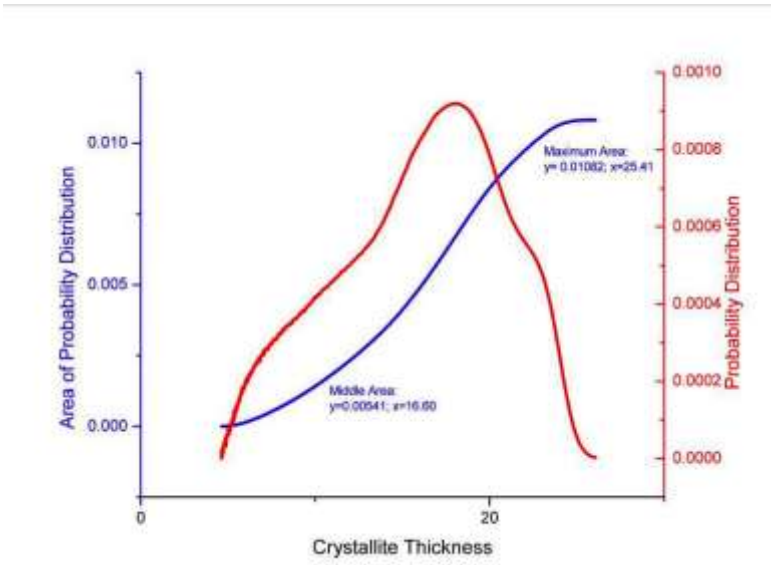

Figure 197: 1.3289 kGy Proton Irradiated (Sample 57) Crystallite Thickness Distribution for Run 2 (Area Calculations)

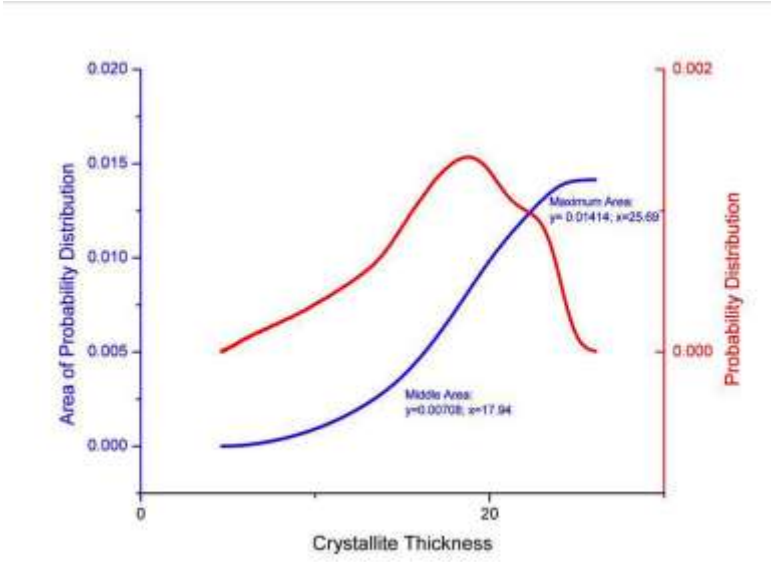

Figure 198: First Moment of 1.3289 kGy Proton Irradiated (Sample 57) Crystallite Thickness Distribution for Run 2 (Area Calculations)

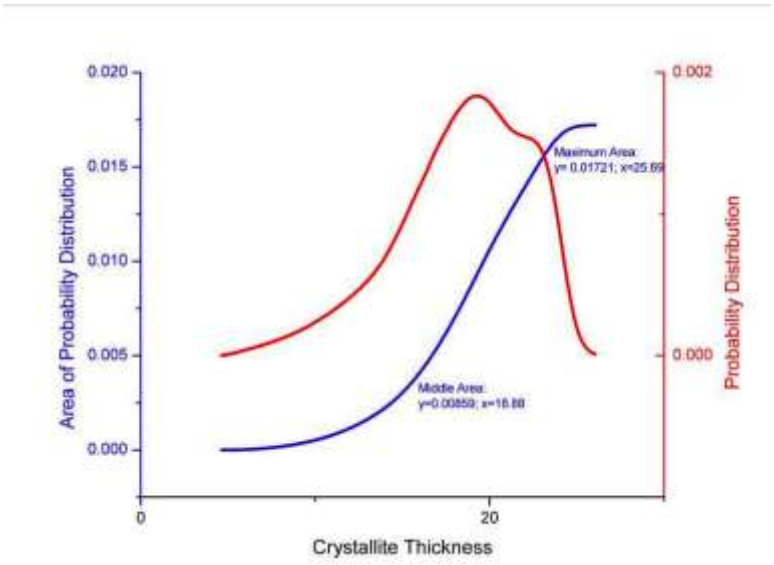

Figure 199: Second Moment of 1.3289 kGy Proton Irradiated (Sample 57) Crystallite Thickness Distribution for Run 2 (Area Calculations)

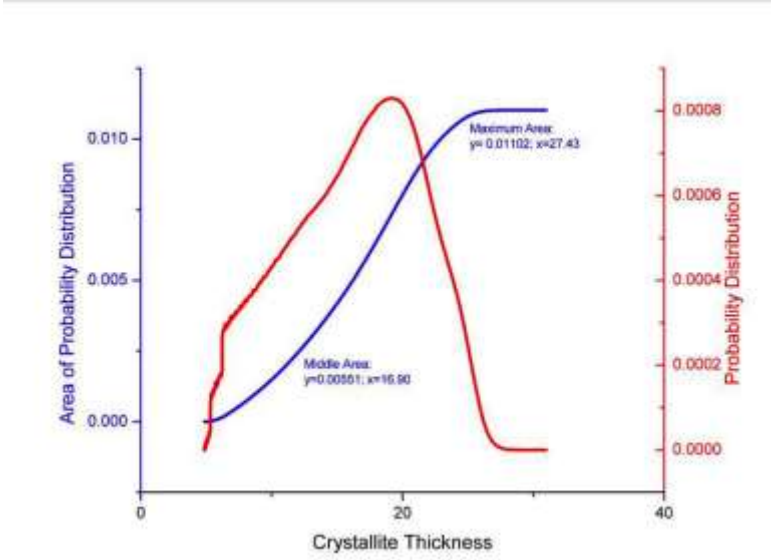

Figure 200: 1.3289 kGy Proton Irradiated (Sample 57) Crystallite Thickness Distribution for Run 2 (Area Calculations)

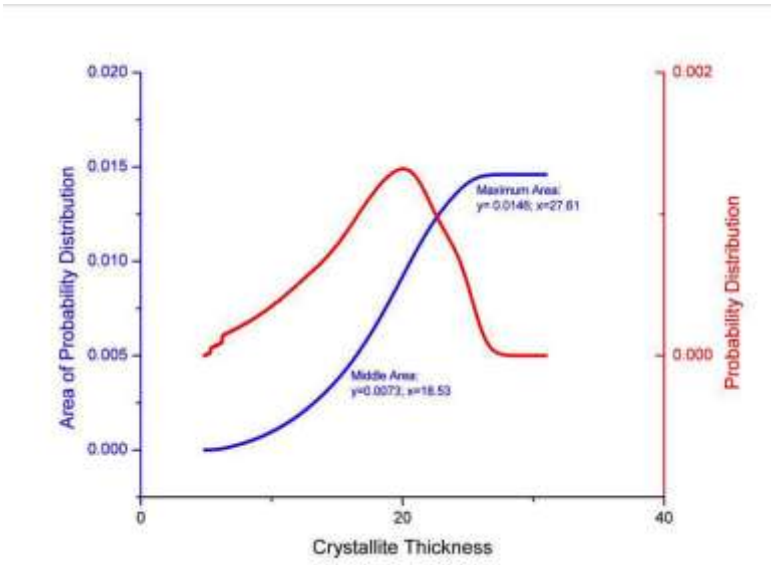

Figure 201: First Moment of 1.3289 kGy Proton Irradiated (Sample 57) Crystallite Thickness Distribution for Run 2 (Area Calculations)

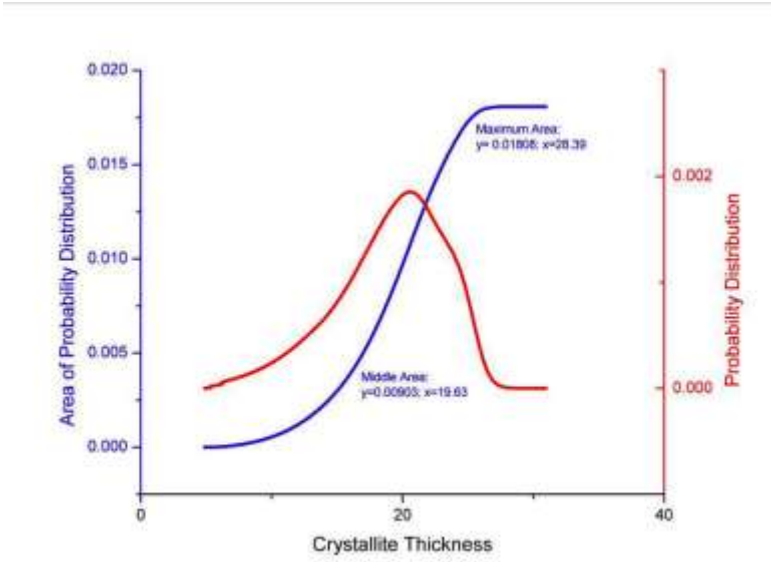

Figure 202: Second Moment of 1.3289 kGy Proton Irradiated (Sample 57) Crystallite Thickness Distribution for Run 2 (Area Calculations)

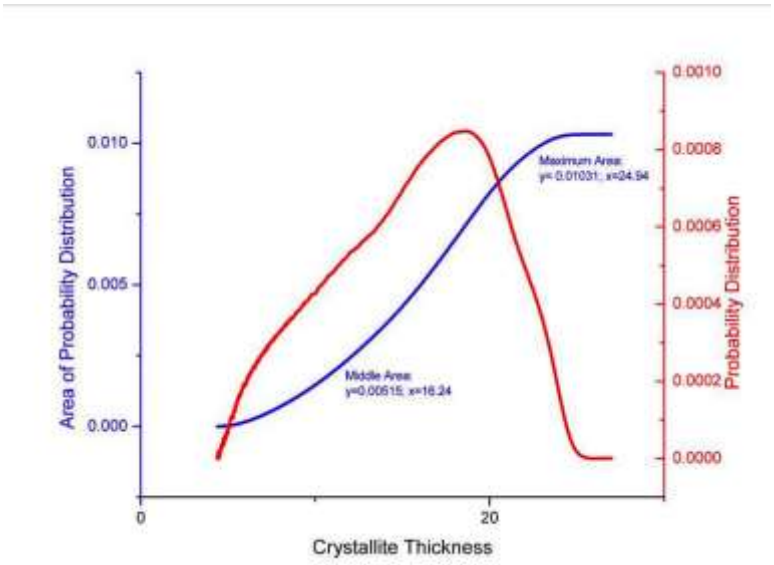

Figure 203: 3.7 kGy Proton Irradiated (Sample 58) Crystallite Thickness Distribution for Run 2 (Area Calculations)

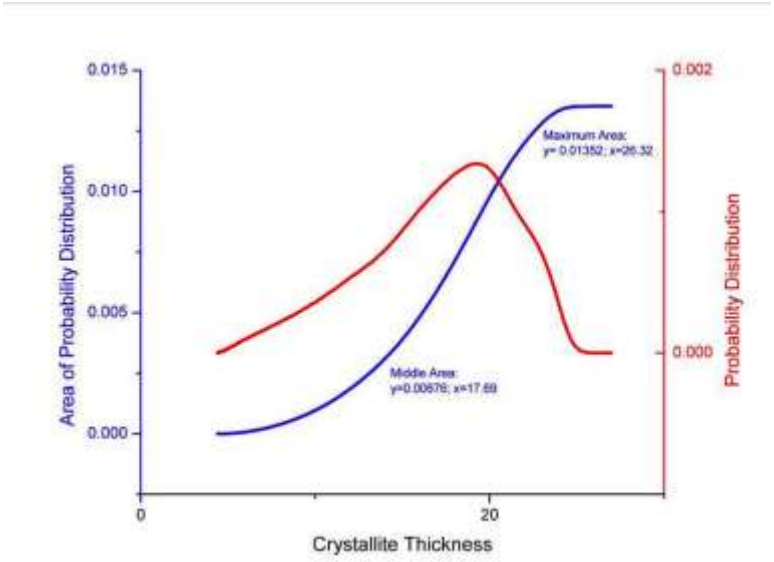

Figure 204: First Moment of 3.7 kGy Proton Irradiated (Sample 58) Crystallite Thickness Distribution for Run 2 (Area Calculations)

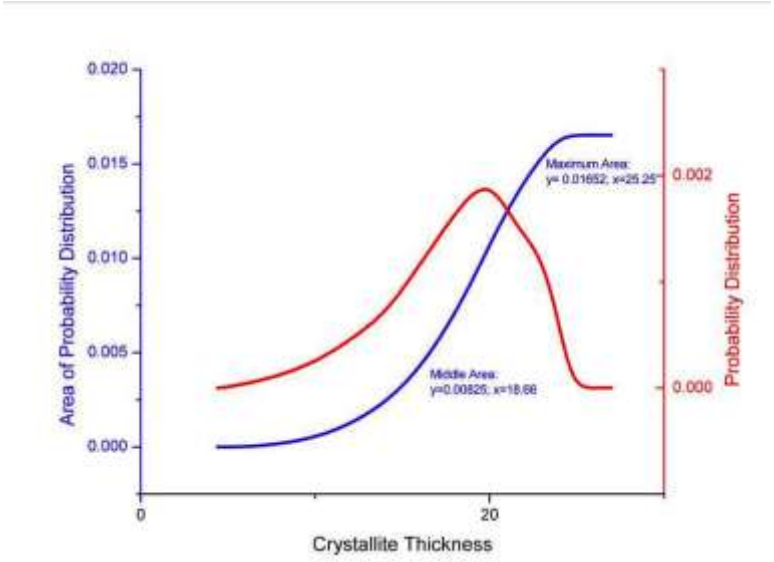

Figure 205: Second Moment of 3.7 kGy Proton Irradiated (Sample 58) Crystallite Thickness Distribution for Run 2 (Area Calculations)

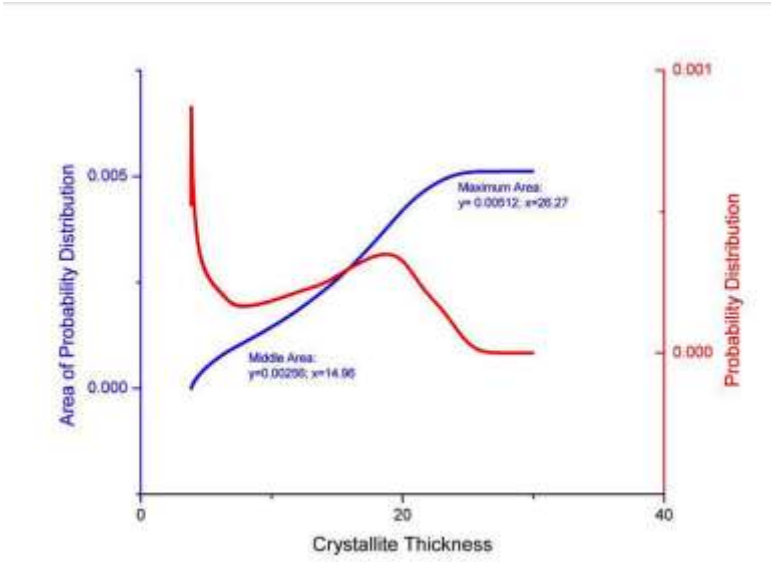

Figure 206: 3.7 kGy Proton Irradiated (Sample 58) Crystallite Thickness Distribution for Run 2 (Area Calculations)

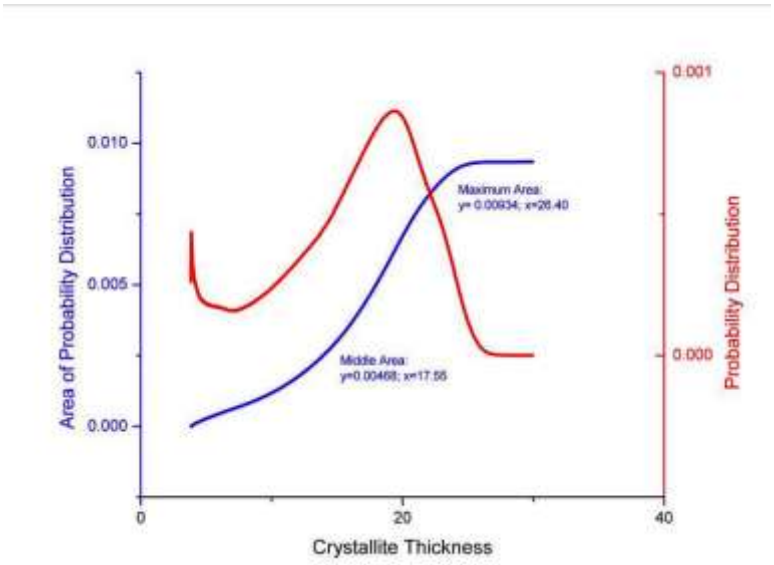

Figure 207: First Moment of 3.7 kGy Proton Irradiated (Sample 58) Crystallite Thickness Distribution for Run 2 (Area Calculations)

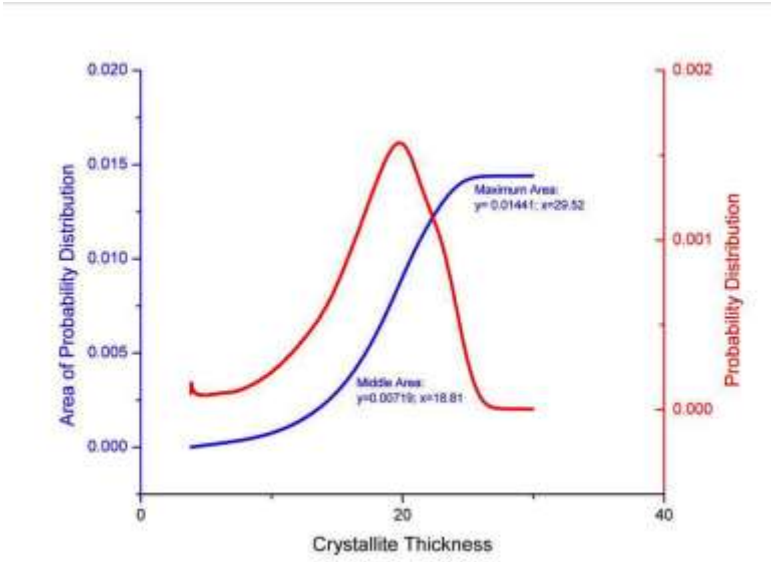

Figure 208: Second Moment of 3.7 kGy Proton Irradiated (Sample 58) Crystallite Thickness Distribution for Run 2 (Area Calculations)

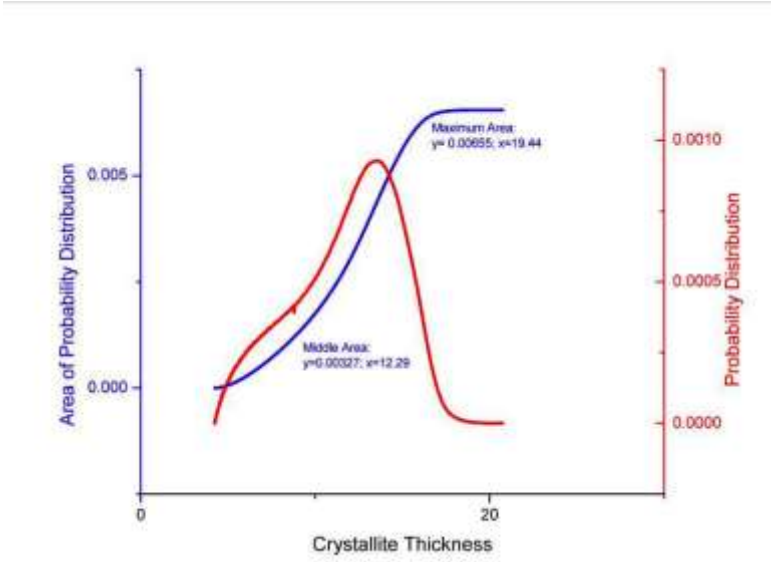

Figure 209: 6.8 kGy Proton Irradiated (Sample 87) Crystallite Thickness Distribution for Run 2 (Area Calculations)

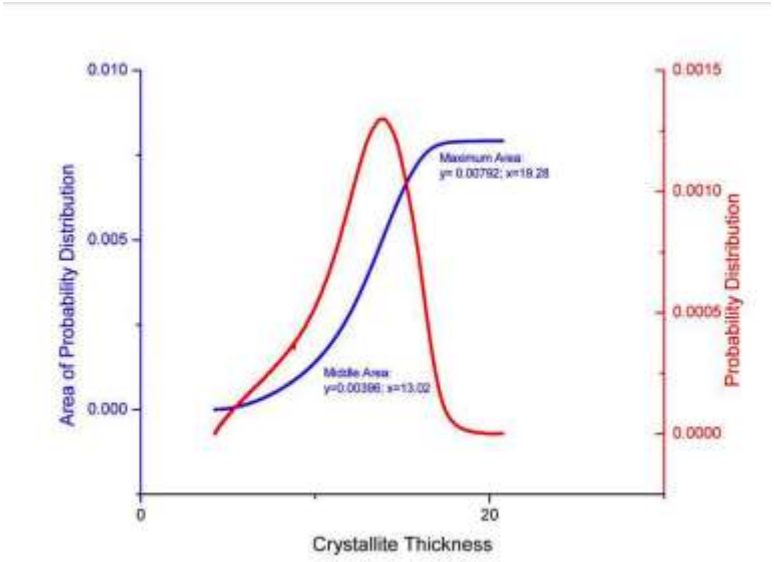

Figure 210: First Moment of 6.8 kGy Proton Irradiated (Sample 87) Crystallite Thickness Distribution for Run 2 (Area Calculations)

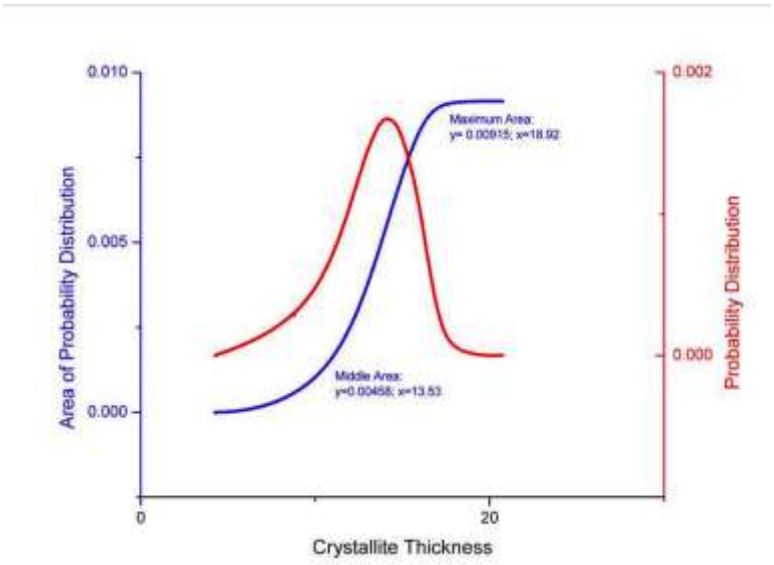

Figure 211: Second Moment of 6.8 kGy Proton Irradiated (Sample 87) Crystallite Thickness Distribution for Run 2 (Area Calculations)

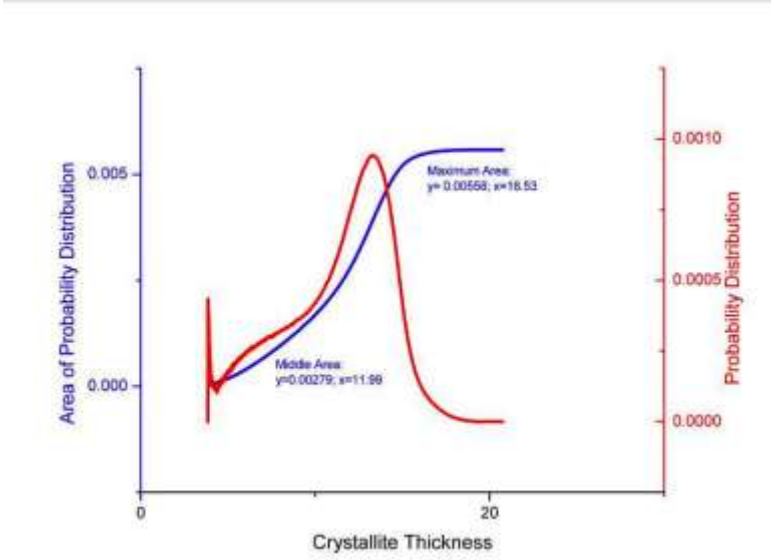

Figure 212: 8.3 kGy Proton Irradiated (Sample 80) Crystallite Thickness Distribution for Run 2 (Area Calculations)

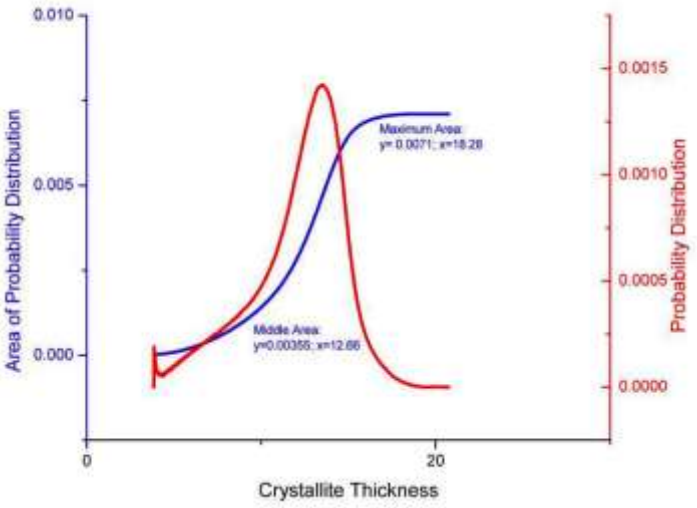

Figure 213: First Moment of 8.3 kGy Proton Irradiated (Sample 80) Crystallite Thickness Distribution for Run 2 (Area Calculations)

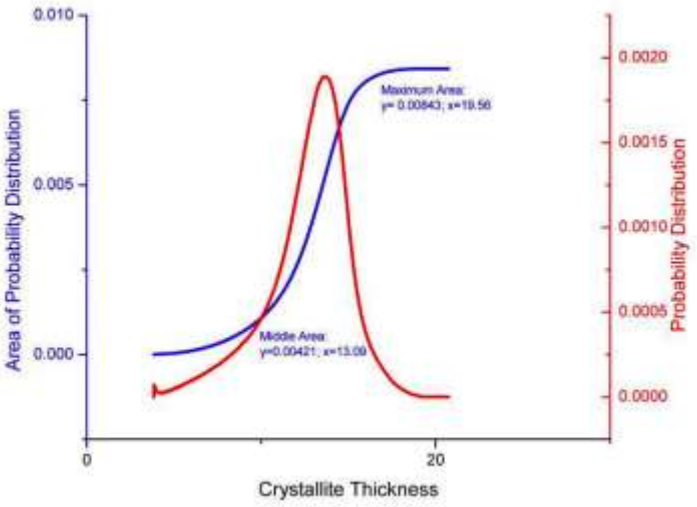

Figure 214: Second Moment of 8.3 kGy Proton Irradiated (Sample 80) Crystallite Thickness Distribution for Run 2 (Area Calculations)

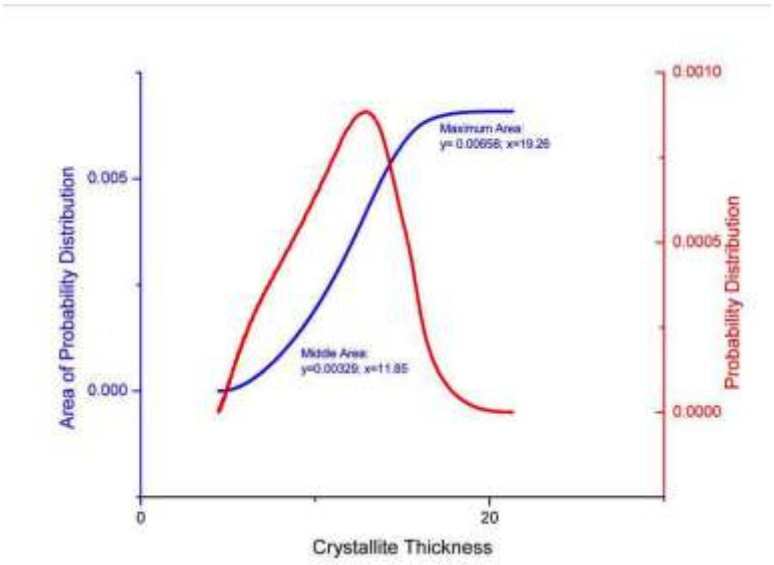

Figure 215: 8.7 kGy Proton Irradiated (Sample 83) Crystallite Thickness Distribution for Run 2 (Area Calculations)

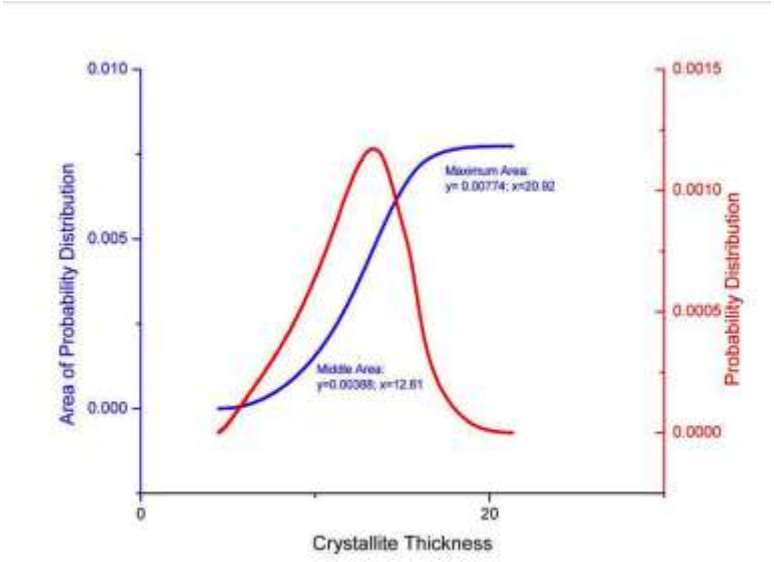

Figure 216: First Moment of 8.7 kGy Proton Irradiated (Sample 83) Crystallite Thickness Distribution for Run 2 (Area Calculations)

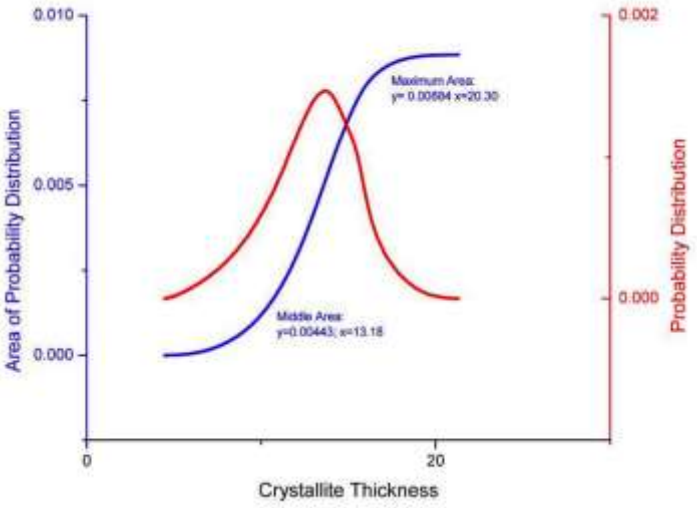

Figure 217: Second Moment of 8.7 kGy Proton Irradiated (Sample 83) Crystallite Thickness Distribution for Run 2 (Area Calculations)

Vita

Christopher P. Stephens was born in Allentown, Pennsylvania, on March 18, 1981. He graduated from Farragut High School in 1999. Chris began his undergraduate education in 1999 at the University of Tennessee at Knoxville and graduated with a B.S. in Materials Science and Engineering in 2004 and a M.S. in Polymer Engineering in 2006.